Active Vortex Generation using Dielectric Barrier Discharge Plasma Actuators in Laminar Boundary Layers

Vom Fachbereich Maschinenbau
an der Technischen Universität Darmstadt
zur
Erlangung des Grades eines Doktor-Ingenieurs (Dr.-Ing.)
genehmigte

D i s s e r t a t i o n

vorgelegt von

Dipl.-Ing. Katrin Barckmann

aus Büdingen

Berichterstatter:	Prof. Dr.-Ing. C. Tropea
Mitberichterstatter:	Prof. Dr.-Ing. K.-S. Choi
Tag der Einreichung:	04.11.2013
Tag der mündlichen Prüfung:	18.12.2013

Darmstadt 2014
D17 (Diss. Darmstadt)

Hiermit versichere ich, die vorliegende Doktorarbeit unter der Betreuung von Prof. Dr.-Ing. C. Tropea und Dr.-Ing. S. Grundmann nur mit den angegebenen Hilfsmitteln selbständig angefertigt zu haben.

Darmstadt, den 1. November 2013,

Abstract

The aim of this study is the characterization and quantification of dielectric barrier discharge plasma actuators when applied to the generation of stable vortices in laminar boundary layers for flow control. To this aim, existing measurement and analysis strategies were applied and extended. Using a specific actuator configuration the lower and upper operation limits have been identified. Between these limits, a constant and two-dimensional force distribution of the actuator can be expected. These operation limits were used to define the parameter range for the description of the induced body force in extent and magnitude. Alongside with this characterization the time resolved force production was analyzed. Based on these studies, the influencing parameters resulting from the actuator setup and the operating conditions were analyzed and quantified. Empirically determined scaling laws describing each influencing parameter were introduced. This enabled an improved prediction of the induced force for varying operating conditions. In addition to this direct scaling of the induced force by influencing the discharge, an indirect scaling method was presented by a non-continuous operation. This reduces the time-averaged force production and, therefore, allows decoupling of the force magnitude and its spatial extent. The analysis of the influencing parameters of the force production was used as a basis for parameter identification during the generation of longitudinal vortices by plasma actuator arrays. The qualification of plasma actuator vortex generators for transition control was demonstrated by the damping of Tollmien-Schlichting waves in laminar boundary layers in two different wind tunnels.

Kurzfassung

Ziel dieser Arbeit ist die Charakterisierung und Quantifizierung von dielektrischen Barriereentladungs-Plasma-Aktuatoren im Hinblick auf die Erzeugung stabiler Wirbel in laminaren Grenzschichten zur Strömungskontrolle. Bei den durchgeführten Untersuchungen wurden bestehende Mess- und Auswertungsstrategien angewendet und erweitert. Am Beispiel einer Aktuatorkonfiguration wurde der Arbeitsbereich identifiziert in dem eine konstante und zweidimensionale Kraftverteilung des Aktuators angenommen werden kann. Dieser Arbeitsbereich diente als Parameterraum um die erzeugte Volumenkraft in ihrer Ausdehnung und Magnitude zu beschreiben. Dabei wurde auch die zeitliche Entwicklung der Kraft untersucht. Basierend auf diesen Untersuchungen wurden Parametereinflüsse die aus dem Aufbau und den Betriebsmodi des Aktuators resultieren analysiert und quantifiziert. Empirisch ermittelte Skalierungsgrößen zur Beschreibung der Parameter wurden eingeführt, um eine verbesserte Vorhersage der erzeugten Kraft ermöglichen. Neben dieser direkten Skalierung der Kraft, die durch eine Veränderung der Entladung erreicht wird, wurde eine indirekte Skalierungsmethode vorgestellt. Hierbei wird durch einen nicht kontinuierlichen Betrieb die Kraft im zeitlichen Mittel reduziert und somit ermöglicht, die Magnitude der Kraft von ihrer räumlichen Ausdehnung zu entkoppeln. Diese Parameteruntersuchung diente als Grundlage zu Identifizierung der Einflussgrößen bei der Erzeugung von longitudinalen Wirbeln mit Plasma-Aktuator-Wirbelgeneratoren. Die Qualifikation von Plasma-Aktuator- Wirbelgeneratoren zur Transitionskontrolle wurde anhand der Dämpfung von Tollmien-Schlichting Wellen in laminaren Grenzschichten in zwei verschiedenen Windkanälen gezeigt.

Acknowledgements

I would like to thank Prof. Dr. Cameron Tropea for ensuring the freedom to pursue the research summarized in this thesis while working at the Center of Smart Interfaces at TU Darmstadt. Furthermore, I appreciate the support by Dr. Sven Grundmann, who always had an open office door and engaged in fruitful discussions.

I would also like to acknowledge with much appreciation Prof. Kwing-So Choi's commitment to co-referee this thesis.

The financial support by the Federal Republic of Germany within the German Aeronautical Research Program LuFo IV in the framework of the AKSA project of the Federal Ministry of Economics and Technology (BMWi) as per resolution of the German Parliament (Grant 20E1101A) is thankfully acknowledged.

I would also like to extend my thanks to Prof. Jens Fransson from KTH for the successful cooperation and fruitful discussions to this work. Additionally, I thank Bengt Fallenius for the collaborative wind-tunnel experiments at KTH as well as the support during my short-term stay in Stockholm.

Multiple experimental setups have only been completed in time due to the arduous work of the electrical and mechanical workshops, and I would like to thank the whole workforce for their persistent support.

The excellent working atmosphere at the wind-tunnel facilities in Griesheim has always been motivating, foremost due to the presence of my collaborators. I am grateful to Alexander Duchmann, Ulrike Cordes, Daniela Klaubert, Jochen Kriegseis, Armin Kurz, Lars Opfer, Bernhard Simon, Debora Vieira, Florian Wassermann and Alexander Widmann for their help and suggestions related to experiments and numerical studies, but also for becoming friends beyond the professional sphere. I am delighted to have supervised many excellent students who fundamentally contributed to the results of this research: Sebastian Bürkle, Tobias Corneli, Felix Diegelmann, Nikolas Kienzle, Imdat Maden, Sebastian Saul and Anton Wasilenko. Finally, I would like to express my deepest gratitude to my family as well as my friends and Stefan, who unconditionally supported me during the good and hard times of my doctoral studies.

Contents

1 Introduction

Dielectric barrier discharge (DBD) plasma actuators are active flow control devices that allow a body force to be imposed to gaseous fluids. Dielectric discharges are known from industrial application such as ozone generation, panel displays, lasers and surface treatments [78]. Since their introduction in 1998 [129] for aerodynamic flow control, active flow control by means of plasma actuators is a research topic of increasing interest.

For aerodynamic flow control applications the DBD plasma actuator commonly consist of asymmetrically arranged electrodes separated by a dielectric. By applying a high alternating voltage to the upper electrode, the electric field, between the upper and the lower grounded electrode, exceeds the breakdown strength, which is required to ionize the air molecules. The dielectric layer between the electrodes allows a diffuse discharge and prevents it to collapse into an arc. The produced ions are accelerated in the electric field, through collision with neutral air molecules this results in the induced body force. Due to the asymmetric orientation of the electrodes, the induced force is directed towards the covered, grounded electrode. Further details on the actuator and its functionality are discussed later in Chapter 2. A comprehensive overview of the actuator and flow control employing dielectric barrier discharges is presented by Corke *et al.* [21] and Moreau [105].

First examples for aerodynamic flow control devices are given in the work of Roth *et al.* [133] and Post *et al.* [122], demonstrating the potential of DBD plasma actuators for boundary-layer separation control. Since then the spectrum of applications has broadened considerably. Some examples for the variety of the active flow control applications using DBD plasma actuators includes separation control [114, 126], aircraft noise reduction [64], reducing losses with compressor blades [90], wake control [39], bluff body flow control [68, 69, 80, 103, 145], boundary-layer control in laminar [53, 57] and turbulent flows [158], and influencing supersonic flow [65, 75].

However, the main focus of active flow control investigations with DBD plasma actuators is on separation control.

In the next section an overview of literature with DBD plasma actuators for separation control will be given, focusing on different separation

scenarios and various operation conditions and actuator configurations.

This leads to some general conclusions about the advantages and limitations of different configurations for different applications. An outline of the present study follows.

1.1 DBD Plasma Actuators for Separation Control

DBD plasma actuators have been investigated for several separation scenarios and various operation conditions (continuous and pulsed mode) and actuator configurations (streamwise and spanwise forcing). In the low Reynolds number range below $Re = 10^6$ and with moderate free-stream velocities, within the incompressible subsonic range, DBD plasma actuators have proved to be an effective flow control device [69]. Separation control with plasma actuators on airfoils have been demonstrated by Roth *et al.* [126] at velocities up to $U = 7.3\frac{\mathrm{m}}{\mathrm{s}}$. Corke and He [20] showed an improvement in control performance with the actuator operated in the unsteady/pulsed mode.

Further actuator configurations for separation control with plasma actuators on airfoils were tested with different positions of streamwise forcing actuators by Jolibois *et al.* [66] and arrays of spanwise forcing actuators Jukes *et al.* [73]. The complexity of these flow-control experiments increased with the extension to closed-loop control shown by Bernard *et al.* [12] with a single spanwise actuator. The potential for feedback control with arrays of spanwise forcing actuators was shown by Jukes *et al.* [72].

Flow control in a turbulent boundary layer across a hump was investigated by He *et al.* [58] and Schatzmann *et al.* [136]. The plasma actuator configurations used in both investigations were single streamwise forcing actuators and arrays of spanwise forcing actuators. With both actuator configurations (streamwise and spanwise forcing) He *et al.* and Schatzmann *et al.* achieved comparable results for the flow control. Schatzmann *et al.* used single spanwise actuators in continuous and pulsed mode and they observed no sensitivity to the reduced frequency F^+ over a large range. An explanation of this lack of sensitivity was given by flow instabilities which the actuator did not exploit, as compared to laminar separation-control applications.

Benard *et al.* [9] examined the attachment of naturally separated flow and at the detachment of naturally attached flow in a diffusor. With span-

wise arranged actuators Bernard *et al.* were able to influence an internal flow with a core velocity of $U = 10$ to $30\frac{\mathrm{m}}{\mathrm{s}}$. Spanwise and streamwise forcing configurations were investigated in Grundmann *et al.* [52] to recover a fully turbulent separated flow in an asymmetric 3D diffuser. A stronger effect was observed with arrays of spanwise forcing actuators. Another demonstartion by Benard *et al.* [9], was adjustable diffuser performance (improvement or degradation) depending on the actuation parameters.

Flow control around a cylinder in a moderate Reynolds number range ($Re = 2k - 30k$) were investigated by Snyder *et al.* [145], Thomas *et al.* [148] and Jukes *et al.* [68, 69] with streamwise forcing actuators. Thomas *et al.* investigated the suppression of the vortex shedding, relevant for noise reduction. Jukes *et al.* showed that depending on the actuation parameters two different regimes of the wake behavior could be observed, a suppressed vortex shedding and an amplified wake. In [69], Jukes *et al.* provided an analysis of the effectiveness for the drag reduction. The effect of streamwise and spanwise forcing on suppressing the vortex shedding was investigated later by Kozlov *et al.* [80, 81] at a slightly larger subcritical Reynolds number ($Re = 85k$).

Separation control on airfoils at higher velocities up to $U = 62\frac{\mathrm{m}}{\mathrm{s}}$ was investigated by Little *et al.* [97], who demonstrated that the control authority of a standard DBD driven by sinusoidal voltage decreases with increasing free-stream velocity. In this work Little *et al.* compared a standard DBD driven by sinusoidal voltage with one driven by a nanosecond pulse and demonstrated the larger control authority at higher velocities of the latter. This is in good agreement with the earlier investigations of separation control with the nanosecond pulse actuator at velocities of $U = 30\frac{\mathrm{m}}{\mathrm{s}}$ from Sidorenko *et al.* [144]. Little *et al.* [97] also described the effect of the DBD plasma actuator as an active trip at pre-stall angles of attack. In Barckmann *et al.* [7], a pressure recovery in the wake of an airfoil at a higher Mach number (Ma=0.42) and angles of attack of $\alpha = 13° - 17°$ was demonstrated using spanwise and streamwise forcing plasma actuators. Separation control at high Mach numbers (Ma=0.05-0.8) with a nanosecond pulse actuator was investigated by Roupassov *et al.* [134].

Controlling the separation on the flap of an airfoil is a much more demanding task than the control of leading-edge separation, according to Melton *et al.* [104]. They observed that a higher momentum input with a zero-net-mass-flux periodic excitation is required for the separation control from a flap as compared to the control of leading-edge separation. Such a control using plasma actuators has been demonstrated successfully by Lit-

tle *et al.* [94–96] at much lower velocities ($U = 15$ to $25\frac{\mathrm{m}}{\mathrm{s}}$) compared to their leading-edge separation control investigations. They also emphasize that much stronger actuation is needed for this particular purpose than for leading-edge separation control.

In Poggie *et al.* [115] flow control was demonstrated at a higher Reynolds number of $Re = 0.9 \cdot 10^6$ to $1.7 \cdot 10^6$ and at $Ma = 0.05$ to 0.1 with separation from an inclined flap using streamwise and arrays of spanwise forcing plasma actuators. The single streamwise forcing actuator was found to be much less effective than the other actuator configurations, where a lift increase of 10% was achieved for the slower case. A decreasing control authority for the case of the higher Mach number was observed, as a result they expressed the need for actuators with higher control authority to further increase the Mach number.

Separation control with higher Reynolds numbers and moderate velocities is addressed by some other publications. Separation control from the leading edge up to $Re = 10^6$ and $U = 60\frac{\mathrm{m}}{\mathrm{s}}$ was investigated by Patel *et al.* [114]. There only a weak dependency on the Reynolds number was found for the minimum required voltage for reattaching the flow. The dependency on the leading-edge curvature and the angle of attack was more pronounced for the leading edge separation. The aforementioned comparison of a standard DBD actuator driven by sinusoidal voltage with an actuator driven by a nanosecond pulse for leading-edge separation by Little *et al.* [97] was acquired at $Re = 10^6$ and $U = 60\frac{\mathrm{m}}{\mathrm{s}}$ and demonstrates the inferior control authority of nanosecond pulse driven actuator.

These findings, especially in the higher Reynolds and Mach number range, clearly demonstrate that the control authority of plasma actuators is limited. DBD plasma actuators demonstrate efficient separation control at a lower Reynolds numbers range and moderate velocities. In a laminar flow the pulsed operation reveals an improved control performance. In this range no significant difference in the performance with spanwise or streamwise forcing plasma actuators can be seen. Whereas in a fully turbulent flow a stronger effect could be achieved with the spanwise forcing. At higher velocities and Reynolds numbers the spanwise forcing also demonstrated better performance. A decreasing control authority was observed with single streamwise forcing actuators with increasing velocities. The advantage of spanwise forcing is the elongated force region in streamwise direction. This way the duration in which the force is acting on the fluid elements is sufficiently longer than with a single streamwise forcing

actuator. Therefore the acceleration of the fluid element is stronger.

1.2 Flow Control with Plasma Actuator Vortex Generators

With the spanwise forcing electrode arrangement of plasma actuators Roth *et al.* [133] demonstrated the formation of unstable streamwise vortices. They showed with smoke-wire visualizations that with increasing voltage the development of the vortices starts earlier and is more compact. They also demonstrated vortex break down and active vortex generation using plasma actuators. The arrays of spanwise forcing actuators are hereinafter referred to as plasma actuator vortex generators (PAVG).

Since their introduction, active vortex generation using plasma actuators has recently experienced a growing interest for flow control applications. Although numerous publications are available, they focus primarily on the topic of separation control (Jukes *et al.* [72], Schatzman *et al.* [135, 136], He *et al.* [58], Grundmann *et al.* [52], Barckmann *et al.* [7], Kozlov *et al.* [80, 81] and Poggie *et al.* [115]) and parametric studies (Jukes *et al.* [70] and Wicks *et al.* [162]) for this special application. One publication that reports the use of plasma actuators for active vortex generation in laminar boundary layers concerns the damping of streaks produced by roughness elements (Hanson *et al.* [57]). Jukes *et al.* [71] investigated the formation process of a single longitudinal vortex created by means of a single spanwise forcing plasma actuator in comparison with a passive vane-type vortex generator (VG). The formation was identified as twisting and folding of the spanwise vorticity in the boundary layer of the oncoming flow. This compares to the formation of a vortex with a passive VG due to the pressure difference between the pressure and suction side of the device. With the PAVG the vorticity is continuously increasing along the actuator length; according to the elongated force region in streamwise direction.

Conventional vortex generators (active and passive) have demonstrated to be robust and efficient flow control devices, that can be utilized for several different flow control applications (as discussed in the next section).

1.3 Flow Control with Vortex Generators

Vortex generators have been applied for flow control investigations since the late 1940s and are already used in several practical situations. A broad

review about the design, applications and investigations of passive vortex generators for boundary-layer separation is provided by Lin [92]. Vortex generators to control boundary-layer separation is extensively investigated for the low-speed separation in adverse pressure gradients and also for the control of shock wave induced separation. Dependent on the flow control approach different designs of passive vortex generators are available, from cylindrical roughness elements, wishbones and the more standard vane type elements. In an array of vortex generators, two general types of the arrangements are differentiated: the co-rotating and counter-rotating VGs.

The robustness of the separation control with passive VGs was demonstrated by Lögdberg *et al.* [100] according to the relative position of the devices to the separation line. Lögdberg *et al.* also showed that the vorticity of passive vortex generators scales with the flow velocity at the tip of the devices. The advantages are, beside the robustness of the flow control, the simple and cheap design and the possibility to retro-fit these devices if required. But these advantages are accompanied by the drawback of parasitic drag. To reduce the device drag, with a height usually in the range of the boundary-layer thickness, smaller devices were suggested, without reducing the performance ([88, 92]). Another possibility to reduce the additional drag, especially when a flow control is not required, is active vortex generation. Active vortex generators like slotted or round jets were first suggested by Wallis [156] in the late 1950s.

A thoroughly parameter investigation in an adverse pressure gradient with active and passive vortex generators were performed by Godard *et al.* [47–49], with the aim to improve the passive devices in terms of skin friction and also to provide a comparison of the different types.

Beside separation control, longitudinal vortices created by passive or active devices, have been investigated for a number of different flow-control approaches. At transonic flow conditions Caruana *et al.* [18, 19] demonstrated the control of shockwave induced separation with passive VGs to suppress buffet around an airfoil. Dandois *et al.* [24], experimentally and numerically, compared buffet control with passive and fluidic VGs.

Boundary-layer control with vortex generators is another flow-control approach involving the delay of transition from laminar to turbulent. Transition delay in a 2D boundary-layer with the attenuation of Tollmien-Schlichting (TS) waves was demonstrated by Fransson *et al.* [41] and Gürün and White [55]. With counter-rotating vortices the boundary layer is deformed, resulting in streaks of higher and lower velocity; these streaks affect the growth of the TS waves.

The interaction of TS waves with streaks was investigated experimentally and numerically by Bakchinov *et al.* [6], Cossu and Brandt [22], White *et al.* [160], Fransson *et al.* [43] and Liu *et al.* [98, 99]. Further details on the conclusions from these investigations are discussed in Chapter 6.

Another transition mechanism in 3D boundary layers controlled with longitudinal vortices is the suppression of cross-flow instabilities with roughness elements. This has been successfully demonstrated by Saric [164] in experiments and numerically investigated by Wassermann and Kloker [157].

Boundary-layer control with the aim of turbulent drag reduction with large coherent structures was investigated numerically by Schoppa and Hussain in [138]. They demonstrated that small scale vortical structures are reduced by imposing counter-rotating vortices with moderate amplitude to a turbulent boundary layer, using a spacing larger than the characteristic streak spacing.

This brief overview of flow-control investigations by means of passive and active vortex generators demonstrates the applicability of VGs for a large variety of flow-control approaches. Plasma actuator vortex generators, so far majorally investigated for separation control, demonstrated their advantages as compared to the streamwise forcing actuators: the elongated force region in streamwise direction. This advantage could extend the limitation of the control authority to a larger range of flow conditions and the applicability of PAVGs for a larger variety of flow-control applications.

1.4 Outline

It is the aim of the present thesis to explore the working mechanisms and the scalability of such devices for active vortex generation in laminar boundary layers. The characterization of the influence of different parameters is investigated, as well the qualification of this active device for boundary-layer control on flat-plate wind-tunnel experiments.

The second chapter describes briefly the classification of plasmas. The involved modifications from the classical drift tubes to the gas-discharge for flow control with DBD plasma actuators are described. In a second part characterization methods are introduced to describe the features of DBD plasma actuators.

The third chapter addresses the description and characterization of the actuator configuration used in this study, involving the operating limits, consumed power, the produced thrust and the relation of the force magnitude to the force field distribution, dependent on the input parameters of

applied voltage and operating frequency.

In the next chapter (Chapter 4) the direct scaling of the actuator force production dependent on the operating conditions and the actuator setup is discussed. Furthermore an indirect scaling method of the force magnitude and the force field distribution are introduced.

The insights of the scaling are used to discuss the parameter influences for the active vortex generation in Chapter 5. There, a qualitative parameter study demonstrates the key features, necessary to generate stable streaks with longitudinal vortices by means of PAVGs in a laminar boundary layer.

Active boundary-layer control is demonstrated with the attenuation of TS waves in Chapter 6. Different array configurations to impose the streaks on the laminar boundary layer are investigated.

2 Dielectric-Barrier Discharges

In this chapter the working principle of DBD plasma actuators is discussed. A brief overview is given in Section 2.1 concerning plasma characteristics as an introduction to classify the DBD plasma actuator.

In Section 2.2 the measures for characterizing the standard actuator are introduced.

2.1 Characterization of Atmospheric Pressure Gas Discharges

Gas discharges have a long history as plasma sources in research and industrial applications. A broad introduction and overview into the topic plasma reactors and their applications is provided by Roth in the first two volumes of *Industrial Plasma Engineering* [127] and [128]. In the first volume Roth introduces the physical background and principle with the basic information on plasma physics and the physical processes important for industrial plasma sources. The physics and technology of constant/direct current (DC) and radio-frequency (RF), usually in the range of kHz to MHz, of the electrical discharge are introduced.

The gas-discharge of dielectric-barrier discharge (DBD) plasma actuators is characterized as a weakly ionized and a non-thermal, non-equilibrium plasma, dependent on the general classification of plasmas with the kinetic temperature and the number of density of charge particles. Further information about this classification can be found in Roth [127] and an overview to this topic in literature is given in [82].

The second volume *Applications to Nonthermal Plasma Processing* [128] provides a background to the principles and applications of low temperature, partially ionized plasmas. As one application example of plasma sources, electrohydrodynamic (EHD) flow control is introduced. EHD flow control is the study of the behavior of electrically charged fluids in electric fields, and it finds application in electrostatic paint spraying and electrostatic precipitators. In combination with glow discharges a *paraelectric* EHD body force arises, when the applied electric field acts on the net

charge density of the plasma. This provides a body force capable of accelerating the neutral gas to velocities up to about 10 m/s according to Roth. Different types of flow control actuators are introduced, besides the single dielectric barrier plasma actuator Roth also presented in [129].

For the DBD plasma actuators the principles of atmospheric pressure plasma sources are of importance. To describe the physical processes involved in the gas discharge of DBD plasma actuators, comparisons to the different regimes of gas discharges are made, as they occur in the well investigated classical DC intermediate-pressure electrical discharge tube, as schematically sketched in Figure 2.1. Although DBD plasma actuators are operated in atmospheric pressure and in a RF range, Raizer [124] and also Gadri and Roth [44] showed that at any given phase of the RF cycle, the discharge between the electrodes has the classical characteristics of a DC normal glow discharge.

Figure 2.1: Example for the plate-to-plate electrode configuration of a classical drift tube.

The characteristics of a drift tube are complex, since many different types of discharges can occur. The following discussion on the difference between dark, glow and arc discharge (see Figure 2.2) are based on the description of Roth [128].

Dark Discharge Very low voltages lead to a drift of the electrons produced by background radiation (background ionization regime) and a nonlinear rise in the current (A-B). The current is in the saturation regime (B-C) once all charges reach the electrodes before recombination. Once the kinetic energy of the primary electrons is sufficient for secondary electron knock-out, avalanches (Townsend discharges) occur and an exponential increase in current can be observed. Depending on the design of the electrodes, the avalanches concentrate around areas of higher electric field strength, such as sharp edges or tips in the electrodes. In this corona discharge regime (D-E), a sub-regime of the Townsend discharge, most of the avalanches concentrate in a disruptive area around the tips, since the voltage is not sufficient for neutralization of ions by secondary electron emission. The ions create a large space charge, shielding most of the electrode. Thus the

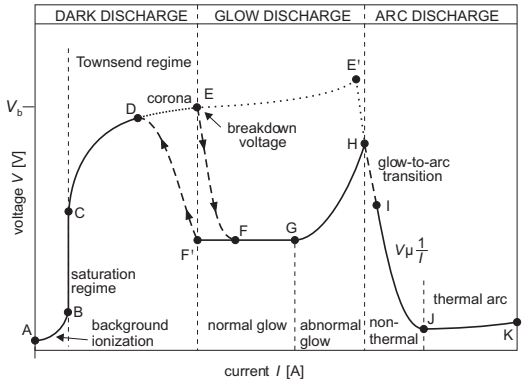

Figure 2.2: The voltage-current characteristic of the classical DC intermediate-pressure electrical discharge tube, according to Roth [128].

electric field in-between the electrode and the space charge is enhanced, whereas it is significantly reduced in-between the space charge and the second electrode. The result is a small visible area of discharges in the area of high gradients, either around the anode (positive corona) or the cathode (negative corona). This regime is the first one that could emit visible light. The discharge area is followed by a large drift zone, where either positive (positive corona) or negative (negative corona) ions slowly move towards the second electrode.

Glow Discharge Once the voltage for secondary electron emission is reached, the discharge is self-sustaining. Thus a breakdown in voltage and a transition (E-F) to the glow discharge regime occurs. In this regime the current is significantly increased over several orders of magnitude. The plasma becomes visible due to the high current, and starts to cover the cathode until the latter is fully covered at point G. The abnormal glow discharge starts just beyond that point: Since the cathode is fully covered, a strong increase in voltage is necessary to create higher currents. Due to the high dissipated power, the plasma is very bright and the electrodes are strongly heated.

Arc Discharge At even higher power levels (H-I) the glow to arc transition occurs. This is caused by thermionic emission of electrons from the highly heated electrodes. These extra electrons strongly decrease the voltage nec-

essary to maintain the discharge. Due to instabilities, the plasma forms in the shape of a hot and bright arc. The plasma is first non-thermal (I-J), since the gas temperature is still not as high as the electron temperature. At higher power levels, the dissipated energy is high enough to heat the gas towards a thermal arc at point J and a thermal equilibrium at point K.

At increasing pressure levels the regions F-G and G-H shrink such that a direct transition to arc discharge is possible.

Breakdown Voltage The breakdown voltage (V_b) required for the transition to glow discharge with a classical DC intermediate-pressure electrical discharge is a function of the pressure and electrode distance pd, as shown by Paschen [113]. These V-pd-curves or Paschen curves (schematically displayed in Figure 2.3) show an increase in V_b at large pd, (high-pressure insulation) and at some critical value of pd, V_b becomes infinite (vacuum insulation), in between, there is an optimum where a minimum voltage is required for a breakdown.

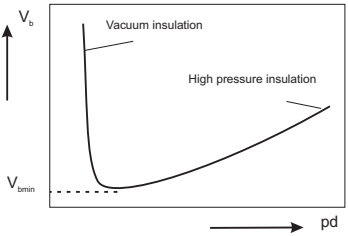

Figure 2.3: Schematic breakdown curve for a parallel plate according to Braithwaite [16].

The gas breakdown voltages by RF electric fields at a lower frequency range are very similar to those with the DC breakdown [16]. At high frequenciy (HF) ranges (above 10MHz) the breakdown voltage decreases [112]. This is explained with a careful examination of the dominant electron loss mechanism. The gas breakdown by high-frequency electric fields has been studied in detail by Brown [36]. According to Brown, the gas breakdown by HF fields occurs when the volume ionization equals the electron loss by diffusion. Based on this diffusion theory, he derived the conditions for HF breakdown similar to the Paschen curve.

By applying at least one dielectric layer in the discharge gap in-between the electrodes in the parallel plate-to-plate configuration, shown in Figure

2.4(a), the breakdown voltage V_b is reduced as well, as discussed by Gibalov *et al.* [45]. The influence is explained with the charge accumulated at the dielectric surface, which is also dependent on the permittivity of the dielectric. Gibalov *et al.* differentiate between the ignition voltage and the required voltage for maintaining the discharge, similar to plasma display panels.

2.1.1 Stable Atmospheric Pressure Gas Discharges

The discharge becomes unstable at higher pressure levels and turns into a filamentary arc immediately after breakdown. Atmospheric pressure plasma sources would be much more advantageous from the viewpoint of the cost of apparatus and the construction of a large-scale system. Since several material processing applications, such as surface treatment, etching, deposition, and surface modification or sterilization, are usually processed at low pressure. Thus several publications on the stability of atmospheric pressure plasma sources are available [76, 102, 132, 142, 143]. A critical current density is observed for all different plasma sources before the transition to arc discharge occurs. A comparison of different atmospheric-pressure plasmas, such as arcs, plasma torches, corona discharges, and dielectric barrier discharges, is presented by Schütze [139]. This comparison involves the voltage current-characteristics and the densities of oxygen species in the plasma discharges with respect to the different applications.

Since the DBD plasma actuators for flow control should be operated under atmospheric pressure and below, atmospheric pressure plasma sources are also of importance for the understanding of this device. To sustain a stable glow discharge up to atmospheric pressure some operating conditions, as for example the operating gas, electrode geometry and temperature, applied frequency or an additional dielectric layer in to the gas gap, could generate discharges in a diffuse glow regime. Von Engel [154] demonstrated in 1956 that a DC atmospheric pressure glow discharge with bare electrodes is possible. For this an intensive electrode cooling was required to suppress the glow-to-arc transition.

The operation of plasma sources at a high RF range increases the stable region of the glow discharge. Numerical investigation of the stability range of RF atmospheric-pressure glow discharges by Shi *et al.* [142] demonstrated an increase of the critical current density with increasing frequency.

Another possibility to increase the stable glow discharge region is to apply a dielectric layer in the discharge gap. Here different configurations

are available as shown in Figure 2.4. Massines *et al.* [102] investigated the stability of glow discharges theoretically and experimentally. Shi *et al.* [143] showed numerically, that the DBD is stable to very large current densities.

The dielectric barrier shields the electrodes and prevents a large current flow. The transferred charge is accumulated at the surface of the dielectric barrier and builds up a surface charge. This surface charge weakens the external applied electric field until its compensation and the discharge stops. This self-limiting behavior of dielectric barrier discharge requires the actuator to be operatedwith a pulsed DC or with an AC voltage to allow continuous plasma generation.

Besides the parallel plate-to-plate configuration with a dielectric layer in between the electrodes (cp. Figure 2.4(a)), there is also a so-called surface-discharge configuration available. With the surface discharge (SD) the electrodes are not facing each other, but rather orientated next to each other and again separated and shielded with a dielectric. Different configurations of SD plasma sources are shown in Figure 2.4(b). In this configuration one or both electrodes could be covered with a dielectric. The discharge with the SD plasma source spreads on top of the surface between the electrodes. The discharge with the plate-to-plate configuration occurs in the gas gap between the electrodes, in contrast to the SD. Consequently the plate-to-plate configuration is also referred as a volume discharge (VD). In the next section the different DBD configurations (SD and VD) are compared and discussed.

2.1.2 Dielectric-Barrier Discharges

An overview of dielectric-barrier volume discharges is presented by Kogelschatz [78], involving the history of their development, the discharge physics and industrial applications.

Usually this type of plasma source is operated at a lower RF range between $0.5 - 10$kHz [45, 123, 143] and up to 10MHz [78]. Depending on the operation condition, the discharge has a filamentary structure or appears in a diffuse glow. Operated at atmospheric pressures, the discharge usually emerges in the filamentary structure. According to Kogelschatz [78] the discharge occurs in current filaments of short duration and large numbers, also called micro discharges, as sketched in Figure 2.5. These filaments are formed by growing electron avalanches, creating a high space charge and resulting in self-propagating streamer. The discharge is inducted when applying an electric field above the breakdown voltage. Due to the fast

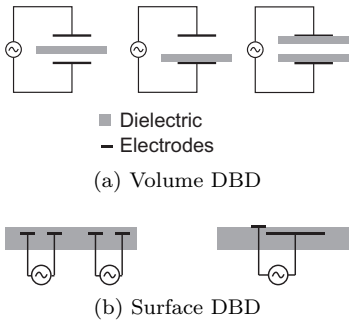

(a) Volume DBD

(b) Surface DBD

Figure 2.4: Different DBD configurations according to [45, 78, 128, 139, 155].

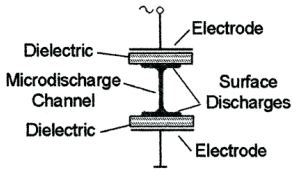

Figure 2.5: Schematic micro discharge according to [78]

moving electrons, the electrons are accumulated at the streamer head and leaving behind a tail of the slower ions. Due to a space-charge induced field enhancement between the head and the anode, further enhancement of the field around the anode is caused. The process is very fast and the positive space charge extends to the cathode very rapidly resulting in the formation of a streamer.

The charges accumulating on the surface spread on the dielectric with a substantial larger diameter compared to the discharge channel. This accumulated surface charge reduces the local electric field to such an extent that ionization stops within a few nanoseconds and the micro discharge terminates. With a still increasing applied electric field new micro discharges can develop, preferably at a location outside the accumulated surface charge, where the local electric field is not affected. Thus the filamentary discharge of VD is randomly distributed in time and space over the surface of the electrodes. This process is described by Kogelschatz [78], and Gibalov and Pietsch [45].

Gibalov and Pietsch [45] compared the VD and SD with experimental and numerical results. The VD is referred to as a pulsed discharge by Gibalov and Pietsch, whereas the SD is described as a stepwise discharge. The charge transferred in a discharge gap with a VD arrangement is connected to the design parameters, the size of the discharge gap, the thickness of the dielectric layer and the relative permittivity, for a given operating gas. The total charge during a half-period of the applied voltage will only grow in discrete steps with increasing voltage. In contrast to the VD arrangement, the charge spreads on the dielectric surface with the SD arrangement. The spatial extent of the surface charge hereby is dependent on the polarity and the amplitude of the applied voltage. While the current-voltage characteristic is mainly linear in the VD case, it is nonlinear for SD arrangements.

This difference in the discharge characteristic is also visible in the so-called Lissajous figures. The Lissajous figures for a VD and SD cycle are sketched in Figure 2.6. In the following the characteristics of the Lissajous figures and the differences with the VD and SD are discussed. In 1943 Manley [101] introduced a method to calculate the power dissipated in DBDs. Since the micro discharge current peaks are of short duration, it is difficult to measure the time-resolved current. It is more appropriate to measure the time-integrated current, the charge Q, with a probe capacitance C_p put in series with the DBD experiment. The voltage V_p across this measuring capacitor is proportional to the charge ($Q(t) = C_\mathrm{p} V_\mathrm{p}(t)$). The slope of the voltage-charge cyclogram or Lissajous figure represents the capacitance of the actuator [101]. For an ideal capacitor the Lissajous figure collapse to one line and for a resistive component the Lissajous becomes an ellipse.

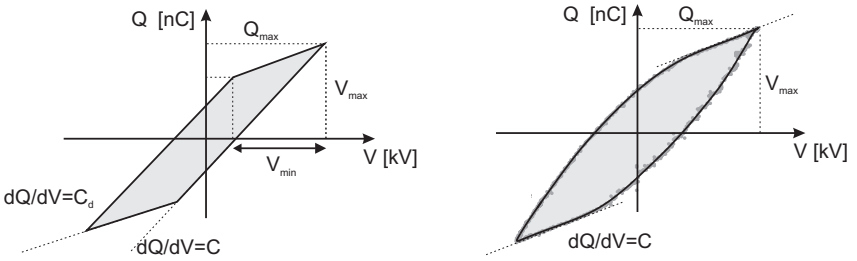

(a) Volume DBD (b) Surface DBD

Figure 2.6: Different DBD configurations according to [155].

Thus the form of a Lissajous figure, obtained from a DBD discharge cycle, contains a lot of information. The VD electrode configuration with the

dielectric layer and gas gap can be seen as a series of capacitances of the dielectric (C_d) and the gas gap (C_g), shown in Figure 2.7, as an equivalent circuit diagram [78, 124, 141]. The spark gap in Figure 2.7 represents the change in capacitance as well as the increase of the conductivity in the gap with the micro discharges. Nersisyan and Graham [108] and Kogelschatz [78] also propose a resistor, set in parallel with the gas gap, for the equivalent circuit diagram.

After ignition of the discharge, the total capacitance of the actuator changes. Thus the change in the slope of the Lissajous figure indicates the ignition and decay of the discharge and the minimum required voltage $V_{\min}$. The step-wise discharge with the SD arrangement, results in a continuous change of the slope and thus a change in capacitance of the actuator . The growth of the discharged area with the applied voltage results in growth of the capacitance. With both electrode arrangements discharge activity is limited to a certain fraction of the cycle and occurs twice during discharge cycle with the doubled frequency of the operation. The discharge cycle can be divided into the positive and negative half-cycle, starting at the extremes of the applied voltage. The time before the discharge starts are also referred to as dark periods (Manley [101]).

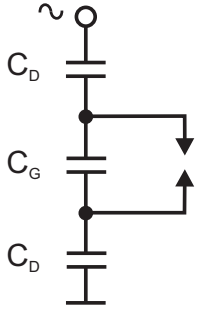

Figure 2.7: Schematic micro discharge equivalent circuit diagram according to [78] and [155]

Besides the information derived from the form of a Lissajous figure, they can be used to calculate the power dissipated in DBDs. The area of a closed loop of the applied voltage vs. charge represents the energy consumed during one period.

$$E = \oint Q(t)\mathrm{d}V. \tag{2.1}$$

The overall consumed power per discharge cycle of the actuator is proportional to the applied frequency f_p and the consumed energy E.

$$P_A = f_p \cdot E = f_p \oint Q(t)\mathrm{d}V \tag{2.2}$$

With the VD electrode arrangement no differences can be seen in the positive and negative half-cycle of the Lissajous figure. Also the asymmetric electrode arrangement of the SD reveals no difference in the slope and analysis of the effective capacitance C_{eff}, as demonstarted by Stanfield [146] and also by Kriegseis *et al.* [84]. This indicates that the same charge is transferred during the discharge in both half-cycles.

In the comparison of the VD and SD electrode arrangement carried out by Gibalov and Pietsch [45] the difference at the anode and cathode pattern on the dielectric is discussed.

Discharge patterns, derived with photographs in the visible spectrum range on the dielectric surface of a VD arrangement reveal a diffuse, homogeneous discharge distribution at the base of a VD on a dielectric anode. In contrast to this, discharge channels are visible on the surface at the base of a VD on a dielectric cathode (cf. Figure 2.8).

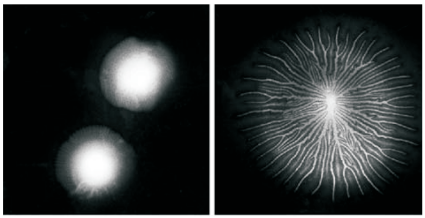

Figure 2.8: Discharge pattern at the base of a VD on a dielectric cathode and anode from Gibalov and Pietsch [45]

Similar patterns are visible for the SD electrode arrangement visualized with dust figures by Gibalov and Pietsch. The patterns for a single positive pulse and a single negative pulse on the dielectric surface also reveal a diffuse, homogeneous discharge distribution for the negative pulse and single discharge channels during the positive pulse. This structure is also identified by photographs taken by Enloe *et al.* [31], shown in Figure 2.9. In the SD arrangement the two-dimensional pattern of the discharge is spread over the upper electrode. In contrast to this, the patterns are symmetric to a central point in the VD case.

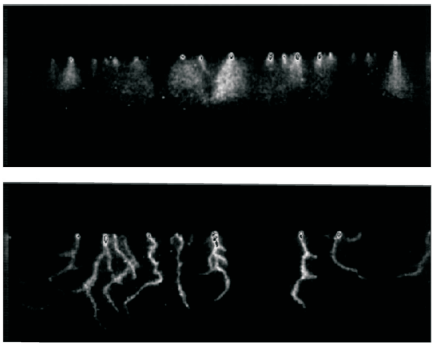

Figure 2.9: Photograph of a discharge pattern during a positive (bottom) and a negative half-cycle (top) with of a SD from Enloe *et al.* [31]

The discharge structure in both half cycles is characterized by Enloe *et al.* [31] and Orlov [111]. They distinguish a (diffuse) glow or Townsend-type discharge for the negative half cycle and a (highly filamentary) streamer type discharge for the positive half cycle.

Gibalov and Pietsch [45] pointed out, that since the distance between the single discharge channels is smaller than its extensions a two-dimensionality can be assumed, comparable to the VD case.

Push-Pull Theory versus Push-Push Theory Moreau [105] discussed the non-uniformity of the discharges in positive and negative half cycles. The question arising here is the influence of the different discharge modes on the sign of the induced EHD force. Theories exist that the plasma strongly pushes (accelerates) the flow downstream during one half cycle and weakly pulls (decelerates) it upstream in the other half cycle. Other theories suggest that the plasma pushes the flow downstream in both half cycles. Correspondingly, the two opposing theories are referred to as the push-pull theory and the push-push theory. Besides time-resolved optical measurements and the analysis of the electrical characteristics only a few efforts have been made to acquire time-resolved force measurements to answer this question. Based on numerical simulations of the discharge cycle, Font *et al.* [38] and Boeuf *et al.* [14] promoted the push-pull theory, which was supported with experimental data by Porter *et al.* [119] using an accelerometer to estimate the time-resolved thrust. On the other hand the push-push

theory is propagated by Font *et al.* [37] based on experimental and computational examinations. Also the numerical simulation by Likhanskii *et al.* [91] support this theory. He concludes that the tangential force on the gas is directed downstream in both cathode and anode half-cycles, and is created by the downstream motion of the negative ions in the cathode half-cycle and by the downstream motion of positive ions in the anode half-cycle. Numerical simulations in electro-negative gas, performed by Boeuf *et al.* [13], revealed a non-uniform force distribution in the negative half-cycle. A small region of a negative force close to the upper electrode is accompanied with a force directed downstream in the positive direction. The overall integrated force magnitude exhibits a downstream directed force in both half-cycles. Time-resolved thrust measurements of Enloe *et al.* [30] show that both half-cycles produces a downstream directed force, whereas the negative-going half cycle produces a force sufficiently larger than the positive-going half cycle.

Both cases, the push-push and the push-pull scenario, are possible according to investigations of Debien *et al.* [25], depending on the geometry of the upper electrode. A deceleration of the induced flow during the dark periods is observed, similar to the finding of Enloe *et al.* [30]. This is also supported by the work of Boucinha *et al.* [15].

Time-resolved measurements, as for example optical, electrical, and force measurements, and numerical simulation of the discharge are important for the understanding of the processes involved in the momentum coupling and the general understanding of DBD plasma actuators. For flow control investigations and for the design of DBD plasma actuators for those applications the force production can be considered as quasi-steady, since the DBD plasma actuator is operated at a low RF range and the flow is usually not receptive to those frequencies. Time-averaged optical and force measurements and the electrical characterization are appropriate methods to describe the actuator characteristic for flow control applications.

2.2 Characterization Methods for DBD Plasma Actuators

In the following section the characterization methods for the DBD plasma actuator used in this work are introduced. The measurement procedures and the processing of the acquired data are presented.

2.2.1 Electrical Characteristic

The electrical measurements were obtained using an oscilloscope (Agilent DSOX2004A) to record the applied voltage V with a high-voltage probe (Tektronix PN6015, 1000:1) and the voltage V_p across the charge-probe capacitor $C_p = 22\text{nF}$ with a low voltage probe (LeCroy PP006A, 10:1), as depicted in Figure 2.10. The applied voltage V is generated by a high voltage generator (GBS Elektronik, Minipuls 6), which is driven by a regular DC laboratory power supply and a function generator. The applied voltage V is defined as the peak-to-peak value of the measured sine wave.

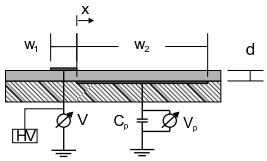

Figure 2.10: Schematic sketch of the actuator setup

The consumed power can be calculated via the well-known and established method of the Lissajous figures as presented by [101] for volume discharges. The Lissajous figure analysis allows, besides the calculation of consumed power, an additional analysis of the electrical characteristics, yieldingthe effective capacitance C_{eff} of the plasma actuator as introduced by Wagner [155] for volume discharges. The transfer to surface discharges was shown by Stanfield [146] and Kriegseis *et al.* [84]. This analysis method employing the Lissajous figure requires intense and time consuming signal processing and smoothing.

A more robust and faster analysis of the consumed power can be achieved with a differential method as presented by Bürkle [17], since no filtering or smoothing is required. Here, the power is directly calculated through the charge $Q(t) = C_p \cdot V_p(t)$.

$$P_A(t) = V(t) \cdot I(t) = V(t) \cdot \frac{dQ(t)}{dt} \tag{2.3}$$

For a set of discrete voltage and charge measurements, the mean power over N samples can be calculated using the midpoint rule for differentiation:

$$\overline{P_A} = \sum_{i=1}^{N} V_i \cdot \frac{Q_{i+1} - Q_{i-1}}{2\Delta t} \tag{2.4}$$

A comparison of results using both methods is presented in Figure 2.11. It is impossible to distinguish a difference between the two methods; revealing equivalent methods for estimating the power-consumption. The reduced complexity of the calculation of the power consumption reduces the required computational power of online monitoring and control approaches. The online monitoring and control for plasma actuators were introduced by Kriegseis *et al.* [86]. Besides the reduced complexity, the differential method offers the possibility to calculate the power consumption of an actuator operated in pulsed mode, which is the actual benefit of this method. For further information on the differential method see Bürkle [17].

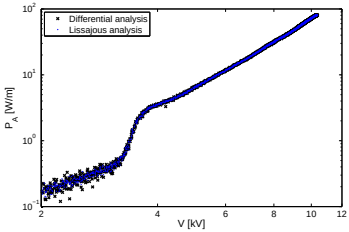

Figure 2.11: Comparison of the differential and the Lissajous figure approach for the estimation of the power consumption.

2.2.2 Light Emission

The analysis of light emission from the gas discharge is a commonly accepted method to characterize the plasma actuator. Time resolved measurements of the light emission were used to evaluate the plasma extension by Enloe *et al.* [31, 32, 34], Orlov *et al.* [110] and Hoskinson *et al.* [63]. Allegraud *et al.* [4], Gregory *et al.* [51] and Kriegseis *et al.* [83] successfully used the same approach with time averaged light emission measurements.

In the present study a CCD camera (*FlowSense 2M*) with a resolution of 1600 × 1220px and a frame rate of 15frames/s has been used to capture the luminosity of the discharge. With an exposure time of 30ms, the time-integrated spatial light emission of the discharge is acquired, since the chosen exposure time is two orders of magnitude longer than a single discharge period.

The gray value distribution $g_i(x, z)$ of the raw image i (right diagram in Figure 2.12) is averaged in spanwise direction with $N_z = 1600$ pixels, yielding the streamwise development of the light emission intensity ($g_i^z(x)$), according to Equation (2.5). The streamwise development of the light emission intensity is shown in the left diagram in Figure 2.12.

$$g_i^z(x) = \frac{1}{N_z} \sum_{k=1}^{N_z} g_i(x, z_k) \tag{2.5}$$

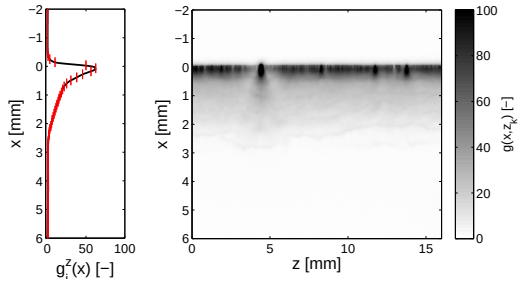

Figure 2.12: The gray value distribution $g_i(x, z)$ (right diagram) of one raw image for a plasma actuator operated at $V = 8$kV and the corresponding spanwise average $g_i^z(x)$ (left diagram)

The standard deviation of the spanwise average yields information about the spatial homogeneity of the discharge. It is shown as red horizontal error bars in the left diagram in Figure 2.12. For the case of $V = 8$kV, the standard deviation of the spanwise average is negligibly small, such that the end marker of the error bars appear as one line in Figure 2.12. Since the exposure time is large compared to the duration of the discharge cycle, the sequence of raw images contains information about the temporal homogeneity with a low-pass filtered temporal evolution.

For the average $I = 15$ frames have been used resulting in a temporal

and spanwise averaging gray value distribution:

$$G(x) = \frac{1}{I} \sum_{i=1}^{I} g_i^z(x). \tag{2.6}$$

According to the analysis of the light emission of Kriegseis *et al.* [83] the gray value distribution $G(x)$ is used to estimate the plasma extension Δx and the peak intensity $\widehat{G}$. For the analysis the background gray value G_b is subtracted from the gray value distribution ($G(x)$.

$$\Delta x = x_{max}(G(x) > G_b) - x_{min}(G > G_b).$$

$$\widehat{G} = max(G(x)) - G_b$$

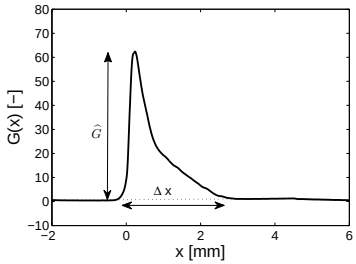

Figure 2.13: Spanwise averaged gray-value distribution $G(x)$

Beside the peak value and the plasma extension, the integral gray value GV of the light emission is used to describe the characteristics of the light emission.

$$GV = \int_{x=0}^{\Delta x} G(x)dx. \tag{2.7}$$

Gregory *et al.* [51] attempted to estimate the number of ions in the discharge with the integral gray value. These data have been normalized with the light emission intensity, since it is a number with arbitrary units. Gregory *et al.* showed that the integral gray value increases with the consumed power but a close correlation of the integrated gray value and the consumed power was not demonstrated.

2.2.3 Thrust Measurements

For the determination of the produced force, the thrust of the actuator was measured directly by means of a weight balance. This technique is convenient and well established, it has been used in a number of studies [1, 2, 28, 35, 51, 60, 61, 83, 118, 147, 151, 152]. The produced thrust F_t should not be understood as the produced body force F_b, as already described by Kriegseis *et al.* [83], as it is reduced by the wall-friction force term. The wall-friction force term depends strongly on the velocity gradient close to the wall and thus the induced wall-jet thickness. These might be affected by a change of the actuator configuration. Nevertheless, the produced thrust F_t corresponds to the utilizable part of the force, therefore it represents a good measure of the effectiveness of an actuator.

The plasma actuator is mounted on an acrylic plate, which is connected to a weight balance (WB) *(KERN PCB 250-3 precision balance, accuracy 1 mg)* using a rocker arm $H_1/H_2 = 1:4$ to amplify the actuator thrust, as depicted in Figure 2.14. The balance and rocker arm were identical to those used in Kriegseis *et al.* [83], except for the increased rocker arm ratio. The increased ratio of the amplification of the produced thrust enables measurements at lower voltage levels. The rocker arm ratio cannot be enlarged indefinitely, since perturbations from the surrounding air and vibrations will also be amplified, resulting in deterioration of the signal-to-noise ratio.

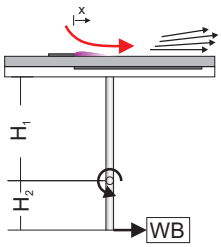

Figure 2.14: Schematic sketch of the experimental setup for the thrust measurements.

To estimate the produced thrust F_t, the actuators were repeatedly turned on and off. The difference in the weight-balance signal ($W(t)$) between the on and off periods was averaged over several iterations ($\overline{\Delta W}$). The thrust term was calculated with the rocker arm ratio, the force of gravity and the averaged difference in the weight-balance signal:

$$F_t = \frac{H_2}{H_1} \cdot g \cdot \overline{\Delta W}, \tag{2.8}$$

2.2.4 Indirect Force Measurements

An alternative to these direct measurements is provided by the estimation of the momentum added to the flow by measuring the resulting velocity distribution. The velocity distribution for this determination is measured with Particle Image Velocimetry (PIV). The force acting on the flow is calculated based on fluid mechanic balance equations. The plasma-actuator force contributes an additional source term to the governing equations.

Integral Approach For this estimation different methods are available. The first method is an integral approach resulting in a force magnitude and the second is a differential approach yielding also the force field distribution besides the force magnitude. The integral approach is based on a control volume (CV) around the discharge region regarding the momentum balance equation at the boundaries of the CV, as shown in Figure 2.15. Since the force is assumed to be two-dimensional the force magnitude is calculated per unit length L of the actuator.

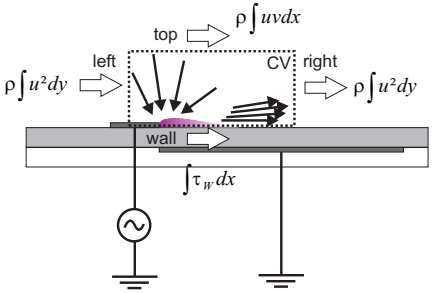

Figure 2.15: Sketch of the control volume as used for the force estimation.

$$F_x/L = \rho \int_{\text{right}} u^2 \, \mathrm{d}y - \rho \int_{\text{left}} u^2 \, \mathrm{d}y + \rho \int_{\text{top}} uv \, \mathrm{d}x + \int_{\text{wall}} \tau_w \, \mathrm{d}x \tag{2.9}$$

The sum of the first three terms on the right side of Equation (2.9), corresponds to the thrust induced by the plasma actuator. Together with

the wall friction, the last term on the right side of Equation (2.9), the body force magnitude can be calculated.

The relative share on the total force is not equal on all boundaries, the major contribution is given by the friction term and the momentum at the right boundary. This approach was successfully applied by several research groups [27, 62, 79, 153], although some neglected the influence of one or more boundaries.

Differential Approach The differential approach is based on the Navier-Stokes equation, where the plasma-actuator force contributes an additional source term. Wilke [163] demonstrated the procedure for the estimation of the body-force distribution for DBD plasma actuator and the required simplifications. Another differential approach for calculating the force field is based on the vorticity equation, as shown by Albrecht *et al.* [3]. A comparison of all the different approaches is given by Kriegseis [87].

In the present work the Navier-Stokes equation is used to estimate the force field in its magnitude and distribution. The Navier-Stokes equation in two directions with the additional source term contributed by the plasma actuator force can be written as:

$$f_x - \frac{\partial p}{\partial x} = \rho\left(u\frac{\partial u}{\partial x} + v\frac{\partial u}{\partial y}\right) - \eta\left(\frac{\partial^2 u}{\partial x^2} + \frac{\partial^2 u}{\partial y^2}\right), \tag{2.10a}$$

$$f_y - \frac{\partial p}{\partial y} = \rho\left(u\frac{\partial v}{\partial x} + v\frac{\partial v}{\partial y}\right) - \eta\left(\frac{\partial^2 v}{\partial x^2} + \frac{\partial^2 v}{\partial y^2}\right) \tag{2.10b}$$

These equations are not sufficient on their own, since only two equations exists to determine the four unknowns, the force densities f_x, f_y and the pressure gradients. Therefore further assumptions have to be made. Wilke [163] assumed that the force term f_i is of at least one order of magnitude larger than the pressure gradients over the entire control volume, i.e.

$$|f_i| \gg \left|\frac{\partial p}{\partial x_i}\right|. \tag{2.11}$$

Consequently, the pressure gradients are neglected

$$\frac{\partial p}{\partial x_i} := 0 \tag{2.12}$$

and the two remaining unknowns f_x and f_y can be calculated according to

$$f_x(x,y) = \rho\left(u\frac{\partial u}{\partial x} + v\frac{\partial u}{\partial y}\right) - \eta\left(\frac{\partial^2 u}{\partial x^2} + \frac{\partial^2 u}{\partial y^2}\right), \tag{2.13a}$$

$$f_y(x,y) = \rho\left(u\frac{\partial v}{\partial x} + v\frac{\partial v}{\partial y}\right) - \eta\left(\frac{\partial^2 v}{\partial x^2} + \frac{\partial^2 v}{\partial y^2}\right). \tag{2.13b}$$

This assumption has been verified by Wilke [163] with reverse numerical simulation of the induced flow field, using the estimated body force distribution as an input parameter.

For the determination of the velocity field, a commercial high-speed PIV system comprising a *Litron* Nd:YLF ($\lambda = 527$nm) dual-cavity laser and a *Phantom V12* high-resolution camera (12 bit, maximum resolution 1280×800 pixels) was used, which was operated in single-frame mode at a repetition rate of 10k frames per second (fps) and a pulse duration of 150ns.

The laser was synchronized with the operating frequency f of the plasma actuator. Thus, the calculated velocity field resembles the induced velocity averaged over one discharge cycle. This could reduce the fluctuations between the single estimated vector fields. Since a frequency shift between the operating frequency of the plasma and the laser pulse frequency would result in a different acceleration of the flow among the single estimated vector fields. The mean velocity would not be affected with adequate large number of images, but the standard deviation would be increased.

This high repetition rate with 10k fps demanded a reduction of the spatial resolution and the bit resolution, down to 800×600 pixels and 8 bit, respectively.

Additional measurements in double-frame mode were acquired to measure the temporal evolution of the flow field with a phase-locked average. Thus a time delay of the two laser pulses of $\Delta t = 10$ and 20μs were used to divide the discharge cycle into 10 and 5 bins, alternatively. With the double-frame mode it was required to reduce the repetition rate to 5k fps, resulting in a phase-locked average of every other discharge cycle.

A reversely mounted 120mm *SKR SYMMAR* lens is used according to the setup described in Kriegseis *et al.* [87], with 4 distance tubes of 75mm length, giving a field of view (FOV) of $6.9 \times 5.2\text{mm}^2$. To reduce reflections on the surface of the actuator, the laser sheet was aligned parallel to the surface, as shown in Figure 2.16. The plasma actuator was operated in a closed acrylic-glass containment ($450 \times 325 \times 445\text{mm}^3$) with quartz-glass windows to assure good optical accesses for the laser-light sheet and

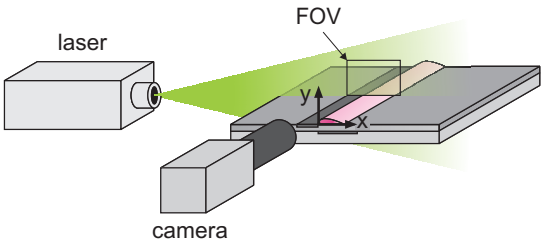

Figure 2.16: Sketch of the experimental PIV setup.

the camera. The containment was seeded with Di-Ethyl-Hexyl-Sebacat (DEHS) aerosol (mean droplet diameter 0.9μm).

The influence of the electric field on the seeding particle was investigated by Boucinha *et al.* [15]. A comparison of different seeding particles (olive oil, DEHS and incense) with an intrusive measurements method to estimate the velocity. Boucinha *et al.* demonstrated that olive oil and DEHS do not show a significant difference, whereas the use of incense as seeding particles lead to incorrect veocity values.

Studies by Kim *et al.* [77] with alumina particles as seeding showed no difference with a direct experimental comparison of the seeding particle-density distribution in the presence and absence of an applied electrical field. They report a negligible influence of seeding particle charging on the resulting velocity measurements. This conclusion is confirmed by theoretical estimations with DEHS particles of Wilke [163].

PIV Data Processing The velocity distributions were calculated from the raw data using commercial software (Dynamic Studio v3.4). To reduce the signal-to-noise ratio (SNR) in the images, the image mean was subtracted from the raw images. Rectangular interrogation areas (IAs) with a final/initial size of $32 \times 8/256 \times 64$ and pixels $64 \times 8/512 \times 64$ pixels, dependent on the particle shift with the different applied voltages. The overlap of the IA was chosen as $75\% \times 50\%$ in the vertical and horizontal directions respectively. The size of the IAs were chosen to fulfill the requirements of

calculating a wall jet's velocity profile with the strong wall-normal velocity gradients ($\mathrm{d}ui/\mathrm{d}y, \mathrm{d}ui/\mathrm{d}x$) and high wall-parallel velocities ($u \gg v$).

The flow fields were calculated with a multi-grid cross-correlation algorithm ('adaptive correlation'). Outliers were eliminated using a range validation with limits two times larger than the estimated range of the mean velocity.

Kriegseis[82] demonstrated that at least 10^3 correlated flow fields are required to assure statistical significance of the averaged data $u_i(x, y)$. Thus a sufficiently large number (N=5-10k) of images were used for the flow field estimation.

3 Characterization of DBD Plasma Actuators

In this chapter the plasma actuator as used in this work is characterized using the previously described methods. The standard plasma actuator is a single DBD plasma actuator comprising two copper electrodes and a polyimide dielectric. The dimensions of the upper and lower electrodes, which were made of self-adhesive copper tape, had a thickness of $d_e = 35\mu$m and a width of $w_1 = 2$mm and $w_2 = 10$mm, for the upper and lower electrode respectively. The actuator setup is shown in Figure 2.10. The electrodes were arranged without a horizontal overlap or gap and were separated by the dielectric layer with a thickness of $d = 0.3$mm. *Cirlex*, a DuPont Kapton® polyimide laminate, was used as dielectric material for the standard configuration.

3.1 Operation Limits

The operating range of a plasma actuator, in which a constant two-dimensional body force can be assumed, is limited. The lower limit is determined by the discharge onset and the upper limit by the start of filamentary discharge. Beyond both limits a spatially or temporally inhomogeneous discharge occurs. Gibalov and Pietsch [45] regarded the filamentary structure of the micro discharges as two-dimensional, in consideration that the spanwise distances in the filamentary structure was substantially smaller than its extension.

3.1.1 Lower Limit - Discharge Onset

For some flow control applications (e.g. boundary-layer control) small forces are required. This requires operating the actuator just above the discharge onset, when a spatially and temporally homogeneous discharge is achieved. For the model development of numerical investigations it is also essential to know when the discharge onset occurs.
The analysis of the voltage-power diagram reveals three discharge regions, a

passive, a transition and a homogeneous-discharge region. These discharge regions are characterized by different slopes in the logarithmic voltage-power diagram, as shown in Figure 3.1. To identify the different regions the standard actuator was operated over a large voltage range ($V = 0 - 13\text{kV}$). Within the passive region the consumed actuator power is proportional to the voltage with the power of two $P_A \propto V^2$. In the passive regime the actuator does not produce a discharge and therefore behaves electrically like a simple capacitor. The power losses for a capacitor operated at an AC voltage is dependent on the frequency f, the phase-shift angle $\tan\delta$ of the voltage and current, the capacitance C and the square of the applied voltage V^2 [59].

$$P_L = \frac{V^2 \cdot \tan\delta}{2\pi f \cdot C} \tag{3.1}$$

Roth *et al.* [132] proposed a heating coefficient K, and described the power losses as dielectric heating $P_L = KV^2 f$. To verify the passive element behavior and to distinguish between the passive power losses in the dielectric and the consumed power with the gas discharge, the same actuator was completely encapsulated with resin to prevent a gas discharge and it was operated in the same voltage range. In Figure 3.1 the voltage-power characteristics for the encapsulate actuator is shown in gray. In the lower voltage region - or passive region - both actuators, the normal and the encapsulate one, have the same power law $P_A \propto V^2$. The encapsulated actuator follows this power law over the complete range of voltages. A small parallel shift in the voltage-power characteristics is observable for the encapsulate actuator. This is due to the change in the capacitance of the actuator owing to the larger dielectric constant of the resin compared to the air which usually surrounds the electrodes.

The transition region starts when the voltage-power characteristics of the encapsulated actuator and the normal actuator diverge. This region is characterized by a spatially and temporally inhomogeneous discharge, as shown in Figure 3.2. The start of the visible discharge occurs at particular points along the contact line between the two electrodes, where the electric field is locally strong enough for a breakdown due to the spike effect of imperfections at the upper electrode.

A single snapshot of the light emission $g_i(x, z)$ for an applied voltage of $V = 4.0\text{kV}$ is shown in Figure 3.2(a). With increasing voltage, the number of the single discharge points increases and grows to a spatially homogeneous discharge line. Within this region the exponent of the power law is strongly increased due the shrinking part of the passive electrode

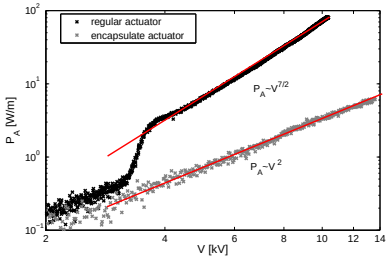

Figure 3.1: Voltage-power diagram for an encapsulated and regular actuator

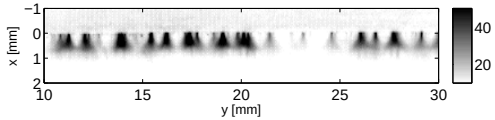

(a) Spatial gray value distribution $g_i(x, z)$ of a single raw image

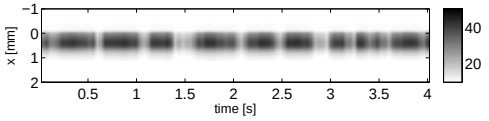

(b) Temporal evolution $g_{z,i}(x)$

Figure 3.2: Temporal and spatial distribution of the gray value at $V = 4.0$kV

area. In this state the discharge is very sensitive to small fluctuations of the applied voltage and environmental conditions, resulting in a temporally inhomogeneous discharge. This can be seen in the temporal evolution of the spanwise averaged gray value $g_{z,i}(x)$ shown in Figure 3.2(b) for the same applied voltage of $V = 4.0$kV. In this region a power-law correlation is not useful, since the extension of the transition process strongly depends on the geometrical precision of the actuator setup and the electrode edge.

In Figure 3.3 the voltage-power diagram and the corresponding sum of the standard deviations of the light emission $g_i(x, z)$, from the spanwise

average and the average over the set of raw images, normalized with the maximum are shown. In the region of the transition a peak in the sum of the standard deviations can be seen, whereas a local minimum can be identified when the transition is complete. With a further increase of the applied voltage the inhomogeneity of the discharge increases again, indicating a growth of filaments in the discharge.

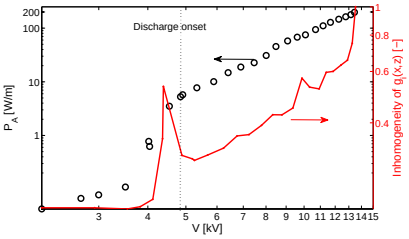

Figure 3.3: Voltage-power diagram for the standard actuator at $f_p = 10\text{kHz}$ (○) and corresponding sum of the standard deviations of the gray-value distribution $g_i(x, z)$ (red line)

Analogue to the identification of the onset of the homogeneous discharge with the voltage-power diagram, the gray value distribution of the discharge could be used to distinguish the completion of the transition. The completion of the transition region is indicated with a dotted line in Figure 3.3; here the value of the standard deviation reaches a local minimum and the slope voltage-power characteristic changes, followed by the last region, the homogeneous discharge. The voltage-power characteristic in the homogeneous discharge region is described by the power law $P_A \propto V^{7/2}$ [132]. The discharge onset and the beginning of the transition region strongly depends on the actuator setup and is shifted to higher voltages with increasing dielectric thicknesses.

Besides the precision of the electrode alignment and the electrode edge, the degree of wear influences tremendously the start of the discharge onset. The voltage-power diagram in Figure 3.1 and voltage-power diagram in Figure 3.3, with the corresponding spatial and temporal distribution of the gray value in Figure 3.2, are acquired with the same actuator at a different level of wear. With a longer duration of operation the exposed copper electrode shows an increasing grade of oxidation on the surface and dirt particles from the surrounding air are accumulated at the edge of the

electrode. This oxide layer and accumulated dirt act like an additional insulation. In Figure 3.4 a comparison of different voltage-power diagrams at a different degree of wear for the standard actuator is shown. An increase of the onset voltage with an increasing sign of usage is observed.

After polishing and cleaning of the upper electrode the original characteristic of the actuator is restored.

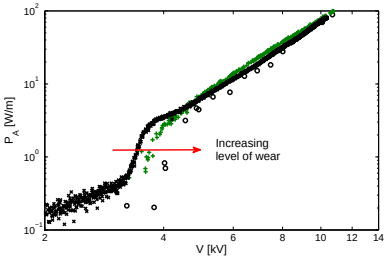

Figure 3.4: Voltage-power diagram for the standard actuator at $f_p = 10$kHz at different levels of wear.

For a clean or new standard actuator the transition starts at $V = 3.2$kV and is complete at $V = 3.9$kV. With a certain degree of usage the transition region can be shifted to a range of $V = 3.5$kV to 4.5kV.

This effect is not advantageous for the operation of an actuator just above the discharge onset, when small forces are required. Since a different degree of wear does not solely affect the force production at a low voltage level, rather it influences whether a force will be produced or not. Thus careful observation of the applied voltage and the consumed power are essential to assure comparable and repeatable results, when the actuator is operated close to the lower voltage limit.

3.1.2 Upper Limit - Filamentary discharge

A saturation of the wall-jet velocity to a maximum of $U = 8$m/s was reported by Boeuf *et al.* [14] and Moreau *et al.* [106]. Thomas *et al.* [147] reported a saturation of the produced thrust and referred this saturation to the onset of a filamentary discharge with the maximum thrust and increased power dissipation. The formation of those filaments is described to be dependent on the local concentration of electric field lines, which is comparable to the effect of a lower current density.

Thomas *et al.* [147] and Durscher *et al.* [27] observed a shift in the onset voltage of the filamentary discharge by changing the capacitance of the actuator. This was as well referred to as a change of the local concentration of electric field lines.

Roth *et al.* [130] described the onset of the saturation to be dependent on the operating frequency f. Thus the formation of the filaments is not solely dependent on the local concentration, but also on the consumed power.

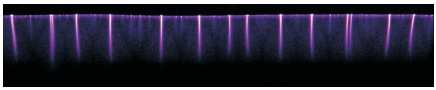

Figure 3.5: Image of large-scale filaments in the glow discharge of a DBD plasma actuator

From this it can be concluded that besides the actuator setup, the operating conditions, including the operating frequency, influence the formation of filaments.

The filaments are not related to the micro-scale filaments involved in the barrier discharge as described in Section 2.1.2, since micro-scale filaments have a duration of only fractions of microseconds and a spatial extension of a few hundred μm in width. They would thus not be visible for the unaided eye. These filaments are referred to as large-scale filaments. An image of the filamentary discharge can be seen in Figure 3.5. They are described as a thermal instability by Bürkle [17], where a theory of the development of thermal instabilities is formulated.

The onset of the filamentary discharge with the standard actuator operated at $f = 10\text{kHz}$ was determined to occur at an applied voltage of approximately $V = 11\text{kV}$. This point can also be identified as a second peak in the standard deviation of the temporal and spatial gray-value distribution shown in Figure 3.3. This second peak is less pronounced since the contribution of temporal standard deviation is less distinctive in this operation point.

Regarding the voltage-power characteristic of $P_A \propto V^{7/2}$ no change was observed with the onset of the filamentary discharge (cp. Figure 3.1), whereas a change in the temperature distribution, captured with an infrared camera (*Optris PI160*), was detected as shown in Figure 3.6. The camera used in the temperature experiments had a resolution of $\pm 1\text{K}$. The instabilities are visible in the heat distribution through a local increase of the temperature. The spatial temperature distribution on the dielectric

surface of the actuator gives good insight into the local power consumption, since most of the electric power consumed by a plasma actuator is released into heat, according to Roth *et al.* [131].

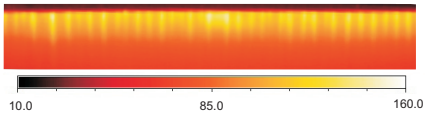

Figure 3.6: Steady state temperature distribution of the actuator surface with a voltage amplitude of $V = 14$kV in quiescent air[17].

The evolution of the surface temperature with increasing applied voltage is depicted in Figure 3.7. Between $V = 4$kV and $V = 10$kV, the glow is stable and homogeneous; for higher voltages the temperature was recorded in the filaments and in the region in-between. The temperature increases strictly monotonically and the temperature of the filaments exceeds that of the glow. With increasing voltage the temperature difference between the instabilities and the glow region in-between grows. The surface temperature of the stable glow is extrapolated towards voltage amplitudes with filamentary discharges using an exponential fit in Figure 3.7.

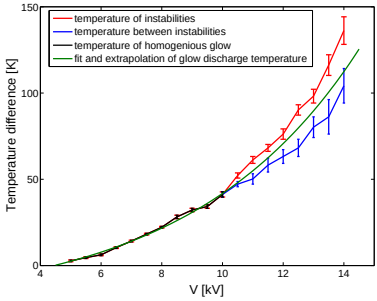

Figure 3.7: Temperature differences between the surface of the actuator and the ambient quiescent air for different voltage amplitudes [17].

The temperature within the filaments always exceeds the value of a hypothetically undisturbed system, whereas the temperature in-between the filaments is always lower. This indicates a larger local current density within the filaments. In combination with the observations of the unchanged

voltage-power characteristic within the filamentary discharge regime and the decreased surface temperature between the filaments, a decreased local current density between the filaments can be presumed.

The effect of the spatially inhomogeneous discharge on the induced velocity distribution was measured with a pitot tube. The pitot tube was positioned in the wake of one instability and downstream of the glow region in-between the instabilities separately. The pitot tube was made out of glass to ensure electric insulation from the plasma discharge and was connected to a differential pressure transducer (*Setra Model 267*). The glass tube had an inner diameter of 0.6mm. The applied voltage was set to $V = 15\text{kV}$ at a frequency of $f = 10\text{kHz}$. The measurement was repeated at different downstream positions in order to find the maximum flow velocity of both measurement positions. The measured velocity of the induced wall-jet in the glow zone between the instabilities ranges from $u = 5.2\text{m/s}$ to 6.1m/s, whereas it ranges from $u = 6.7\text{m/s}$ to 7.2m/s within the instabilities. The induced velocity of the filaments clearly exceeds that of the space in-between.

Regarding the definition of Gibalov and Pietsch [45] and the observed distances between the filaments compared to the extension of the plasma in Figure 3.5, the flow produced by a plasma actuator with a filamentary discharge cannot be considered as two-dimensional.

Besides the three-dimensional flow induced by a filamentary discharge, this operation point is not favorable for further reasons. The filaments significantly damage the actuator due to massive heating and electro erosion of the dielectric barrier. During electro erosion, molecules of the dielectric barrier are detached from the solid state material due to ion collision.

3.1.3 Summary - Operation Limits

In this configuration, with a given dielectric material and thickness, the operation range where a constant two-dimensional body force can be assumed, associated with a spatially and temporally homogeneous discharge distribution, is restricted to an applied voltage of $V = 4.5\text{kV}$ up to $V = 10\text{kV}$. The determination of the discharge onset and the start of a filamentary discharge provide the lower and upper limit of the usable operating range.

3.2 Induced Thrust

In Figure 3.8 the produced thrust F_t of the standard actuator operated at $f_p = 10\text{kHz}$ is shown in its relation to the voltage (Figure 3.8(a)) and consumed power (Figure 3.8(b)). The thrust is normalized with the actuator length L.

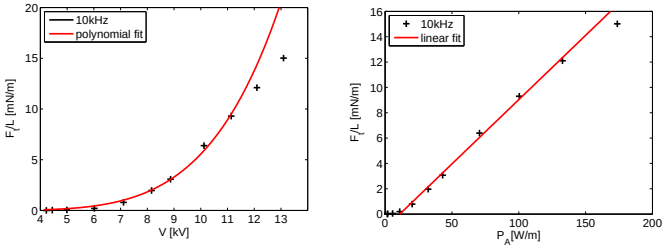

(a) Thrust-voltage diagram (b) Thrust-power diagram

Figure 3.8: Evolution of the induced thrust in dependency of the electrical characteristics, voltage and consumed power.

The actuator was operated in a range of voltages from $V = 4\text{kV}$ up to $V = 13\text{kV}$. For lower voltages $V < 11\text{kV}$, an increasing slope for the thrust F_t is observed ending in a steeper slope at higher voltages, whereas an almost linear dependency with the consumed power can be seen. The polynomial fit (red) in Figure 3.8(a) is plotted with a correlation of $F_t \propto V^5$. At higher voltages, above $V = 10\text{kV}$, larger discrepancies between the thrust measurements and the fitted curve can be seen. The linear fit (red) in Figure 3.8(b) yields a correlation $F_t \propto P_A$.

A linear relationship of the produced thrust with the applied voltage ($F \propto V$) was identified by Kriegseis *et al.* [83] at higher voltages (between $V = 8$ and 12kV), whereas a dependency of $F \propto V^{7/2}$ was identified by Thomas *et al.* [147]. At higher voltages, above the onset of a filamentary discharge, Thomas *et al.* described the relation as $F \propto V^{2\frac{3}{10}}$.This discrepancy between the observed thrust-voltage relations and data found in the literature, might be irritating at the first glance; however the results of the thrust-voltage relations might be related to the investigated range of voltages. Secondly, the actuator setup and the size of the body-force region might affect thrust-voltage relations, since the thrust F_t is reduced by the wall-friction force term. This influence will be discussed more in detail in

Section 3.4.

The relation of the produced thrust and the consumed power is identified as a linear relation by Poon *et al.* [118] and Enloe *et al.* [29] and is in good agreement with the present observation.

The fluid mechanic effectiveness ($\eta^*_{FM} = \frac{F_t}{P_A}$), according to the definition of Kriegseis *et al.* [85], is shown in Figure 3.9 as a function of the applied voltage.

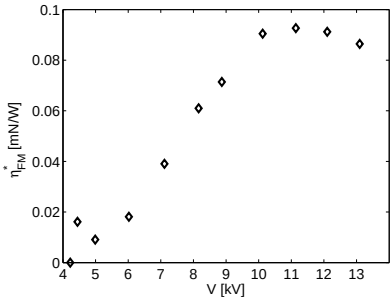

Figure 3.9: Fluid mechanic effectiveness η^*_{FM} of the standard actuator in dependency of the applied voltage

The effectiveness increases with increasing voltage up to a maximum at around $V = 10 - 11$kV, at higher voltages no further increase can be distinguished. This saturation of the thrust and the decreasing effectiveness, is in good agreement with the start of the filamentary discharge as discussed in Section 3.1.2 and with the described effect of the saturation by Thomas *et al.* [147], Durscher *et al.* [27], and Roth *et al.* [130].

3.3 Velocity Field Distribution

The PIV based flow field measurements serves as the basis for the differential approach of the force field estimation. For the PIV measurements the standard actuator was operated at voltages ranging between $V = 4.5 - 12$kV and a constant operating frequency of $f_p = 10$kHz.

The induced flow field of an actuator operated at $V = 7$kV in quiescent air is shown in Figure 3.10. The maximum achieved velocity for this operation condition is $u_{\max} = 2.58$m/s.

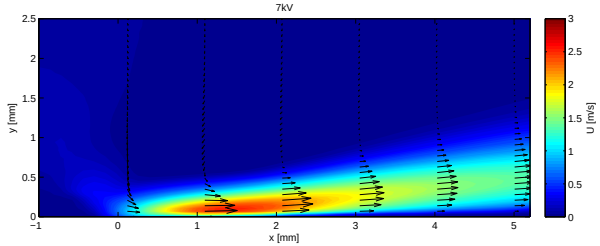

Figure 3.10: Velocity distribution of the induced flow field of a standard actuator operated in quiescent air at $V = 7$kV.

With increasing voltages the maximum induced velocity increases linearly (c.p. Figure 3.11). This linear increase of the induced velocity was also reported by Roth *et al.* [130], Abe *et al.* [1], Moreau *et al.* [106] and Joilbois *et al.* [66], whereas others (Murphy *et al.* [107], Orlov *et al.* [111] and Jukes *et al.* [67]) report an increase of the maximum induced velocity following an power-law of $u_{max} \propto V^{12/5}$ to $V^{7/2}$.

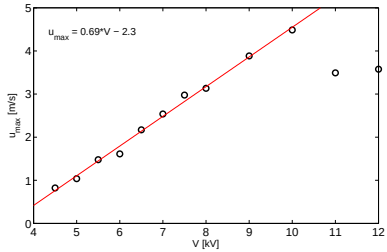

Figure 3.11: Maximum induced velocity of a standard actuator operated in quiescent air.

The linear increase is observable up to a voltage of $V = 10$kV, at higher voltages the maximum induced velocity decreases in these measurements. This might be caused by the small FOV of 6.9mm in streamwise direction and the long time between the frames taken in the single-frame mode. The combination of higher spatial resolution and a long time between the laser pulses results in a large particle shift around 50 pixel for the case of $V = 10$kV. An even larger particle shift occurs at higher voltages.

Additionally the onset of a filamentary discharge, starting at $V = 11$kV

for this type of actuator, causes a spanwise velocity component. In combination with the large particle shift, this leads to a corresponding particle loss out of the measurement plane. Therefore the measurements above $V = 10$kV are not taken into account for characterizing the induced velocity field and the estimated force distribution based on these measurements. This clearly demonstrates the limitation of this setup, since the advantages of a small FOV and the synchronization of the laser and the plasma discharge cycle are associated with the drawback, that the maximum resolvable velocity is limited.

The velocity distributions of the u velocity component are shown in Figure 3.12 for the applied voltages between $V = 4.5$ to 10kV.

The induced wall jet is accelerated close to the wall and up to the position of the maximum velocity the wall jet does not separate from the wall. Beyond that position the flow decelerates and the wall jet lifts away from the wall.

In Figure 3.13 the wall-jet profiles at the position of the maximum induced velocity are shown for these cases. It can be seen that the wall-jet thickness increases with the applied voltage as well as the induced velocity. In contrast to this, the wall-normal position of the wall-jet maximum do not appear to be strongly influenced.

Further insights can be drawn from the streamwise position of the maximum induced velocity $x|_{u_{\max}}$ and the characteristics of the wall-jet profiles. Both characteristics are analyzed more in detail in the next paragraphs.

Streamwise Position of the Maximum Induced Velocity The velocity profiles evaluated at the position of the maximum induced velocity $x|_{u_{\max}}$ are shown in Figure 3.14. Here a linear increase of the x-position with increasing applied voltage can be seen. In comparison to the position of the maximum induced velocity the plasma extent Δx, derived from optical measurements of the light emission as introduced in Section 2.2.2, are shown. The similar characteristics of the plasma length Δx and the position of the maximum induced velocity $x|_{u_{\max}}$ is obvious.

The maximum velocity is expected to correlate with the extension of the force field (Δx_F), since the fluid is accelerated within this region. In Figure 3.14 the correlation is shown and corroborate the results of Kriegseis *et al.* [87], who demonstrated that the plasma extent Δx correlates with the spatial extent of force field.

It can therefore be concluded that the plasma length Δx and the position of the maximum induced velocity $x|_{u_{\max}}$ serve as a measure for the

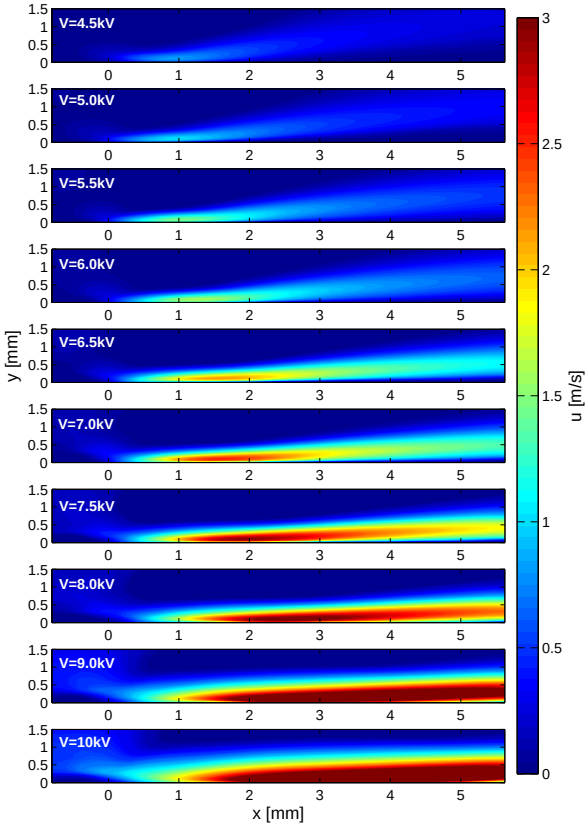

Figure 3.12: Velocity distribution of the induced flow field of a standard actuator operated in quiescent air at increasing voltages.

dimension of the force field.

Wall-Jet Profile Characteristics As has been demonstrated earlier the wall jet is accelerated close to the wall. The wall jet thickens and the induced velocity increases with increasing voltage. The wall jet is accelerated up to the end of the discharge region. Further downstream the velocity de-

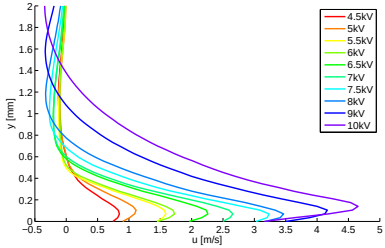

Figure 3.13: Velocity profiles at the position of the maximum induced velocity at different applied voltages.

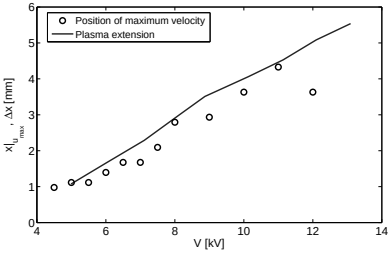

Figure 3.14: Downstream position of the maximum induced velocity in comparison to the plasma extent derived from gray value distributions.

creases again and the wall jet lifts away from the wall. The question arising here is whether the force field influences the characteristics of the wall-jet profiles?

For better comparability the wall-jet profiles are normalized according to the definition of Glauert [46]. The velocity is normalized with the maximum value of the wall jet, as expressed in Equation (3.2). The wall-normal distance is related to the wall-jet thickness (cp. Equation (3.2)), which is defined according to Glauert [46] as the position where the jet has 50% of the maximum velocity ($\delta_{1/2} = y|_{\frac{1}{2}\cdot u_{\max}}$). Glauert differentiated between the characteristics of a laminar and turbulent wall jet. According to this definition, the typical wall-normal distance for a laminar wall jet is around $\delta_{1/2} = 0.5$. A turbulent wall jet typically has a position of the wall-jet velocity maximum at $\delta_{1/2} = 0.25$.

$$u^* = \frac{u}{u_{\max}} \quad \text{and} \quad y^* = \frac{y}{\delta_{1/2}}. \tag{3.2}$$

The laminar nature of the induced wall jet of a DBD plasma actuator was demonstrated by Roth *et al.* [131], by comparing the theoretical laminar wall-jet profile of Glauert with experimental data. This is in good agreement with the findings of Jukes *et al.* [67], Thomas *et al.* [147], Kriegseis *et al.* [82] or Murphy and Lavoie *et al.* [107]. They demonstrated the self-similarity of the non-dimensional wall-jet profiles. Some discrepancies towards the laminar wall-jet profile and varying wall-normal distances of the maximum velocity where identified for different applied voltages and wall-jet profiles evaluated at fixed locations downstream of the upper electrode.

In Figure 3.15(a) the non-dimensional wall-jet profiles at the position of the maximum induced velocity are shown for different applied voltages.

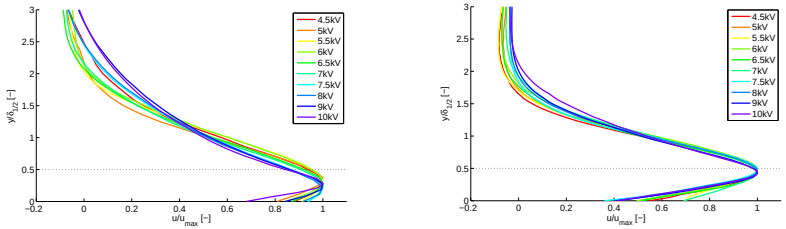

(a) Normalized velocity profiles at the position of the maximum induced velocity $x = x|_{u_{max}}$

(b) Normalized velocity profiles at $x = x|_{u_{max}} + 2.5$mm

Figure 3.15: Scaled velocity profiles of different applied voltages.

The thickness of the wall jet-profiles and the maximum induced velocity increase with increasing applied voltages, whereas the wall-normal distance of the maximum induced velocities is more or less constant (cp. Figure 3.13).

This results in a decrease of the non-dimensional wall-normal distance, when the wall-jet profiles are evaluated inside or at the end of the body-force region. This can be seen in Figure 3.15(a) where the normalized velocity profiles reveal a wall-normal distance of $\delta_{1/2} = 0.3$ to 0.35 at the position of the maximum induced velocity.

This is significantly smaller than the expected values for a laminar wall-jet. Comparison with the non-dimensional wall-jet profiles, at a position 2.5mm downstream of the maximum velocity, reveal some differences. The wall-jet profiles are developed without the influence of the body force and the wall-jet starts to lift away from the surface. This can also be seen in Figure 3.12. Figure 3.15(b) reveals a larger wall-normal position of the velocity maximum of $\delta_{1/2} = 0.5$. This clearly demonstrates that the non-dimensional position of wall-jet maximum, when evaluated inside the body-force region, is not an reliable indicator of the turbulent or laminar state of the wall jet.

3.4 Force-Field Distribution

In this section the magnitude and the distribution of the force is analyzed, based on the velocity distribution of the standard actuator. First the force-field distribution and the limitations of the force field estimation is analyzed. This is followed by an analysis of the field magnitude compared to the direct thrust measurements.

Force-Field Distribution Figure 3.16 shows the calculated force-field distribution for an applied voltage of $V = 7$kV. The black line in Figure

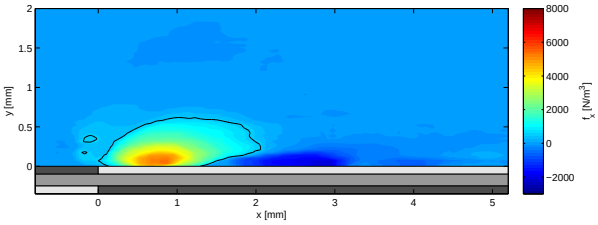

Figure 3.16: Force-field distribution at $V = 7$kV.

3.16 indicates the iso-contour line of 10% of the maximum induced force ($f_x|_{0.1 \cdot f_{x,max}}$) and serves as an indicator for the force-field dimension. The estimated force distribution spreads up to $y = 0.5$mm in wall-normal direction and is elongated along the surface, reaching the expected extent

($\Delta x_F = 2\text{mm}$) of the force field. Further downstream a region with a negative force can be seen in Figure 3.16.

This negative force component is presumably not associated with the discharge since its location exceeds the extent of the discharge. Also a remnant in the time averaged force-field estimation related to the force contributions during the positive and negative discharge half-cycle is questionable, since Wilke [163] demonstrated that the maximum force-field extent during the positive and negative half-cycles do not differ. The origin of the negative force term has to be investigated more in detail.

An explanation for this force component can be drawn from the analysis of the contribution of each term in Equation (2.13). The first term on the right hand side of this equation resembles the convection term in the NS equation and the second term gives the contribution of the diffusion.

$$f_x - \frac{\partial p}{\partial x} = \underbrace{\rho\left(u\frac{\partial u}{\partial x} + v\frac{\partial u}{\partial y}\right)}_{\substack{Convection\ term,\\ f_{x,\mathrm{Conv}}}} - \underbrace{\eta\left(\frac{\partial^2 u}{\partial x^2} + \frac{\partial^2 u}{\partial y^2}\right)}_{\substack{Diffusion\ term,\\ f_{x,\mathrm{Diff}}}}$$

In Figure 3.17 the distributions of the convection term and the diffusion term are shown. The iso-contour line of the total force is shown to give an orientation of the local contributions of the convection and the diffusion term. The relative share of the total force is given by 77% of the convection term and 23% is contributed with the diffusion term.

The convection term (shown in Figure 3.17(a)) dominates because of the acceleration of the fluid. The positive component of the convection is distributed inside the iso-contour line of the total force. Further downstream a negative region appears, indicating a deceleration of the fluid. In contrast to this, the major contribution of the diffusion term occurs close to the surface and spreads over a long distance in streamwise direction (shown in Figure 3.17(b), with a different colormap). The diffusion term is dominated by the second derivative of the u velocity component. Thus an exact determination of the velocity gradient and curvature close to the wall is essential to estimate the correct distribution and magnitude of the diffusion term. Dependent on the size of the IA and due to strong velocity gradients and the decreasing particle density in the near-wall region, the particle shift close to the wall is biased, as described by Kähler *et al.* [74].

These effects could lead to a falsely determined curvature of the velocity

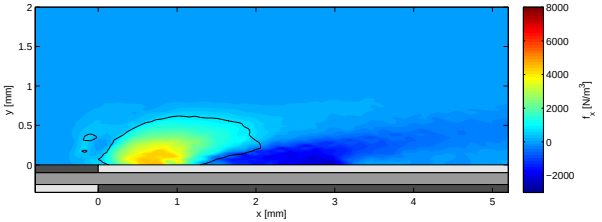

(a) $f_{x,\mathrm{Conv}} = \rho \left(u \frac{\partial u}{\partial x} + v \frac{\partial u}{\partial y} \right)$

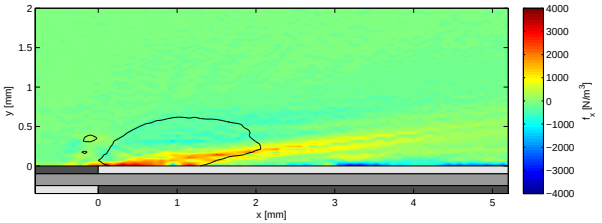

(b) $f_{x,\mathrm{Diff}} = -\eta \left(\frac{\partial^2 u}{\partial x^2} + \frac{\partial^2 u}{\partial y^2} \right)$

Figure 3.17: Distribution of the convection and diffusion term at $V = 7\mathrm{kV}$.

profiles in the near-wall region and this could cause an incorrectly estimated force.

To support this assumption a comparison with a second set of data, measured with the same actuator with an applied voltage $V = 7\mathrm{kV}$ emphasizes the necessity of correctly measuring the near-wall region of the wall-jet. The measurements above are further on referred to as measurements $M1$, whereas the second set of data is labeled $M2$. By comparing the wall-jet velocity profiles for the measurements $M1$ and $M2$ (in Figure 3.18) at the location 2.5mm downstream of the upper electrode (corresponding to the position of the negative force in Figure 3.16) good agreement can be seen for the maximum induced velocity and the general slope of the wall jet further away from the wall.

Below the wall jet's maximum a straight slope towards the wall and also a negative curvature, for both measurements $M1$ and $M2$, can be identified. This indicates an overestimated velocity close to the wall, with a falsely

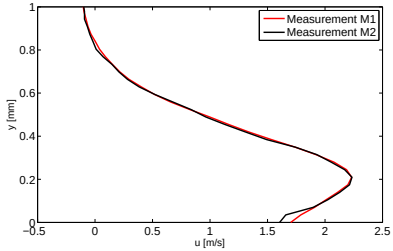

Figure 3.18: Comparison of the wall jets at $x = 2.5$mm for measurement $M1$ and $M2$.

determined curvature of the velocity profiles in both measurements. The force-field distribution for the second measurement is shown in Figure 3.19. For $M2$ a region with a negative force can be seen as well. The extent of the negative force is restricted to a smaller region, as compared to the force field distribution for the measurement $M1$ shown in Figure 3.16, but exhibiting a larger magnitude.

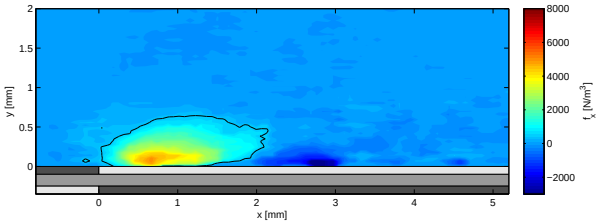

Figure 3.19: Force-field distribution for the second measurement $M2$ at $V = 7$kV .

These differences can be explained by the contribution of the convection and the diffusion terms to the force f_x. The convective term for the measurement $M2$, shown in Figure 3.20(a), compares well the convective term for $M1$ (cp. Figure 3.17(a)) in extent and magnitude. Thus, the difference in the force field distribution is not related to the convective term. A difference between the measurement $M1$ and $M2$ can be recognized in the diffusion term (Figure 3.17(b) and Figure 3.20(b) respectively). For $M2$ the magnitude of the diffusion term is larger, whereas the extent of

the positive component is comparable with the measurement $M1$. Thus, the negative component from the convection term is more strongly compensated for measurement $M2$. Except for a small region close to the wall (at $x \approx 2.8$mm), strong negative values in the diffusion term are present for the measurement $M2$, due to the deviated wall-jet profile. Thus it can be concluded, that the source of the negative force can be found in the underestimation of the diffusion term.

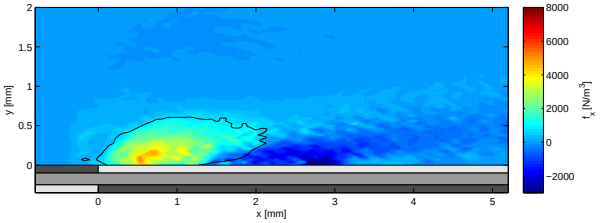

(a) $f_{x,\mathrm{Conv}} = \rho \left(u \frac{\partial u}{\partial x} + v \frac{\partial u}{\partial y} \right)$

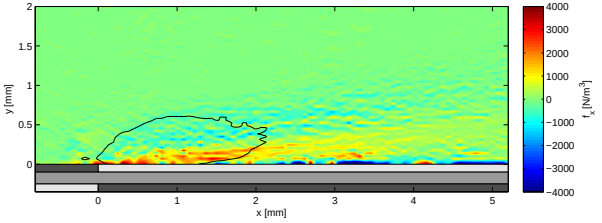

(b) $f_{x,\mathrm{Diff}} = -\eta \left(\frac{\partial^2 u}{\partial x^2} + \frac{\partial^2 u}{\partial y^2} \right)$

Figure 3.20: Distribution of the convection and diffusion term for the measurement $M2$ at $V = 7$kV.

By adding zero-velocity at the wall as shown in Figure 3.21, it can be shown that the curvature of the profiles is not entirely corrected, but avoids values of the curvature with a negative sign.

Results of the force field estimation with the corrected velocity at the wall for the measurements $M1$ and $M2$ are shown in Figure 3.22. The negative contribution of the convection term to the force is almost entirely compensated by the diffusion term with the modified velocity profiles.

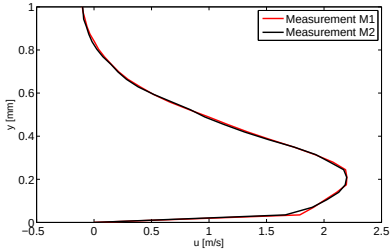

Figure 3.21: Comparison of the corrected wall jets at $x = 2.5$mm for measurement $M1$ and $M2$.

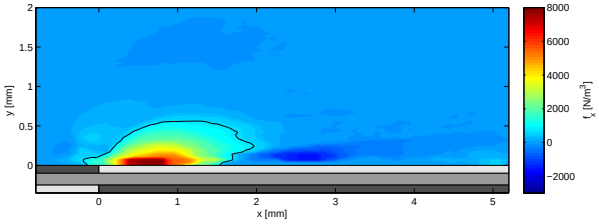

(a) Measurement $M1$

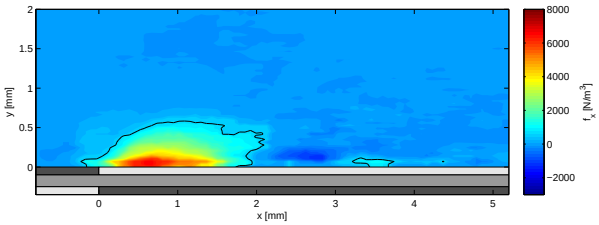

(b) Measurement $M2$

Figure 3.22: Comparison of the force-field distribution with the corrected velocity fields for measurement 1+2.

This indicates that the region of the negative force is not related to the discharge or induced by the body force of the actuator itself. It is much more related to the experimental limitation for the estimation of velocities

with strong gradients close to the wall. Thus the negative force component is neglected in the determination of the force magnitude.

In addition to the force field distribution, the force-field extent and its magnitude can be derived with the indirect force measurements. As defined earlier and demonstrated by Kriegseis *et al.* [87], the contour lines of 10% of the maximum induced body force serve as an indicator of the force-field extent.

The contour lines for different applied voltages are shown in Figure 3.23. There, the position of each maximum induced force is marked with an x. The position of the maximum induced force is increasingly shifted away from the edge of the upper electrode with increasing voltage. The relative position of the maximum force is around $0.25 - 0.3 \cdot \Delta x_F$, compared to the force-field extent.

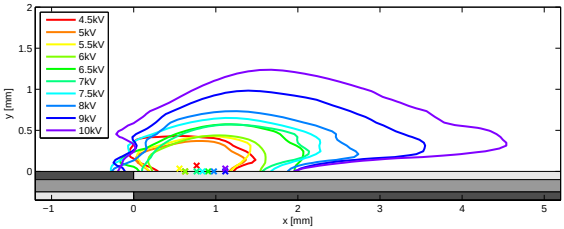

Figure 3.23: 10% isolines of the force distribution $f_x(x, y)$ for different applied voltages V ($f = 10$kHz).

With increasing applied voltages the extent of the force field (Δx_F) grows, as already demonstrated by Kriegseis *et al.* [87]. This is shown in Figure 3.24, where the downstream position of the maximum induced velocity is compared to the plasma extent as derived from gray value distributions (cp. Figure 3.14) expanded with the extent of the force field Δx_F.

Force Magnitude The force magnitude is determined by integrating the force distribution as shown in Equation (3.3).

$$F_i/L = \int_{y_{\min}}^{y_{\max}} \int_{x_{\min}}^{x_{\max}} f_i(x, y)\, \mathrm{d}x\mathrm{d}y. \tag{3.3}$$

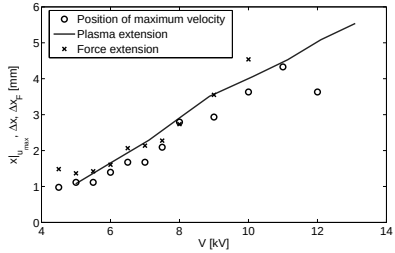

Figure 3.24: Downstream position of the maximum induced velocity in comparison to the plasma extent derived from gray value distributions and the extent of the force field Δx_F.

In Figure 3.25 the x-component of the force magnitude F_x is plotted as a function of the applied voltage. The red curve is plotted with a dependency of $F_x \propto V^{3\frac{7}{8}}$. This dependency is slightly higher as compared than the findings of Valerioti *et al.* [151] who identified a dependency of $V^{7/2}$ for different plasma actuators. This discrepancy in the dependency of the produced force with the applied voltage is discussed alongside with the comparison of the different force measurements.

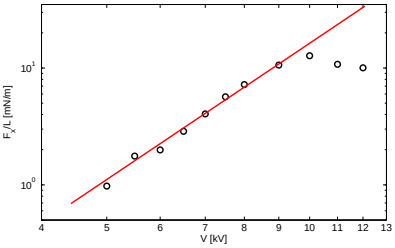

Figure 3.25: Force field magnitude F_x in dependency of the applied voltage.

The produced thrust F_t should not be understood as the produced body force F_b, because it is furthermore reduced by the wall-friction force term.

By comparing the direct thrust measurements with the differential and integral approaches, calculated with Equation (2.13) and Equation (2.9) respectively, the different outcomes of the thrust/force-voltage relation can be explained.

For this comparison, the different terms that contribute to the thrust are analyzed at the three sides of the control volume (integral thrust) and are compared to the direct thrust measurements. For the total force (integral force), all sides of the control volume are considered and compared to the force magnitude of the differential approach.

In Figure 3.26 the different approaches for the force estimation are shown in a logarithmic scale. The dissimilar relations for the direct thrust measurements (+) and the force magnitude of the differential approach (∘) can be seen in the different slopes in this diagram. The integral force estimation is shown with solid lines in red and blue, for integral thrust and the total integral force respectively. With the integral thrust and integral

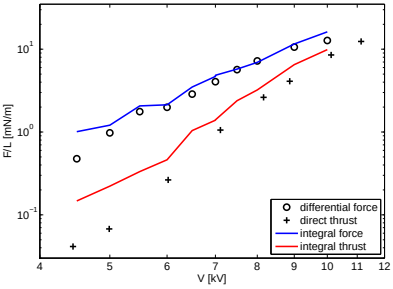

Figure 3.26: Comparison of the induced plasma forces estimated with different approaches.

force, similar relations can be seen as for measurements of thrust and force magnitude. For the integral force a similar relation of $F_x \propto V^{7/2}$ can be seen, agreeing well with the findings of Valerioti[151]. A slightly different slope in Figure 3.26 can be seen in the comparison of the integral force to the differential approach, resulting from underrated force magnitudes in the lower voltage range. This discrepancy can also be related to resolution of the near-wall regions of the velocity fields. This shows, that the estimated force magnitude with the indirect force measurements should be cross-checked with both approaches, the integral and differential approach, to assure the reliability of the results.

Both, the direct measured and integral thrust reveal a much steeper slope in the diagram. This indicates, that the relative share of the wall friction term to the total force is more pronounced at smaller applied voltages and smaller induced forces. The different relations of the applied voltage to the

induced force and thrust are therefore consistent.

3.5 Temporal Evolution of the Velocity Field

Based on PIV measurements in double frame mode the phase-averaged velocity distributions are calculated for an actuator operated at a voltage of $V = 7$kV and an operating frequency of $f = 10$kHz. In different experiments the discharge cycle was divided into 5 and 10 bins per cycle, according to the time between the laser pulses of $\Delta t = 20\mu s$ and $\Delta t = 10\mu s$ respectively. The maximum velocities of the phase-averaged velocity fields $u_\phi(x, y)$ over the phase angle of the discharge cycle are shown in Figure 3.27. Two measurements are shown for the 10 bin case and one measurement is shown for the 5 bin case. The different measurements yield similar temporal evolutions (in amplitude and phase) of the maximum induced velocity, revealing some fluctuations of the velocity data between the single measurements. It should be noted at this point, that each phase position in Figure 3.27 represents an independent experiment. In-between each measurement the actuator was turned off and was cleaned to remove depositions from the upper electrode. To assure comparable results, the actuator operating conditions, such as applied voltage and consumed power, were monitored and controlled with less than 1% deviation between the single measurements.

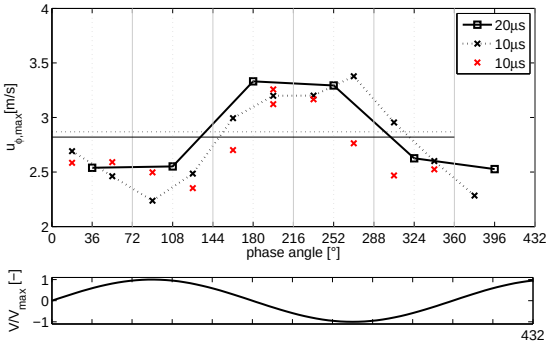

Figure 3.27: Time evolution of the maximum induced velocity in the flow field of an actuator operated at $V = 7$kV and $f = 10$kHz with different temporal resolution.

The mean values of the maximum velocity $\overline{u_{\phi,\max}}$ is shown for the $\Delta t =$

$20\mu s$ and $10\mu s$ cases in Figure 3.27 as horizontal lines. Both values are in good agreement with each other, but exceed the maximum velocity of time-averaged PIV measurements acquired in the single-frame mode as presented Section 3.3. This is due to the fact that the horizontal position of the maximum induced velocity varies during the discharge cycle, as shown in Figure 3.28. During the strong acceleration with the $\Delta t = 20\mu s$ measurement, the position of the maximum induced velocity moves closer to the upper electrode.

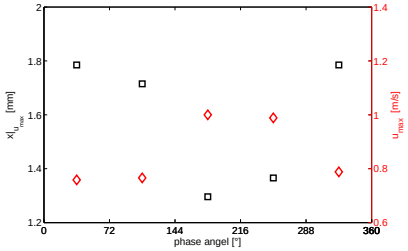

Figure 3.28: Variation of the horizontal position of the maximum induced velocity in comparison with the maximum induced velocity during the discharge cycle.

The average of the velocity field of the $\overline{u_\phi(x,y)}$ over the discharge cycle reveals a similar distribution compared to the time-averaged PIV measurements as presented Section 3.3. This can be seen in the comparison of velocity profiles at the position of maximum induced velocity for the mean velocity fields of the phase averaged measurements $\overline{u_\phi(x,y)}$ and of the time averaged velocity measurements in Figure 3.29.

The force-density distribution, based on Equation (2.13) and the averaged velocity field $\overline{u_\phi(x,y)}$, are calculated. The mean force of the discharge cycle is in good agreement with the estimated force as presented in Section 3.4, the difference in the force magnitudes is around 0.5%. Thus the comparability of the phase-averaged and the time-averaged measurements is assured.

The results of the normalized time evolutions of the maximum induced velocity are compared to data of Debien *et al.* [25] in Figure 3.30.

The velocity $u_{\phi,\max}$ is normalized with its maximum value within the discharge cycle. Even though the operating conditions and the actuator setup used in Debien *et al.* [25] differ considerably, a similar time evolution

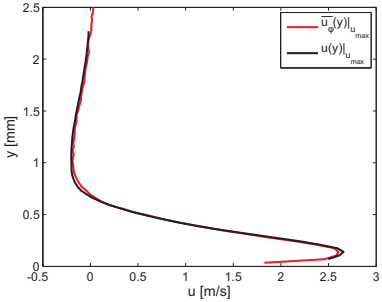

Figure 3.29: Velocity profiles at the position of maximum induced velocity for phase averaged measurements $\overline{u_\phi(x,y)}$ and the time averaged velocity measurements $(u(x,y))$.

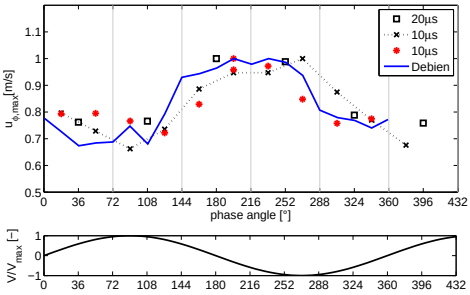

Figure 3.30: Time evolution of the maximum induced velocity in the flow field of an actuator operated at $V = 7$kV and $f = 10$kHz with different temporal resolution in comparison with data of Debien *et al.* [25].

can be seen.
The velocity fluctuation during a discharge cycle is restricted to the region of the discharge. This can be seen in Figure 3.31, where the velocity profiles $u_\phi(y)$ for the different phase positions at two downstream positions are shown. At $x = 1$mm downstream of the upper electrode in the middle of the discharge region ($V = 7$kV) a strong fluctuation of the velocity profile can be observed. Only 2mm farther downstream, outside of the discharge region, at $x = 3$mm, no difference between the different phase angles can

be recognized in the velocity profiles.

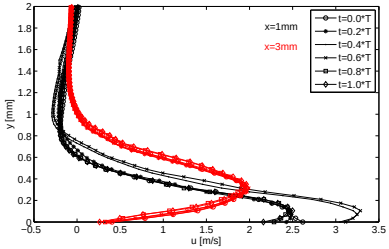

Figure 3.31: Temporal evolution of the velocity profiles at $x = 1$mm and $x = 3$mm for $V = 7$kV and $f = 10$kHz.

To derive the force field evolution at different instants of a discharge cycle the time-dependent term $\rho\frac{\partial u_i}{\partial t}$ has to be considered in the calculation, as shown in Equation (3.4) and (3.5).

$$f_x(x,y,t) = \rho\frac{\partial u}{\partial t} + \rho\left(u\frac{\partial u}{\partial x} + v\frac{\partial u}{\partial y}\right) - \eta\left(\frac{\partial^2 u}{\partial x^2} + \frac{\partial^2 u}{\partial y^2}\right) \quad (3.4)$$

$$f_y(x,y,t) = \rho\frac{\partial v}{\partial t} + \rho\left(u\frac{\partial v}{\partial x} + v\frac{\partial v}{\partial y}\right) - \eta\left(\frac{\partial^2 v}{\partial x^2} + \frac{\partial^2 v}{\partial y^2}\right) \quad (3.5)$$

With the strong acceleration and deceleration of the flow during a discharge cycle as shown in Figure 3.27, the force is dominated by the time-dependent term. Beside this strong effect of the acceleration and deceleration on the temporal evolution of the force, small fluctuations in the velocity field results in a large change in the transient term $\rho\frac{\partial u_i}{\partial t}$. A velocity change of only $\Delta u = 0.1$m/s between two measurements changes the body force by $6020N/m^3$ at this position due to the very short $\Delta t = 10\mu s$ between two PIV raw images. Since the velocity fields of all phase angles are measured in single experiment extreme accuracy is required.

To reduce the error in the estimation of the temporal force-field evolution, the phase-averaged measurements with the coarser temporal resolution (5 bins) are used. The force-density distributions for the different phase angles are shown in Figure 3.32. The negative half-cycle starts with a strong acceleration of the flow at the second phase angle. The extent of the body-force increases until the third phase angle at $\phi = 180°$, followed by a short period of deceleration with the phase positions $\phi = 252°$ and $324°$. The

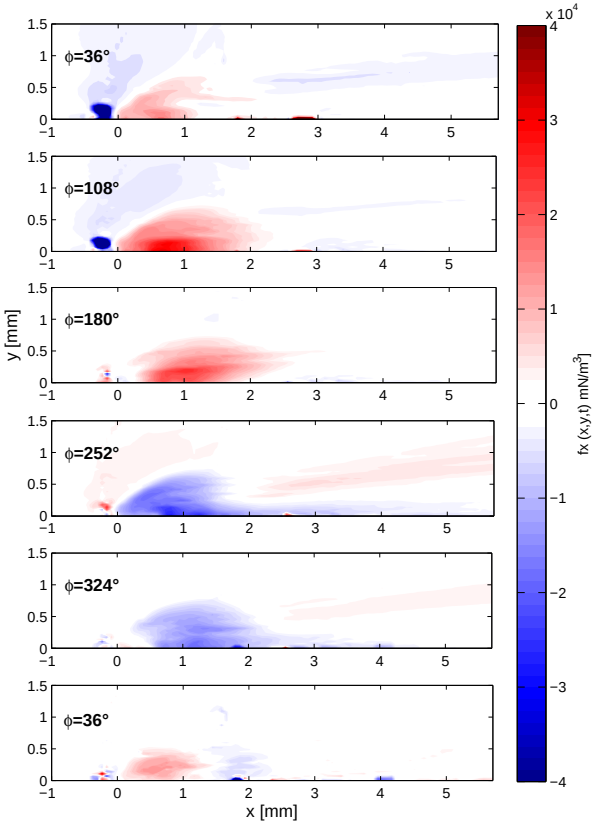

Figure 3.32: Time evolution of the force field distribution.

last force-density distribution indicates the beginning of the next discharge cycle, starting again with a small acceleration of the flow.

On top of the upper electrode $x < 0$mm small regions with a large body-force amplitude can be seen in Figure 3.32 for the first two phase angles. These areas are presumably the results of the velocity fluctuation due the accuracy of different experiments and are not induced by the EHD force of the discharge. Outside of the discharge region, areas with a positive or

negative body-force are present. This can be compared to the first and the last force-density distribution shown in Figure 3.32. These force-density distributions resemble the same phase angle of the discharge cycle and significant differences can be seen. In the last force-density distribution the spatial extent of the positive body force is smaller and closer to the upper electrode. No negative component of the body force can be seen in the field. Nevertheless, the phase-averaged force-field distribution provides insight into the force production and its distribution during the discharge cycle.

To reduce the uncertainty of the estimation of the force magnitude, the area for the force integration is reduced to only enclose the spatial extent of the discharge ($0 < x < 2.2$mm and $0 < y < 1.5$mm). The time-averaged force magnitude, derived from the phase-locked averaged measurements, only exceeds the force magnitude based on the time-averaged measurements by 7.3%. This shows a good agreement between both measurement approaches.

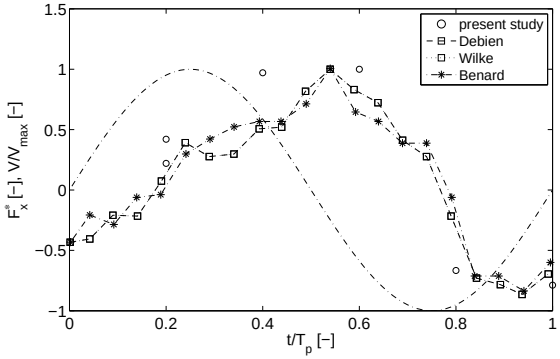

Figure 3.33: Time evolution of the force magnitude by comparison with previous literature (Debien *et al.* [25], Wilke [163] and Benard *et al.* [10]).

The force magnitude for each phase angle is shown in Figure 3.33 in comparison with results from Wilke [163], Bernard *et al.* [10] and Debien *et al.* [25]. The amplitude of the body force is normalized (divided by its maximum value) for better comparison between very different plasma actuators: different dielectric thicknesses, applied voltages and operating frequencies. All results show that the horizontal force magnitude F_x is

positive during the negative going-cycle and negative during the positive going-cycle. No significant differences can be distinguished in the temporal evolution of the force during a discharge cycle, even though the actuator in the present work was operated at a significantly higher frequency and with a thinner dielectric, resulting in a smaller force field extent.

3.6 Summary of the Characterization of DBD Plasma Actuators

In this chapter the operation limits of the plasma actuator, as used in this work was, were defined. The operation range with the upper and lower limit is determined with a spatially and temporally homogeneous discharge region. This was defined with the analysis of the voltage-power characteristics and optical measurements of the discharge light emission.

The induced velocity fields of the actuator operated in quiescent air were analyzed. The non-dimensional wall-jets showed good conformity at different applied voltages, when a length scale related to the discharge region, is taken into account. The non-dimensional wall-jets yield a form characteristic of laminar wall-jets, when the velocity profiles are examined downstream of the force field.

Different approaches to estimate the produced force with direct and indirect force measurements are compared. The evolution of the force in dependency of the applied voltage and consumed power exhibit a good agreement with the different approaches and in comparison with dependencies found in the literature. Time resolved velocity field measurements and force field distributions derived from this, demonstrated that the discharge characteristics during the discharge cycle is comparable with DBD plasma actuators with a significantly different setup and operating conditions.

4 Scaling Laws for the Induced Body Force

There are two options for directly or indirectly influencing the induced body force in its magnitude and distribution.

The direct influence is related to the change of the discharge intensity by changing the operating conditions and the actuator setup. With the operating conditions (operating frequency (f) and applied voltage (V)), the electric field strength is influenced and the actuator force magnitude and its distribution are affected. The actuator setup, such as changes in the thickness of the dielectric layer or its dielectric constant, the electric field density and thus the discharge intensity and distribution are influenced. The force magnitude and distribution are coupled and are dependent on the operating conditions and for a given actuator setup.

The indirect scaling of the induced body force is achieved with a discontinuous operation of the actuator. With the pulsed mode the actuator is repeatedly turned on and off. Usually this pulsed mode is used to excite or actively damp disturbances in the flow; however operated at a sufficiently high modulation frequency, the time averaged force production is also reduced. Since the discharge during the on-pulse of the modulation period is not affected, the discontinuous operation of the actuator is referred to as indirect scaling of the time averaged force.

4.1 Direct Scaling of the Induced Force

In the following section, the actuator setup is described and the influence of changes in the operating condition and the actuator setup are discussed separately. Kriegseis *et al.* [83] demonstrated that the simultaneous and independent measurements of the produced thrust, electrical characteristics and light emission cover the main required quantities to evaluate the actuator performance. Consequently, these three measurements are used to analyze the actuator performance in the dependencies of the influencing parameters.

The parametrical studies of the actuator performance are numerous. Only a small overview will be given here, beneficial for the following discussions about changes in operating conditions and actuator setup.

The first group of parameters discussed is the operating conditions. The voltage-power characteristic was identified by Enloe *et al.* [33] who demonstrated a dependency of $P_A \propto V^{7/2}$. Porter *et al.* [121] showed the influence of the frequency on the power consumption which proved to be linear $P_A \propto f$. This dependency is confirmed by several research groups (e.g.[1, 8, 26, 40, 116, 119]), also describing the power-frequency function as a linear. In [119], Porter *et al.* discussed the dependencies of the body force and the effectiveness with varying frequency and constant voltage or constant power. The effectiveness describes the ratio of the consumed power of the actuator and the produced thrust. Thrust measurements with varying frequencies were also performed by Poon *et al.* [118], Ferry *et al.* [35], Van Dyken *et al.* [152], and Thomas *et al.* [147]. A dependency of the produced thrust with the plasma extent was described as linear by Durscher *et al.* [28], Poon *et al.* [118], and Kriegseis *et al.* [83]. Roth *et al.* [130] investigated the influence of changes in operating condition and of different dielectric materials regarding power losses due to dielectric heating compared to the produced thrust, as a measure of the actuator performance.

The second group of parameters in this work addresses the actuator setup, as with the actuator setup a large variety in geometrical parameters is available. To clearly separate between the influences of the different parameters only changes in the dielectric material and thickness are considered herein. Further geometrical parameters such as electrode thickness, size, geometry and electrode arrangement, acting on the actuators performance, are not discussed in this work, but a number of publications on the topic are available and further information can be found in [1, 2, 117].

Influences from dielectric material and thickness were investigated by Thomas *et al.* [147], Poon *et al.* [118], Durscher *et al.* [27] and Van Dyken *et al.* [152]. There, the influence of different materials and thicknesses on the actuator performance was identified and described qualitatively. A decreasing thickness of the dielectric layer and an increase in dielectric constant both result in larger power consumption. A force increase with increasing thickness for a given power consumption was observed, resulting in an increase in effectiveness with thicker dielectrics. The effect of a lower dielectric constant was described with a lower power consumption and smaller induced force, but no precise description on the influence of

the effectiveness has been made.

4.1.1 Actuator Setup

The plasma actuator was mounted on an acrylic glass plate as sketched in Figure 2.10. The dimensions of the upper and lower electrodes are kept constant for all measurements, whereas the dielectric thicknesses as well as the dielectric materials were varied. The electrodes of all actuators are made of self-adhesive copper tape with a thickness of $d_e = 35\mu$m and a width of $w_1 = 2$mm and $w_2 = 10$mm for the upper and lower electrode respectively. An overview of the different actuator configurations is given in Table 4.1. The actuators $D1 - D4$ are composed of several layers of self-adhesive polyimide tape with different thicknesses of the polyimide layer ($d_p = 0.025$mm, 0.051mm and 0.127mm corresponding to 1mil, 2mil and 5mil). The thickness of the silicone adhesive is $d_s = 0.0381$mm for each layer. The total thickness of the dielectric layer is composed of the thickness of the polyimide layer and the thickness of the adhesive ($d = d_p + d_s$).

Label	d	ϵ	Material	Dielectric	Parameter
D1	0.317	3.04	Kapton	5x1mil	f, V
D2	0.279	3.07	Kapton	2mil+3x1mil	V
D3	0.241	3.12	Kapton	2x2mil+1mil	V
D4	0.165	3.26	Kapton	1x5mil	V
D5	0.38	10	Al_2O_3	-	V

Table 4.1: Overview of investigated actuator configurations

The total thickness of the polyimide layer was keep constant at $d_p = 0.127$mm (5mil) for the actuators $D1 - D4$ by varying different tapes, whereas the total thickness of the dielectric changed. The dielectric constant ϵ in Table 4.1 is calculated using the relative share of the total thickness of the silicone adhesive and polyimide, with a dielectric constant of $\epsilon = 2.8$ and $\epsilon = 3.4$ [1] respectively. The $D5$ actuator is made of an alumina plate with a dielectric constant $\epsilon = 10$.

In the following two sections, the influence of the plasma operating conditions and actuator setup on the three measures: thrust, electrical characteristics and light emission are discussed as well as their dependencies.

[1] http://www2.dupont.com

In Section 4.1.2 the influence of the plasma operation is discussed using actuator $D1$ at different operating frequencies and voltages. In the following Section (4.1.3), all actuators $D1 - D5$ are used at a fixed operating frequency to compare the influence of the actuator setup.

4.1.2 Influence of Plasma Operation

For the investigation of the dependencies and the characteristics of plasma operation and force production, the actuator $D1$ was operated at different frequencies ($f = 8,\ 10,\ 11,\ 12$ and 14kHz) with varying voltages. In the next three paragraphs the influence of plasma operation on the electrical characteristics, produced thrust and the light emission analysis will be discussed.

Electrical Characteristics The voltage-power characteristic is known to follow the dependencies of the voltage with the power law $P_A \propto V^{7/2}$. The operating frequency f influences the consumed power linearly, as mentioned above. Porter *et al.* [121] assumed the dissipated energy per discharge cycle to be constant. The consumed power is calculated with the dissipated energy per discharge cycle and the operating frequency, thus the consumed power increases linearly with operating frequency. Also, the power consumption is influenced linearly by the length L of the plasma actuator, as demonstrated by Kriegseis *et al.* [83]. All this leads to the following correlation:

$$\frac{P_A/L}{f \cdot V^{7/2}} = const. \tag{4.1}$$

The unscaled voltage-power diagram in Figure 4.1(a) and the voltage-power diagram scaled with the frequency f in Figure 4.1(b) reveal that this correlation is well met. The solid lines in Figure 4.1(a) are measurements of constant frequency. When the dependency of the frequency is taken into account in the scaled voltage-power diagram, all measurements collapse onto one line, as shown in Figure 4.1(b).

This corresponds to the assumption of Porter *et al.* [121] and indicates that the dissipated energy per discharge cycle is constant.

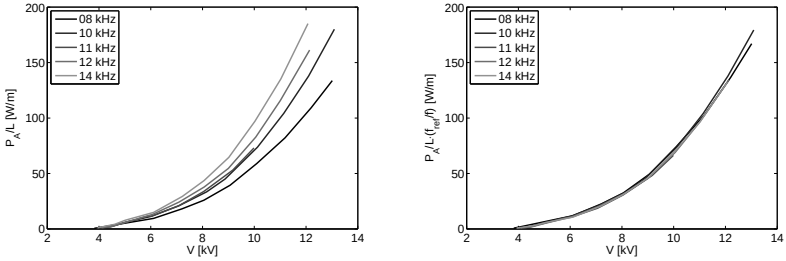

(a) unscaled (b) scaled

Figure 4.1: Unscaled and scaled voltage-power diagram for actuator $D1$ with varying voltages and frequencies.

Force Measurements The change of the produced thrust on the operating frequency and applied voltage was addressed in several publications (e.g. Van Dyken *et al.* [152], Enloe *et al.* [29], Thomas *et al.* [147], and Poon *et al.* [118]). The correlation between the power consumption and the produced thrust with varying frequency was qualitatively described, revealing a decrease in effectiveness with increasing frequency.

In this work the force, more specific the produced thrust of an actuator, is estimated with the direct thrust measurement as described in Section 2.2.3. To determine the the influence of the operation conditions on the thrust production, the produced thrust is analyzed with the dependencies of the electrical characteristics. Comparing the diagram F_t/L over P_A/L with varying frequency in Figure 4.2(a), the dependency of the produced thrust with the frequency clearly becomes obvious; with a constant power consumption a higher force is achieved with a lower frequency. The force power diagrams for the different measurements, shown in Figure 4.2, confirm that the effectiveness decreases with increasing frequency. While the consumed power is linearly coupled to the operating frequency (c.p. Equation (4.1)), the produced force does not exhibit the same dependence, which yield the change in effectiveness.

Curve fitting analysis of the experimental data reveals an empirical scaling law: The consumed power is proportional to the produced force and the frequency with the power of $-3/4$.

$$F_t \cdot f^{3/4} \propto P_A \tag{4.2}$$

This relation is shown in Figure 4.2(b), where the thrust per meter F_t/L

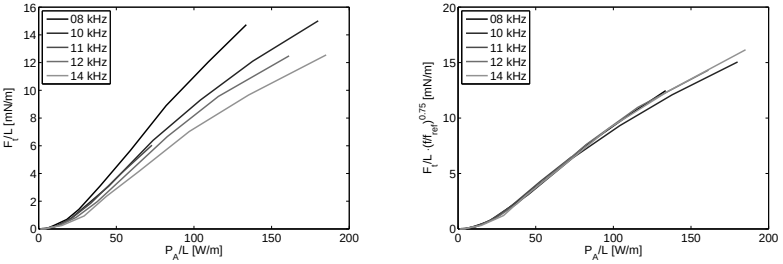

(a) unscaled (b) scaled

Figure 4.2: Unscaled and scaled power-thrust diagram for actuator $D1$ with varying voltages and frequencies

is plotted over the scaled power consumption $P_A/L \cdot \left(\frac{f_{ref}}{f}\right)^{3/4}$. The reference frequency $f_{ref} = 10\text{kHz}$ is chosen arbitrarily, to keep the scaling non-dimensional. All lines in the scaled thrust-power diagram collapse. The scaled thrust-power diagrams correspond to the reference frequency. A measurement at a constant voltage level ($V = 9\text{kV}$) with varying frequencies between $f = 7 - 17\text{kHz}$ is shown in Figure 4.3. The scaled and unscaled thrust-power diagrams are compared directly, also showing the standard deviation of the thrust measurement as error bars for both cases. The deviation shown with the error bars just represent the variation within the thrust measurements. Errors originating from changes in the actuators performance or a systematic errors with the thrust measurement are not taken into account in this consideration. The two outliers in the lower frequency range must have suffered from some unsteadiness in the plasma operation or a systematic error, since the standard deviation is small compared to the difference.

The curve is almost horizontal for the scaled thrust $F_t/L \cdot \left(\frac{f}{f_{ref}}\right)^{3/4}$.

The dependency of the voltage-thrust behavior with varying frequency is less pronounced than that of the power-thrust characteristics. Nevertheless, with increasing frequency the produced thrust is slightly enhanced with constant applied voltage, as Figure 4.4(a) clearly shows.

The relation of the produced force and the voltage can be described by:

$$F_t / \left(L \cdot f^{1/4}\right) \propto V^{7/2}, \tag{4.3}$$

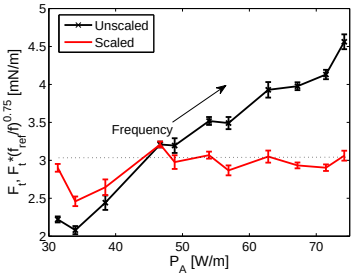

Figure 4.3: Unscaled and scaled power-thrust diagram for a constant applied voltage of $V = 9$kV and varying frequency

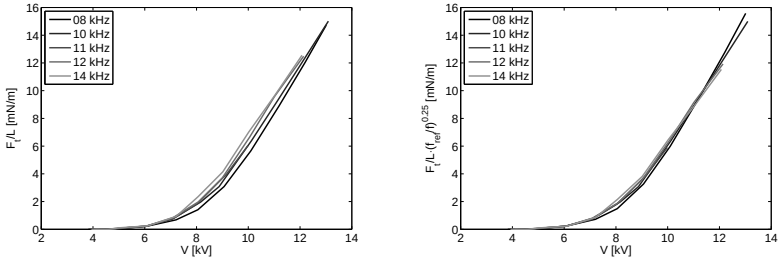

(a) unscaled (b) scaled

Figure 4.4: Unscaled and scaled voltage-thrust diagram for actuator $D1$ with varying voltages and frequencies

derived through the relation of the voltage-power characteristic $P_A/L \propto V^{7/2}$ and the relation in Eqn. 4.2. This relation is shown in Figure 4.4(b) with the scaled thrust of $F_t/L \cdot \left(\frac{f_{ref}}{f}\right)^{1/4}$. In the scaled diagram all measurements for different frequencies collapse to one line, representing the reference frequency f_{ref}. The effectiveness of the momentum transfer is reduced at higher operating frequencies.

To validate the correlation derived in this investigation, the scaling-laws are cross-checked using force measurements with varying frequency found in literature. Measurements by Poon *et al.* [118] and Thomas *et al.* [147] are shown in Figures 4.5(a) and 4.5(b) respectively. In the left part of each

figure, the unscaled thrust-power diagrams are shown. In comparison to this, the diagrams with the correlation from Equation (4.2) are shown in the right part of each figure.

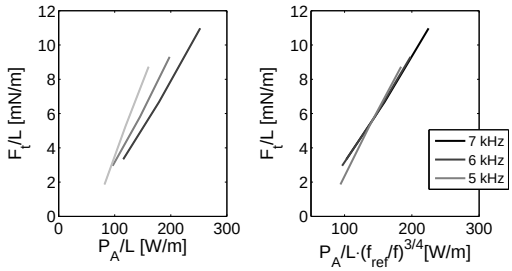

(a) Power-thrust diagram based on the data of Poon *et al.* [118] ($f_{ref} = 5$kHz)

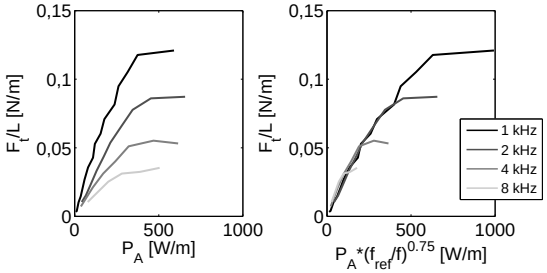

(b) Power-thrust diagram based on the data of Thomas *et al.* [147] ($f_{ref} = 2$kHz)

Figure 4.5: Unscaled and scaled power thrust diagrams, based on the data of Poon *et al.* [118] and Thomas *et al.* [147], with varying voltages and frequencies,

In the thrust-power diagram of Thomas *et al.* [147], a saturation of the produced thrust can be seen. Thomas *et al.* related the saturation to the onset of a filamentary discharge associated with a maximum achievable thrust and still increased power dissipation. Thomas *et al.* showed that the onset of the saturation is dependent on the operating frequency f. With the change in the slope of the thrust-power diagram in Figure 4.5(b), the onset of thrust saturation can be seen for higher power levels. A saturation of the wall jet to a maximum velocity was also reported by Boeuf *et al.* [14] and Moreau *et al.* [106].

All lines of the scaled thrust-power diagram and thrust-voltage diagram show a good agreement with the reference case with the scaled data, based on the empirical scaling laws in Equation (4.3) and Equation (4.2). These scaling laws yield robust and general dependencies before the saturation of the discharge starts.

Light Emission The determination of the light emission and the measurement of the gray-value distribution and plasma extension Δx provide additional and independently-measured parameters for the characterization of the actuator and its performance. The interrelation of the light emission with electrical characteristics are shown by Enloe *et al.* [32] and Orlov *et al.* [109], with a dependency of $V \propto \Delta x$.

Kriegseis *et al.* suggested the dependency $C_{eff} \propto \Delta x$ in [83] and also showed the interrelation of plasma extent Δx and the extent of the estimated force-field distribution in [87].

During the measurements at constant voltage with varying frequency the plasma extent remained constant $\Delta x \approx const$ as shown in Figure 4.6. This is in good agreement with the findings of Orlov *et al.* [109] who also demonstrated the plasma extent to be independent of the operating frequency. This can also be seen for the different measurements in Figure 4.7(a).

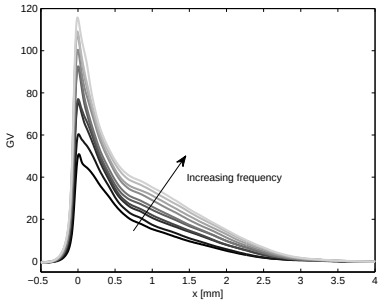

Figure 4.6: Gray-value distribution ($G(x)$) for a constant applied voltage of $V = 9$kV and varying frequency

For the given actuator setup and varying operating conditions, the correlation in Equation (4.4) of the consumed power and the integral gray value is shown in Figure 4.7(b). Independent of the operating frequency a close

correlation of the consumed power P_A and the light emission intensity GV, the integral of the gray value, can be found.

$$P_A/L \propto GV \tag{4.4}$$

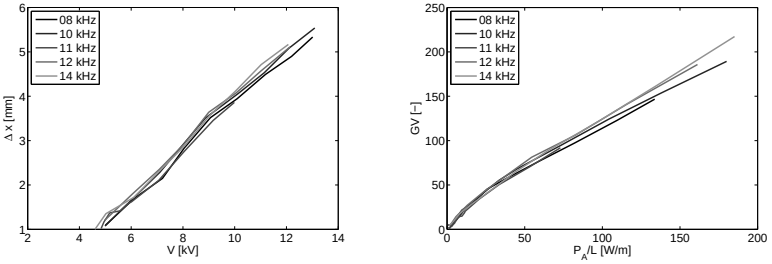

(a) Voltage-Δx diagram (b) Power-GV diagram

Figure 4.7: Interrelation of the applied voltage (V) and the plasma extent Δx (a) and the consumed power (P_A) and the integral gay-value (GV) for actuator $D1$ with varying voltages and frequencies

The thrust over the light emission intensity GV is shown in Figure 4.8(a), here a similarity to the thrust-power diagram in Figure 4.2(a) can be seen. This confirms the correlation given in Equation (4.4). With the linear correlation of P_A and GV, the interrelation of integral gray value and thrust can be written as $F \propto GV/f^{3/4}$ (shown in Figure 4.8(b)).

The correlation given in Equation (4.4) completes the interrelation triangle between the measures of the gray-value distribution, the electrical measurements and the force measurements. It demonstrates the robustness and the generality of equations (4.2) and (4.3) as a scaling law for describing the force dependency on the operating conditions of DBD plasma actuators. With an equivalent description of this dependency, derived with independent measurements of the gray value distribution as given in Equation (4.4).

The influence of the operating conditions on the thrust production can be described and quantified by the procedures and realtions discussed in this chapter. The correlations in the equations (4.2) and (4.3) were confirmed with data published by other research groups [118, 119, 147].

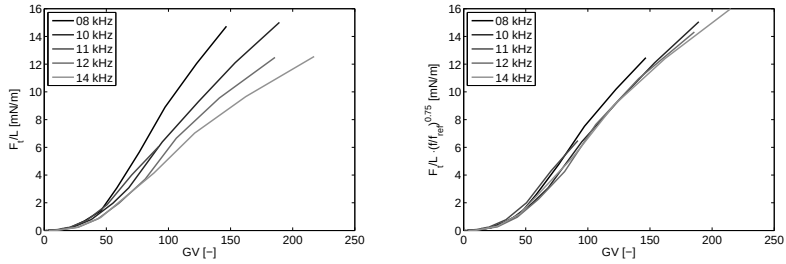

(a) unscaled (b) scaled

Figure 4.8: Unscaled and scaled power-integral gray-value diagram for actuator $D1$ with varying voltages and frequencies

4.1.3 Influence of the Actuator Setup

For the investigation of the force production in dependence of the actuator setup, the actuators $D1 - D5$ (see Table 4.1) were operated at a constant frequency ($f = 10$kHz) with varying voltages. With the change in dielectric material and thickness the actuator performance is influenced. This was described qualitatively by several researchers. Roth *et al.* [130] discussed the properties of different materials, e.g. dielectric constant, dielectric strength, loss factor, etc., concerning power losses due to the dielectric heating. Besides the actuator performance, the requirements on the material are manifold and often opposing each other with the different available materials. The influence of the degradation on the actuator performance in terms of electro erosion [56] on one hand makes the durability of the material important. On the other hand, flexibility and weight might be essential for some applications. The final choice for a certain material or setup often stems from a compromise between the different requirements and makes the choice of the optimal dielectric material and thickness crucial. The large variety of different materials and geometrical parameters makes it even more difficult to compare different experimental results, actuator performances or numerical with experimental results.

Alongside with the results in this section, the findings in literature about the influences of the actuator setup on the performance will be discussed. In the following paragraphs, the effect of actuator setup will be analyzed quantitatively, equivalent to the previous section, based on the electrical characteristics, produced thrust and the light emission measurements.

Electrical Characteristics Thomas *et al.* [147] described the effect of a lower dielectric constant as a reduction of the effective capacitance of the actuator and a subsequent reduction of the local concentration of electric field lines. According to them, the formation of filaments and, thus, the beginning of the saturation is influenced, since the decrease in the concentration of electric field lines is comparable to the effect of a lower current density. This is in good agreement with the description of the nonuniform/filamentary discharge by Roth *et al.* [130].

Durscher *et al.* [27] observed the same; higher voltages were sustainable for low dielectric constant compared to other materials of similar thickness, before a nonuniform/filamentary discharge starts.

The voltage-power diagram shown in Figure 4.9(a) reveals an increase in power consumption with a decreasing dielectric thickness d for the actuators $D1 - D4$ and a larger dielectric constant ϵ for the actuator $D5$. For both of the parameters, the influence is linear. This leads to the following correlation:

$$\frac{P_A/L}{V^{7/2}} \cdot \frac{d}{\epsilon} = const. \tag{4.5}$$

In Figure 4.9(b), the scaled voltage-power diagram is shown, related to a reference setup with the dielectric thickness of $d_{ref} = 0.3$mm and a dielectric constant of $\epsilon_{ref} = 3.4$. The voltage-power diagram in Figure 4.9(b) reveal some outliers for the actuators $D4$ and $D5$ at higher voltages and thus higher power consumption. A possible explanation for the outliers is the dielectric heating on the one hand. The change in temperature, for instance, influences the dielectric constant, which is a function of the temperature $\epsilon(T)$ and dependent on the material [149]. The change in the dielectric constant is more pronounced for the alumina dielectric (Al_2O_3) with the $D5$ actuator. On the other hand the degradation [56] of the polyimide dielectric influences the actuator characteristics. It was demonstrated ([56]) that the degradation is more pronounced with thinner dielectrics, as for example of the actuator $D4$. Both effects would yield a larger power consumption.

The power losses, such as the dielectric heating of the passive element are correlated with V^2 over the entire range of operation, while the linear correlation of the power consumption with d and ϵ in Equation (4.5) is connected with $V^{7/2}$. The overall power consumption scales with $P_A \propto V^{7/2}$,whereas

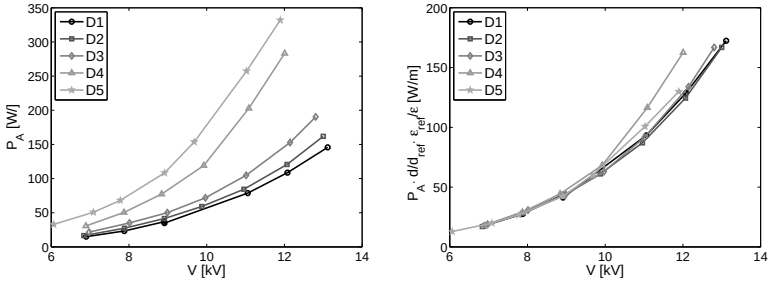

(a) unscaled (b) scaled

Figure 4.9: Unscaled and scaled voltage-power diagram for actuator $D1 - D5$

the passive power losses of the actuator, correlated with $P_L \propto V^2$. Accordingly the difference between P_A and P_L is the consumed power by the gas discharge, described by Roth *et al.* [130] as plasma maintenance power P_D. Thus the consumed power of the plasma actuator is composed of the power losses and the plasma maintenance power $P_A = P_L + P_D$. Consequently, the variation in the dielectric thickness and material does not solely influence the dielectric heating, but also the power consumption connected with the discharge.

Force Measurements Since the overall power consumption of the plasma actuator scales linearly with the thickness and dielectric constant of the dielectric, the discharge is influenced as well. The change and scaling of the induced thrust and the effectiveness of the different actuator setups is the arising question now.

The unscaled force-power diagram (Figure 4.10(a)) shows good agreement with the findings of Poon *et al.* [118], as an increase in thickness leads to an increase in effectiveness with the actuators $D4$ to $D1$. The effect of the dielectric thickness was described by Poon *et al.* [118] as an increase in effectiveness with thicker dielectrics. Van Dyken *et al.* [152] observed a force increase with increasing thickness for a given power consumption. Furthermore, the strong effect of the dielectric constant becomes obvious, which shows a decrease in effectiveness with an increase of the dielectric

constant with the actuator $D5$.

Curve fitting analysis of the experimental data reveals empirical scaling laws for the force in dependence of the dielectric constant and thickness either for the consumed power or the applied voltage. The correlation of the force with the dielectric constant and its thickness in dependence of the consumed power P_A or the applied voltage V can be described as followed:

$$F \propto P_A \cdot \frac{d^{1/2}}{\epsilon^{7/10}} \tag{4.6}$$

$$F \propto V^{7/2} \frac{\epsilon^{3/10}}{d^{1/2}} \tag{4.7}$$

The scaled force-power diagram (Figure 4.10(b)) is based on the correlation given in Equation (4.6) and is related to a reference setup with the dielectric thickness of $d_{ref} = 0.3$mm and a dielectric constant of $\epsilon_{ref} = 3.4$ (resembling the dielectric constant of Kapton). The lines in this scaled force-power diagram for the actuators $D1 - D5$ collapse and the influence of the dielectric thickness and the dielectric constant are compensated. Some outliers with the actuator $D4$ at higher consumed power can be seen (Figure 4.10(b)). The limitation in the produced thrust is due to the beginning of the saturation with the thinnest dielectric. This also shows that the scaling law is restricted to the homogeneous discharge region.

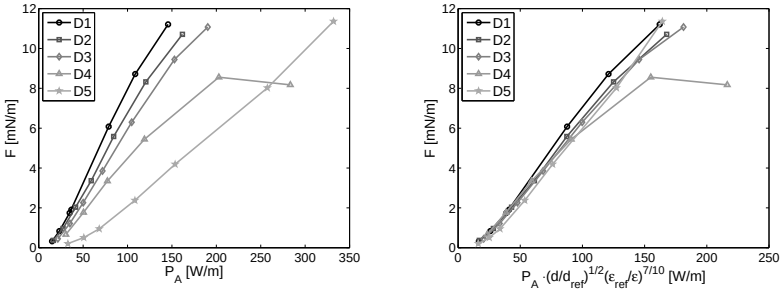

(a) unscaled (b) scaled

Figure 4.10: Unscaled and scaled power-thrust diagram for the actuators $D1 - D5$

In Figure 4.11(a), the force-voltage diagram is shown for the actuators $D1 - D5$. An increase of the produced thrust at constant applied voltages for thinner dielectrics or higher dielectric constants can be seen. The effect

of the changed dielectric is less pronounced as compared to the force-power diagram shown in Figure 4.10. The correlations in Equation (4.7) and Equation (4.6) are linked with the correlation given in Equation (4.5). By comparison of the unscaled scaled force-voltage diagram with the scaled force-voltage diagram, shown in Figure 4.11(b), it can be seen that the different measurements in the scaled force-voltage diagram agree well the the references case and the influence of the dielectric thickness and the dielectric constant are compensated. Again some outliers for actuator $D4$ at higher applied voltages can be seen, again related to the beginning of the saturation, but the overall agreement with this correlation is good. The influence of the dielectric thickness and the dielectric constant is compensated by the correlation in Equation (4.7).

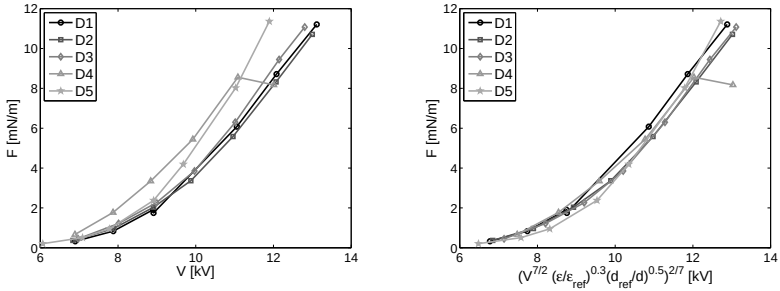

(a) unscaled (b) scaled

Figure 4.11: Unscaled and scaled voltage-thrust diagram for actuator $D1 - D5$

To validate the correlation in Equation (4.6) and Equation (4.7), the scaling laws are used to compensate the influence of the dielectric thickness and the dielectric constant in data found in the work of Poon *et al.* [118], Thomas *et al.* [147] and Van Dyken *et al.* [152]. Poon *et al.* [118] varied the thickness by using several layers of polyester film for the dielectric. In Figure 4.12(a), the scaled and unscaled force-power diagram is presented based on data found in [118]. A discrepancy can be found in the scaled force-power diagram with the thinnest dielectric. This could be caused by the dielectric heating, degradation of the dielectric, nonuniform/filamentary discharge or other influences, yet unknown. The scaled force-power diagram on the right side of Figure 4.12(a) is related to the reference thickness of $d_{ref} = 0.762$mm. All lines resemble this reference

case and show good overall agreement with the correlation (4.6).

A further study, varying the dielectric thickness by several layers of Kapton tape was carried out by Van Dyken *et al.* [152]. In Figure 4.12(b), the unscaled (left) and scaled (right) force-voltage diagram is shown. In both diagrams a clear start of saturation can be seen, as also described by Van Dyken *et al.* [152]. In the region of the homogeneous and filament free discharge, the lines collapse to the reference case of d_{ref} = 24mil, thus revealing a good agreement with the correlation in Equation (4.7). Again, the stronger influence of the change in the actuator setup can be seen in the force-power diagram, as shown in Figure 4.12(c), with the data derived from Van Dyken *et al.* [152]. The scaled force-power diagram (right side of Figure 4.12(c)) collapse to one line corresponding to the reference case of d_{ref} = 24mil based on the correlation in Equation (4.6).

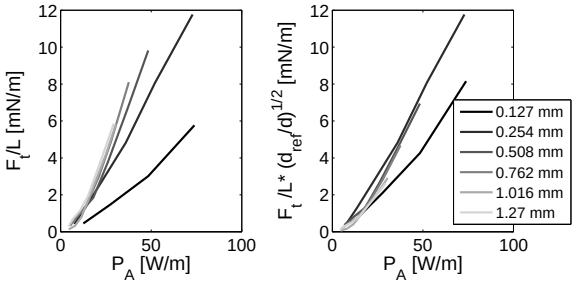

(a) Power-thrust diagram based on the data of Poon *et al.* [118](d_{ref} = 0.762mm, $\epsilon = const$)

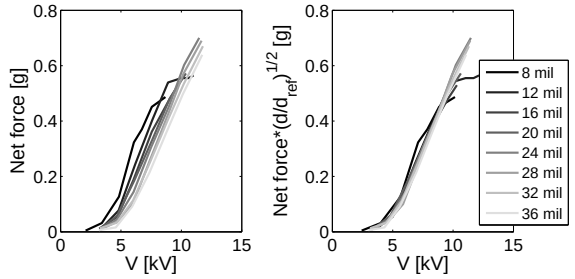

(b) Voltage-thrust diagram based on the data of Van Dyken *et al.* [152](d_{ref} = 24mil, $\epsilon = const$)

. . .
to be continued

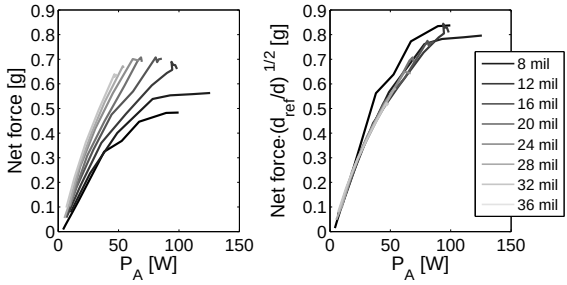

(c) Power-thrust diagram based on the data of Van Dyken *et al.* [152](d_{ref} = 24mil, $\epsilon = const$)

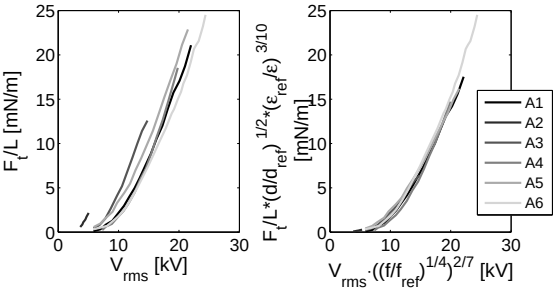

(d) Voltage-thrust diagram based on the data of Thomas *et al.* [147](reference case A6) A1: 6.35mm, Delrin, 2.3kHz; A2: 0.15mm, Kapton, 4.4kHz; A3: 3.18mm, Macor , 2.3kHz; A4: 6.35mm, Quartz, 2.3kHz; A5: 3.18mm, Teflon, 2.0kHz; A6: 6.35mm, Teflon, 2.1kHz

Figure 4.12: Unscaled and scaled power or voltage-thrust diagrams, based on the data of Poon *et al.* [118], Thomas *et al.* [147] and Porter *et al.* [119], with varying dielectric constants and thicknesses

A larger variety of parameters was carried out in the work of Thomas *et al.* [147], where the dielectric thickness d, the dielectric constant ϵ and the frequency f were varied. The scaled and unscaled force-voltage diagrams of the data from Thomas *et al.* [147] are shown in Figure 4.12(d). The reference case for the scaled force-voltage diagram is given with their actuator configuration A6, a 6.35mm thick Teflon dielectric operated at $f = 2.1$kHz. The dielectric thickness d was varied in the range of $d = 0.15 - 6.35$mm and the dielectric constant within $\epsilon = 2.0$ to 6.0 (see [147]). The force-voltage diagram in right part of Figure 4.13d shows a good agreement for the dif-

ferent actuator configurations and collapses to the force-voltage diagram of the reference case.

The correlations in Equation (4.6) and (4.7) are able to compensate the influence of the dielectric thickness and the dielectric constant with data found in the work of Poon *et al.* [118], Thomas *et al.* [147] and Van Dyken *et al.* [152]. This clearly shows, that the scaling is reasonable over a large range of different dielectric materials and thicknesses as long as the discharge is still in a homogeneous and non-filamentary regime.

Light Emission The plasma extent Δx exhibit a linear correlation with the applied voltage as mentioned above with the plasma operation for the different actuators, as shown in Figure 4.13(a).

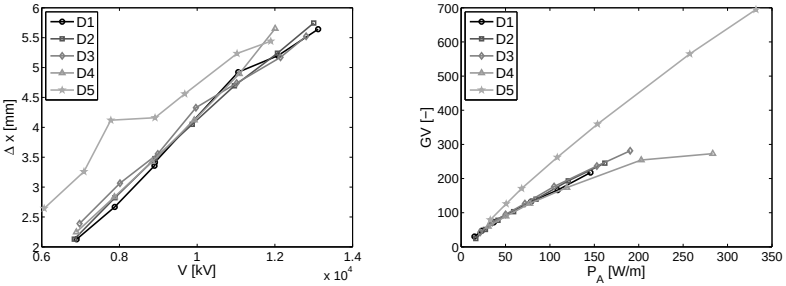

(a) Voltage Δxm

(b) power-gray value diagram

Figure 4.13: Interrelation of the applied voltage (V) and the plasma extent Δx (a) and the consumed power (P_A) and the integral gay-value (GV) for actuator $D1 - D5$

An influence of the dielectric thickness and constant on the plasma extent Δx is not very clear, especially with the influence of the dielectric thickness in the investigated range. Due to the different reflectivity of the dielectric material the luminosity of the discharge differs. With the white material of the alumina (Al_2O_3) dielectric of the actuator $D5$, the discharge appears brighter as compared to the darker dielectric surface with actuator $D1-D4$. An almost parallel shift for the actuator $D5$ in the diagram of the plasma extent over applied voltage can be seen in Figure 4.13(a). Whether this shift is due to the reflectivity of the dielectric surface or the influence of the dielectric constant, cannot be clearly distinguished. Thus a scaling will

not be attempted, also in respect to the measurement uncertainty.

The gray value-power diagram is shown in Figure 4.13(b). The differences for the actuators $D1 - D4$ in the power-gray value diagram are marginal, whereas the actuator $D5$ differs a lot. This might again be due to different reflectivity of the dielectric material. Regarding the actuators $D1 - D4$, the correlation in Equation (4.4) is valid. The slope of actuator $D5$ is also linear in Figure 4.13(b). This implies that the correlation in Equation (4.4) is valid for a certain type of dielectric material.

With the correlation in Equation 4.6, the interrelation of the integral gray value and the produced thrust of the actuator can be determined.

$$GV \propto F_t \frac{\epsilon^{7/10}}{d^{1/2}} \tag{4.8}$$

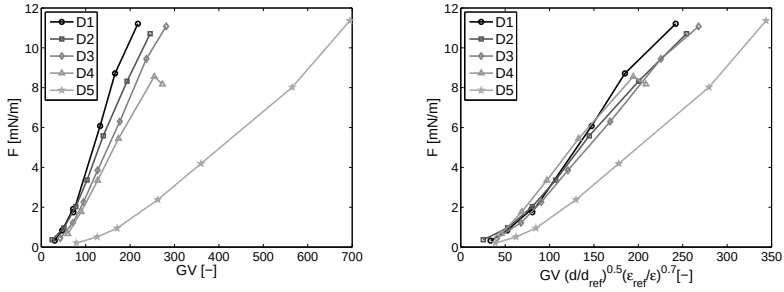

(a) unscaled (b) scaled

Figure 4.14: Unscaled and scaled power-integral gray-value diagram for actuator $D1 - D5$

The relation of the force and the integrated gray value GV (Equation 4.8) is compared to the unscaled diagram with the scaled diagram in Figure 4.14(a). With the unscaled force-integral gray value diagram, an influence of the dielectric thickness for the actuators $D1 - D4$ and of the dielectric material for actuator D5 becomes obvious. Applying the correlation in Equation (4.8) to the results of the integrated gray values GV, the lines collapse for the actuators $D1 - D4$ in the scaled force-gray value diagram in Figure 4.14(b). The influence of the dielectric material with the actuator $D5$ is reduced, but due to the overestimation of the integral gray-value, the lines of actuator $D5$ and the actuators $D1 - D4$ do not collapse. The unclear influence of the reflectivity of the dielectric surface needs to be

investigated further. Nevertheless, the results for the actuators $D1 - D4$ imply that the Equation (4.4) is resonable for variation in the dielectric thickness.

4.1.4 Summary of the Direct Force Scaling

The two options of directly influencing the induced body force in its magnitude and distribution: operating conditions and geometry respectively, are investigated with three independent and simultaneously applied analysis methods. Electrical characteristics, light emission of the discharge, and direct thrust measurements are used to characterize the different parameter influences. With the three measures the influence on the actuator performance is quantified and more universal scaling laws are developed. These empirical scaling laws were derived for the relation of the electrical characteristics, such as applied voltage and power consumption, and the interrelation of the produced thrust with the electrical characteristics. These scaling laws allow to compensate the influence of the above mentioned parameters. The robustness and the generality of these scaling laws were demonstrated with data found in literature and with an alternative expression of this scaling laws using the plasma luminosity instead of the consumed power.

The scaling law for the electrical characteristics could be summarized to one general relation of the consumed power, applied voltage, operating frequency and the influence of the thickness and material constant of the dielectric layer.

$$\frac{P_A/L}{fV^{7/2}} \cdot \frac{\epsilon}{d} = const \tag{4.9}$$

Analogue to this, the interrelation of the produced thrust with the electrical characteristics, dependent on the actuator setup and the operating conditions, could be summarized to the following equations:

$$V^{7/2} \quad \propto \quad F_t \frac{1}{f^{1/4}} \frac{d^{1/2}}{\epsilon^{3/10}} \tag{4.10}$$

$$P_A \quad \propto \quad F_t \cdot f^{3/4} \cdot \frac{\epsilon^{7/10}}{d^{1/2}}. \tag{4.11}$$

These scaling laws allow to predetermine changes in the performance of an actuator, based on one known configuration. Changes in the produced thrust and consumed power can be estimated. The layout and the design

of the actuator for an experimental setup can be based on a target configuration. Premised on robust and general valid scaling laws, a more universal development of empirical actuator models for numerical simulations is possible. This allows a better comparability of experiment and simulation.

Even though these new scaling laws (4.9), (4.11), (4.11) seem promising to describe and classify the consumed electrical power and produced thrust of DBD plasma actuators for varying operating conditions and changes in the dielectric, these correlations do not include any information about changes of the electrode arrangement. For a better comparability of experiments of different research groups, it is also necessary to quantify the influence of those additional geometrical parameters.

4.2 Indirect Scaling of the Induced Force

The pulsed operation of DBD plasma actuators is usually referred to the unsteady force agitation as it is used for the excitation or the active damping disturbances in the flow for the control of separated flow [20, 69, 94] or the damping of disturbances in the boundary layer [54, 89]. But, the pulsed operation also yields the possibility to reduce the time-averaged force production, as shown by Porter *et al.* [120]. There, the plasma actuator was operated at duty cycles (DC) of 10%, 50% and 100%, this reduced the mean force production significantly, but no direct proportional relation of the reduced force and the applied duty cycle is apparent.

To determine the reduction rate of the produced force, the differential force estimation is used to analyze the influence of the pulsed operation. The standard actuator operated at $f = 10$kHz and an applied voltage of $V = 6$kV and $V = 7$kV is modulated at a frequency of $f_{mod} = 250$ and 500Hz with different duty cycles. As a requirement to assume a quasi-steady time-averaged force production by the pulsed operation, the actuator has to be operated at a sufficiently high modulation frequency concerning the time scales of the flow under investigation. Thus; the plasma operating frequency f has to be chosen high enough, since at least a certain number of discharge cycles has to be within the on-pulse of the modulation. The relationship between the modulation frequency $f_{mod} = \frac{1}{T_{mod}}$ and the operating frequency of the plasma f is explained in Figure 4.15. The higher frequency is the plasma operating frequency. In this sketch two periods of the modulation frequency are shown with a duty-cycle of 50%

This ideal signal shape cannot be directly transferred to the high-voltage

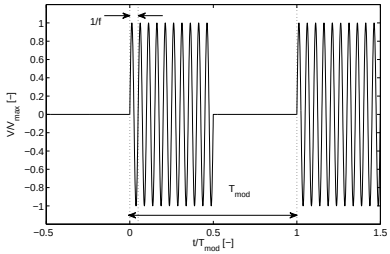

Figure 4.15: Schematic sketch of the driving voltage for the pulsed operation

signal, since the plasma actuator and the high voltage generator resemble an oscillating circuit with a certain transient behavior. An example of the transient behavior is shown in Figure 4.16 for the standard actuator operated at a frequency of $f = 10\text{kHz}$ modulated at $f_{mod} = 500\text{Hz}$ with a duty cycle of DC = 50%. Due to this transient oscillation some periods of the plasma operating frequency are required to reach the maximum amplitude of the high voltage signal and after the shut down of the actuator, during the off period, a post-pulse oscillation of the system is observable.

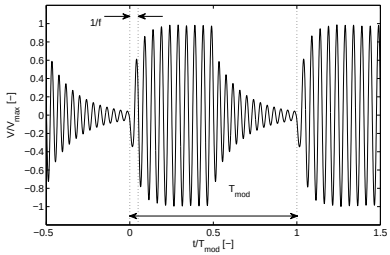

Figure 4.16: Measured driving voltage for the pulsed operation

This transient oscillation, observed with the high-voltage generator, requires operation of the actuator at the resonance frequency of the whole electric circuit. When the actuator is modulated the operation at the resonance frequency prevents an overshoot in the high-voltage signal and reduces the transient behavior.

4.2.1 Force magnitude

The plasma actuator operated at $V = 7$kV and a frequency of $f = 10$kHz shows a reduction in the consumed power when it is modulated at $f_{mod} = 250$Hz with varying duty cycles (DC = 20%-100%). The relative consumed power, shown in Figure 4.17, reveals a linear relation with the duty cycle of the modulation, but no direct proportional scaling is observed. The red line in Figure 4.17 shows a linear fit with a slope of 4.3% change in the relative power consumption with a change of 10% in the duty cycle.

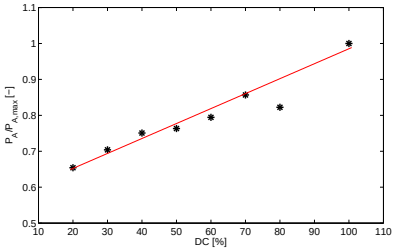

Figure 4.17: Relative consumed power P_A at varying DC with the modulation frequency of $f_{mod} = 250$Hz.

This can be explained with the post-pulse oscillation of the system. The duration of this oscillation is dependent of the characteristics of the oscillating circuit, of high-voltage generator and plasma actuator. Therefore the relation of the pulse duration and the duration of the post-pulse oscillation changes with varying duty cycle. As long as the amplitude of the post-pulse oscillation is below the onset voltage, the pulse width of the modulation is not affected and the consumed power in the post-pulse oscillation is referred to passive power losses.

Some discharge cycles are required for the amplitude of the voltage to achieve the maximum of $V = V_{\max}$. This transient oscillation in the beginning of the modulation pulse could also affect the force production.

The relative force magnitude $F_x/F_{x,\mathrm{DC}\,=\,100\%}$ (based on Equation (3.3)) for different duty cycles is shown in Figure 4.18 and is normalized with the force at the continuous operation (DC = 100%). The actuator was operated at an applied voltage of $V = 7$kV and the operating frequency ($f = 10$kHz) was modulated with a frequency of $f_{mod} = 250$Hz and $f_{mod} = 500$Hz. It can be seen that the force magnitude F_x is not linearly scaled with the chosen duty cycle. A quadratic fitting is applied to the mean force and is

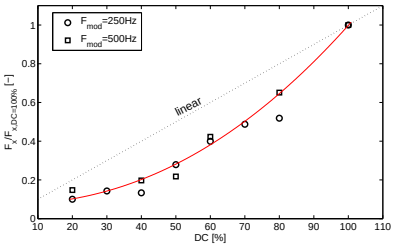

Figure 4.18: Relative force magnitude F_x at varying DC with the modulation frequency of $f_{mod} = 250\text{Hz}$ and $f_{mod} = 500\text{Hz}$.

shown with the red line in Figure 4.18. It clearly shows, that a smaller duty cycle is less efficient in accelerating the flow.

The fluid mechanic effectiveness η^*_{FM} is shown in Figure 4.19, for different duty cycles and at a modulation frequency of $f_{mod} = 250\text{Hz}$.

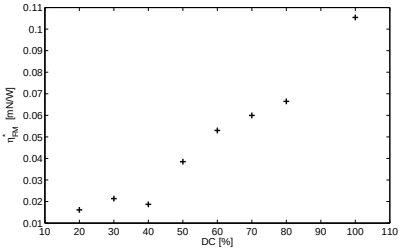

Figure 4.19: Fluid mechanic effectiveness η^*_{FM} for a modulated actuator ($f_{mod} = 250\text{Hz}$) in dependency of the duty cycle

For a small duty cycle of DC = 20% the effectiveness of the actuator is approximately one order of magnitude smaller than for the continuous operation. The effects of the transient and post-pulse oscillation with the oscillating circuit, the reduced force production at the beginning of the pulse and the passive power losses after the pulse, are not influenced by the pulse duration. Thus the relative share becomes more pronounced with a reduced duty cycle, resulting in a decrease of the effectiveness.

Velocity-Field Evolution During a modulation period the flow is accelerated and with the plasma turned off the flow decelerates . Boucinha *et al.* [15] performed time-resolved velocity measurements with an actuator operated in pulsed mode in quiescent air. The actuator was operated at a low frequency of $f = 500$Hz and pulsed at 10 Hz. There, it can be seen that a time of 10ms was required to achieve a constant velocity during the on-pulse. In the investigation of Benard *et al.* [11] time-resolved velocity measurements with an actuator operated at a frequency of $f = 1500$Hz and varying modulation frequencies where performed. There, a time of 5ms was required to achieve a constant velocity during the on-pulse. This time is presumably dependent on the operating frequency and decreases with increasing frequency.

With PIV based velocity-field measurements, acquired at a frequency of 10kHz synchronized to the plasma operating frequency, phase-averaged velocity fields could be obtained for the velocity evolution during a modulation period. Since the operating frequency is 20 times larger than the modulation frequency of $f_{mod} = 500$Hz, the modulation period could be divided into 20 bins. The phase-averaged velocity-field measurements yielding the fluctuation of the velocity-field distribution with the discontinuous force production.

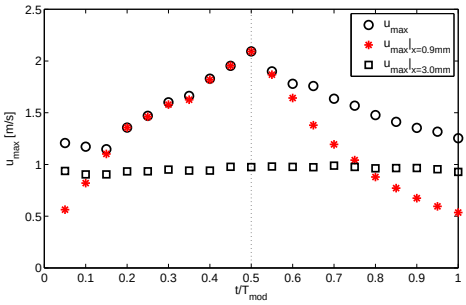

Figure 4.20: Phase-averaged evolution of the maximum velocity in the flow field (∘) and the maximum velocity at $x = 0.9$mm (∗) and $x = 3$mm (□) downstream of the upper electrode.

In Figure 4.20 the maximum velocity of the flow field (∘) and the maximum velocity at two downstream positions at $x = 0.9$mm (∗) and $x = 3$mm (□) are presented for a duty cycle of DC = 50%. At the beginning of the

pulse the maximum velocity in the flow field ($\circ$) shows a still decreasing velocity. This demonstartes that the induced velocity is not convected downstream or dissipated completely. With the maximum velocity in the flow field and the maximum velocity at the downstream position of $x = 0.9$mm ($*$) it can be clearly seen that no constant velocity is achieved during the on-pulse. The position $x = 0.9$mm resembles the position of the maximum velocity at $t = 0.5 \cdot T_{mod}$. Here the largest velocity fluctuations could be expected.

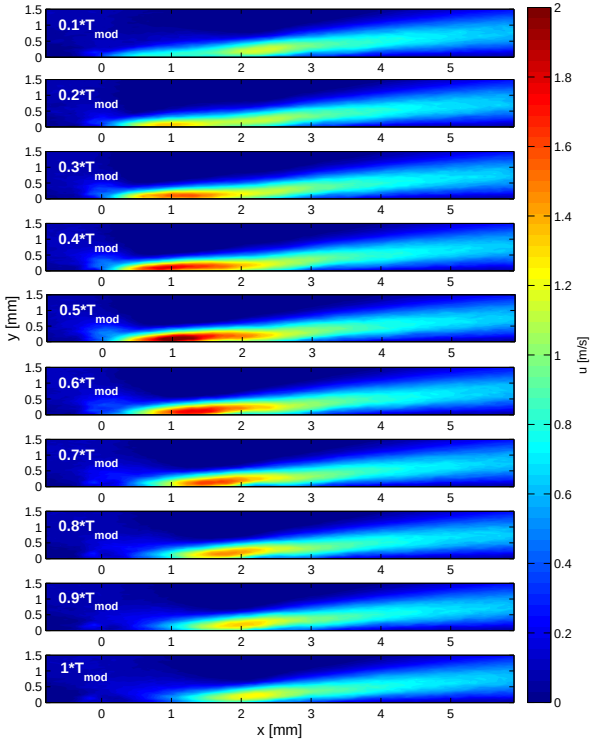

Figure 4.21: Flow field distributions for different phase angles of the modulation period at $f_{mod} = 500$Hz and $V = 7$kV at DC $= 50\%$.

The velocity fluctuation is restricted to an area close to the upper electrode, since the maximum velocity at $x = 3$mm (□) downstream of the upper electrode does not reveal any significant fluctuations. This behavior can also be seen in the evolution of the flow field distribution. In Figure 4.21 the flow field distributions for different phase angles of the modulation period are shown. At $t = 0.1 \cdot T_{mod}$ the pulse starts, and a small spot of a low velocity arises. This spot is continuously growing in intensity until $t = 0.5 \cdot T_{mod}$ when the pulse stops. Between $t = 0.6 \cdot T_{mod}$ and $t = 1.0 \cdot T_{mod}$ this spot is convected downstream and reduced in magnitude. It is still visible as a second maximum in the flow field when the next pulse starts at $t = 0.1 \cdot T_{mod}$. Further downstream no fluctuations in the induced wall-jet can be distinguished.

With the modulation frequency $f_{mod} = 250$Hz the number of bins increases to 40 bins per modulation period. In Figure 4.22 the maximum velocity in the flow field (○) and at two downstream positions at $x = 1.5$mm (∗) and $x = 3$mm (□) for a duty cycle of DC = 50% and the lower modulation frequency are presented.

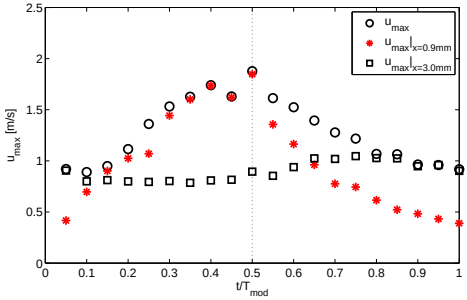

Figure 4.22: Phase-averaged evolution of the maximum velocity in the flow field (○) and the maximum velocity at $x = 1.5$mm (∗) and $x = 3$mm (□) downstream of the upper electrode, for an actuator operated at $V = 7$kV and modulated at $f_{mod} = 250$Hz aand DC = 50%.

The induced velocity does not reach a constant value with the lower modulation frequency either. But in comparison with the higher modulation frequency, shown in Figure 4.20, the deceleration of the flow during the off period reduces the velocity to a larger extent. Thus the maximum

induced flow velocity does not exceed the velocity with the higher modulation frequency. The position of the maximum velocity at $t = 0.5 \cdot T_{mod}$ moves downstream to $x = 1.5$mm for the lower modulation frequency, due to the longer acceleration period. Compared to the position of the maximum velocity with the continuous operation, as discussed in Section 3.3, a longer acceleration period would be required to produce the position of the maximum velocity at $x = 2$mm.

Regarding the fluctuation, still visible in the velocity plot for $x = 3$mm (□) in Figure 4.22, the flow field modulated at $f_{mod} = 250$Hz has a more unsteady character as compared to the higher modulation frequency.

With a larger duty cycle DC = 70% the maximum velocity at two positions at $x = 2$mm (∗) and $x = 3$mm (□) is analyzed and presented in Figure 4.23. With the longer acceleration period a constant velocity was achieved during the on-pulse of the modulation. Here, with a operating frequency of $f = 10$kHz a time of $t = 2$ms was required to achieve a constant velocity.

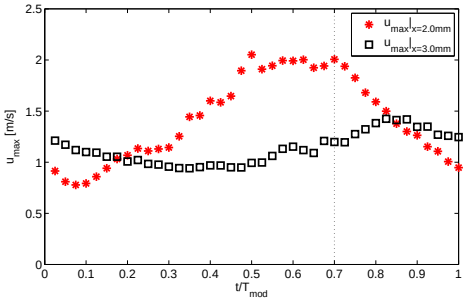

Figure 4.23: Phase-averaged evolution of the maximum velocity at $x = 2$mm (∗) and $x = 3$mm (□) downstream of the upper electrode, for an actuator operated at $V = 7$kV and modulated at $f_{mod} = 250$Hz and DC = 70%.

The more unsteady character of the wall-jet can also be seen in Figure 4.24, where the flow field distributions for different phase angles of the modulation period are shown. The wall-jet appears in a wavy structure in the entire field of view.

At the beginning of the pulse ($t = 0.1 \cdot T_{mod}$) a small region with higher velocity appears close to the upper electrode due to the beginning of the discharge. The second maximum is already convected farther downstream as compared to the flow field in Figure 4.21. The flow is accelerated until the

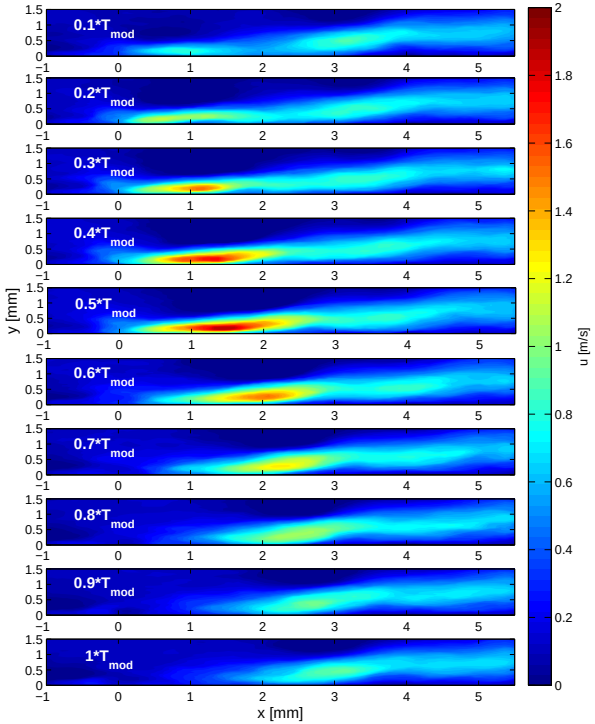

Figure 4.24: Flow field distributions for different phase angles of the modulation period at $f_{mod} = 250$Hz and $V = 7$kVat DC $= 50\%$.

end of the pulse ($t = 0.5 \cdot T_{mod}$) and starts to decay during the off period between $t = 0.6 \cdot T_{mod}$ to $1.0 \cdot T_{mod}$. The distances between the single spots of higher velocity reach a larger extent at the modulation frequency $f_{mod} = 250$Hz.

With the time-dependent force field calculation as introduced in Equations (3.4) and (3.5), the development of the body-force can be estimated during modulation period T_{mod}. The time-dependent force magnitude is calculated by the integration of the force distribution, as described in Equation (4.12).

$$F_i(t)/L = \int_{y_{\min}}^{y_{\max}} \int_{x_{\min}}^{x_{\max}} f_i(x, y, t)\, \mathrm{d}x\, \mathrm{d}y. \tag{4.12}$$

The normalized force magnitude $F_x^*(t)$ during the modulation period for a duty cycle of 50% and a modulation frequency of $f_{mod} = 500\text{Hz}$ is shown in the upper diagram of Figure 4.25. In the lower diagram the corresponding normalized voltage signal is depicted. The force magnitude is normalized with the mean magnitude of the plasma-on phase (cp. Equation (4.13)].

$$F_x^*(t) = F_x(t)/\overline{F_{x,on}} \tag{4.13}$$

Assuming an ideal behavior of the force modulation, a constant force during the plasma-on phase could be expected as depicted with dotted lines in Figure 4.25. The real behavior shows that at least three discharge cycles are required to reach the maximum induced force.

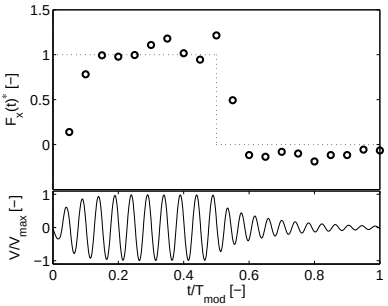

Figure 4.25: Evolution of the normalized force magnitude $F_x^*(t)$ during a modulation period with $f_{mod} = 500\text{Hz}$ and DC = 50%.

This correlates with the transient oscillation of the applied voltage, where also three discharge cycles are required to reach the maximum voltage. The temporal evolution of the force implies a linear scaling with the chosen duty-cycle of the modulation, but the mean force magnitude during the plasma-on pulse is smaller as compared to the force magnitude with the continuous operation. In the case of 50% duty cycle, the mean force magnitude reaches less than $0.8 \cdot F_x$ of the force magnitude of continuous operation. In combination with the reduced force at the beginning of

the plasma-on pulse this results in a strong reduction of the mean force magnitude averaged over the entire modulation period.

The cause of the reduced force magnitude has to be investigated further, since it cannot be distinguished with this investigations if the discharge is affected due to a reduced surface charge or if the reduced dielectric heating influenced the force production. Therefore further measurements with the gray value distribution of the light emission could give more insights.

Force-Field Distribution Beside the force magnitude of the pulsed operation, the force-field distribution and its extent are of interest for the approach of the indirect force scaling. In Figure 4.26 the contour lines for 10% of the force field maximum are shown for $V = 6$kV (dotted line) and $V = 7$kV (solid line) for the modulation frequency $f_{mod} = 500$Hz. The black line shows the 10% contour of the force field for a duty cycle of DC = 50% and the 100% duty cycle is display in red.

The extent of the force field is constant for varying duty cycles at a given applied voltage.

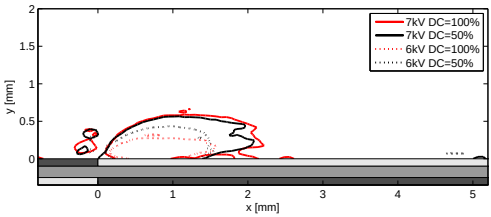

Figure 4.26: Contour lines with 10% of the force field maximum at $V = 6$ and 7kV for a DC = 50% and 100% duty cycle

4.2.2 Summary of the Indirect Force Scaling

It was demonstrated, that the time averaged force can significantly be reduced in its magnitude by operating the actuator in pulsed mode, whereas the force extent remained constant. The discontinuous force production or pulsed mode offers the possibility to decouple the force field magnitude and its extent to the greatest possible extent. To assume a time averaged constant force the plasma actuator has to be modulated at a sufficient high frequency. Which frequency is appropriate depends on the flow control

approach, the relevant time scales of the targeted flow and on the electrode arrangement. Operated in quiescent air at a modulation frequency of $f_{mod} = 500$Hz the actuator induces a fluctuating velocity field. The fluctuation of the velocity field is restricted to a small area close to the upper electrode. At a smaller modulation frequency ($f_{mod} = 250$Hz) the oscillation of the wall-jet sustain over a longer distance. This is correlated with the convective speed of the wall jet.

4.3 Summary - Scaling of the Induced Body Force

In the first part of this chapter the direct scaling of the force was introduced. Dependent on the parameters, plasma operating conditions and actuator setup, the influence on the produced thrust and power consumption was analyzed using three independent measures, such as electrical characteristics, direct thrust measurements and the light emission of the discharge. Empirical scaling laws were derived, to compensate the influence of the above mentioned parameters. These scaling laws were verified with data found in literature and with an alternative expression of this scaling laws using the plasma luminosity instead of the consumed power.
With the direct scaling of the force, by changing the actuator setup, the magnitude of the force is influenced mainly. The extent of the plasma or the extent of the force field grows linearly with the applied voltage, but this is coupled with an increase of the force magnitude. With a variation of the operating frequency the extent of the plasma is kept constant, but the force magnitude is influenced only in narrow range.

Adjusting the force magnitude and the force field extent independently for a certain actuator setup is only possible by indirect scaling.

The indirect scaling was addressed with second part of this chapter. The differential force field estimation, based on PIV measurements, was used to analyze the influence of the discontinuous operation on the force magnitude and the extent of the force field. It was demonstrated, that the time-averaged force magnitude can be adjusted in a wide range without changing the time averaged size of the force field. This is an essential perquisite for the experiments and investigations of the following chapters.

5 Plasma Actuator Vortex Generators

The aim of this section is the parameter identification of plasma actuators for active vortex generation in laminar boundary layers. The main intention here is the prolonged generation of longitudinal vortices over a significant streamwise distance. One promising application for arrays of streamwise vortices is to delay transition by spanwise modulating the streamwise velocity in a laminar boundary layer, as demonstrated by Fransson *et al.* [41] and Gürün and White [55]. Therefore, the experiments presented here focus on the streaks and their streamwise development that result from the vortices produced by the plasma actuators.

To generate stable streaks in a laminar boundary layer the spanwise modulation of the velocity inside the boundary layer must not exceed a certain amplitude. Direct numerical simulations performed by Andersson *et al.* [5], showed that there exists a critical streak amplitude around 26% of the free-stream velocity, above which the streaky base flow becomes unstable. With a strong forcing, the plasma actuators would themselves trigger the transition to turbulence. Thus the forcing of the plasma actuator has to be carefully adjusted to meet this requirement. It turns out that creating a low enough force magnitude is one of the major challenges. This is in contrast to the usual problem of plasma actuator research, where the actuator is in most cases not strong enough for achieving the desired effects.

In the following section the parameter influences are identified and discussed.

5.1 Parameter Influence: Identification

With the body force oriented perpendicular to the main flow direction, a longitudinal vortex begins to form. Measurements by Jukes *et al.* [70] have shown that a certain streamwise distance is necessary for the flow to develop a vortex under the influence of the transverse body force. Farther downstream the vorticity increases linearly until the end of the electrode is reached. Thereafter the vortex starts to decay. Several parameters influence the size, vorticity and the vertical and horizontal position of the vor-

tex cores, and these can be grouped into geometric parameters (**electrode spacing**, **width** and **length** and **dielectric thickness**), operating conditions (**voltage**, frequency and **consumed electric power**) and flow conditions (free stream velocity and boundary-layer thickness). The bold printed parameters are investigated qualitatively in this chapter. Before the the experimental setup and the results are presented, the influencing parameters are discussed based on the characterization and the scaling of the plasma actuator as introduced in Chapter 3 and 4.

Geometry

- **Actuator spacing:** In an array of actuators the distance between the active electrodes has a comparable effect to the spacing of passive devices, such as vane type vortex generators. However, the direct scalability of plasma actuators is limited concerning the independent choice of size and length of the discharge region and the forcing magnitude. Additionally, the electrodes cannot be placed arbitrarily close to each other without promoting an interaction between the discharge regions and the electric fields of two adjacent actuators. The distribution of the body force has its maximum at a distance from the active electrode of approx. $0.25 - 0.3 \cdot \Delta x_F$ in direction of the induced force. The size of the discharge region is correlated with the magnitude of the generated force. Both effects need to be considered for small actuator spacings.

- **Electrode width:** In an arrangement that produces counter rotating vortex pairs, the width of the upper electrode primarily influences the distance between the vortex pairs and thus the shape of the streaks, similar to the distance between the two vanes of a passive vortex generator producing a pair of counter-rotating vortices. By varying the width of the upper electrode at a constant spacing, the spanwise position of the vortex cores can be adjusted such that the vortices are distributed equally, i.e. the distance between two vortices of a pair have the same distance as the corresponding neighboring vortex.

- **Electrode length:** Usually the plasma actuator is considered as a 2D device and is applied for 2D problems. The force production is therefore usually quantified by force per meter length. This force (N/m) certainly is an important feature for the creation of vortices. However, in contrast to passive devices the vortex is created gradually

along the streamwise direction, therefore the vorticity of the resulting vortex directly depends on the electrode length in the streamwise direction, i.e. the electrode-parallel length of the discharge region. For a given plasma actuator (electrode dimension and dielectric material), the streak amplitude mainly depends on the force integrated along the electrode length. This implies, that for longer electrodes the forcing magnitude (applied operating voltage) must be reduced for producing a vortex of a given vorticity.

- **Thickness of the dielectric :** One major parameter simultaneously affecting the magnitude and size of the discharge region is the dielectric between the electrodes. Changes of its thickness and its material, directly influence the electric-field lines and their dependence on the applied voltage. The discharge only occurs where the electric field exceeds the breakdown-field strength. Both, the permittivity of the material and the distance between the electrodes affect the position of the breakdown-field line. Thinner dielectric layers increase the local electric field strength at a chosen voltage. The thickness of the dielectric therefore constitutes a further parameter for adjusting the forcing magnitude and discharge-region size.

Plasma Operation

- **Voltage:** The applied voltage has to exceed a certain level for a given device setup for the discharge to begin. Starting with this threshold voltage the discharge region grows in size and the integral force (N/m) increases. The applied voltage and the consumed power of the device are closely correlated. When operated near the threshold voltage, the discharge is very sensitive to imperfections concerning the distance of the electrodes, permittivity of the dielectric and the geometric accuracy of the electrodes. Variations of these parameters lead to a nonuniform discharge along the electrodes and from one actuator to the neighboring ones and, therefore, lead to non-constant growth of the vorticity along the length of the actuator. It is observed that this sensitivity is reduced when the actuator is operated well beyond the above mentioned threshold voltage. However, higher operating voltages stand in contrast to lowering the forcing magnitude. Since the operating voltage is closely coupled to the force magnitude and more important here; to the extent of the body-force region.

- **Operating Frequency:** Similar to the effect of the operating voltage, the plasma operating frequency is also closely correlated with the consumed power of the device and with the produced force magnitude. The consumed power increases linearly with increasing frequency, whereas the produced force magnitude is only scaled with $f^{1/4}$
- **Continous/pulsed mode:** The plasma actuator is operated at a high frequency high voltage usually of the order of tens of kHz and kV. During a discharge period the body force is not constant. However, this operating frequency can be chosen high enough such that the flow can be assumed to not be susceptible to this frequency. Furthermore, the amplitude of the operating frequency can be modulated at chosen frequencies. For example, the operating frequency can rapidly be turned on and off, leading to a force pulsed at the modulation frequency with a chosen duty cycle. Given that this amplitude modulation is of high enough frequency not to trigger any further instabilities, the option to operate the plasma actuator in pulsed mode is an interesting means to decouple the forcing magnitude and the size of the discharge region. By adjusting the duty cycle of the modulation, the time averaged force can be reduced without changing the size of the discharge region.

Additionally the outer flow conditions affect the vortex scaling, by means of control authority and the relative vortex size. For completeness these parameters are discussed at this point, but not included in the subsequent investigation.

Flow Conditions

- **Free-stream velocity:** As known from other flow control experiments with plasma actuators the ratio between the momentum of the free stream and the induced momentum (momentum coefficient C_μ) is an accepted measure for the dimensionless quantification of active flow-control actions. Usually the applicability of plasma actuators for flow control is very limited due to the limited force magnitude,resulting in low value of C_μ. It turns out that the generation of longitudinal vortices requires very low forcing magnitudes in the case that actuators with a significant streamwise length are to be used.
- **Boundary-layer thickness:** The penetration depth of the body-force region into the boundary layer in wall-normal direction is lim-

ited and cannot be easily varied or adjusted, due to the wall-normal thickness of the discharge region and the resulting distribution of the body force. The effect of the ratio of discharge region thickness to boundary-layer thickness on the vortex formation should be identified and certainly has an effect on the vortex formation.

5.2 Experimental Setup

The aim of the present investigation is the qualitative parameter identification for active vortex generation using plasma actuators in laminar boundary layers. The experiments presented here focus on the streaks and their streamwise development that result from the vortices produced with the plasma actuators.

The experimental data have been acquired in the large scale speed wind tunnel (NWK1) at the TU Darmstadt. This is a Göttinger-type tunnel with a vertical arrangement. The closed test section has a length of 4.8m and a cross section of 2.2m by 2.9m with a maximum velocity up to 68m/s. The turbulence level is approximately 0.2% at test speeds above 20m/s.

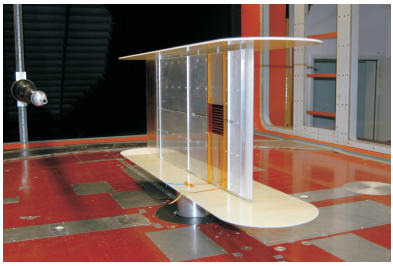

Figure 5.1: Experimental setup of the flat plate mounted in the test section.

The flat plate is made of acrylic glass with an elliptic leading edge and a length and width of 1.08m and 0.44m respectively. It was mounted vertically into the test section with end plates (see Figure 5.1). The plate has an exchangeable insert over the range $x = 170$mm to 290mm measured from the leading edge, allowing flush mounted actuator arrays to be positioned between $x = 175$mm and 275mm. The plasma actuator arrays were made of self-adhesive Kapton and copper tape. The copper tape has a thickness of 35μm and Kapton tapes of different thicknesses were available.

The standard actuator configuration is defined as an array of plasma

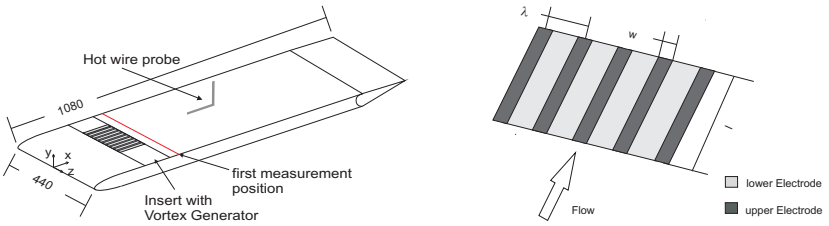

Figure 5.2: Sketch of experimental setup: a) flat plate; b) plasma actuator array, with a given electrode length L, electrode width w and spanwise spacing λ

actuators with a single large lower electrode and seven upper electrodes with a width of $w = 2$mm, a length of $l = 100$mm and with a $\lambda = 10$mm spanwise spacing. The dielectric layer has a thickness of $d = 0.33$mm. Plasma is generated on both sides of the active upper electrodes. Thus, each upper electrode produces a pair of counter-rotating vortices. The discharge length l_p is defined as the sum of the lengths of all active edges of the upper electrodes. For the standard configuration the total discharge length is $l_p = 1.4m$. The operating conditions for the standard configuration was an operating voltage of $V = 4$kV and a carrier frequency of $f = 8$kHz. Figure 2 shows the setup on the flat plate including the coordinate systems origin (a) and the geometrical definition of a vortex generator array (b).

The velocity data were acquired with a Dantec StreamLine CTA system placed downstream of the plasma actuator at a sufficient distance to the active electrodes ($x > 300$mm) to prevent arcing between the actuator and the CTA probe, and also to reduce the electronic noise due to electromagnetic disturbances. In the post-processing the data were smoothed using a Savitzky - Golay smoothing filter.

5.2.1 Base Flow

For all experiments the flow velocity was set to $U_\infty = 8\frac{\mathrm{m}}{\mathrm{s}}$. Using the deflection of the trailing edge flap, the pressure gradient along the plate was adjusted to be close to zero. In Figure 5.3 the measured boundary-layer thickness δ_{99} is compared to the Blasius solution and the downstream development of the shape factor H_{12} of the base flow configuration is shown.

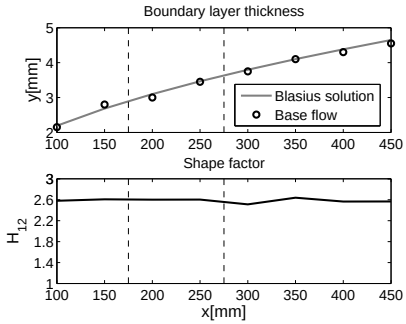

Figure 5.3: Boundary-layer thickness and shape factor of the base flow configuration. The dotted lines show the size of the exchangeable insert in which the actuators can be mounted.

5.2.2 Measurement Procedure

There are several reasons to minimize the measurement time for any one set of operating conditions. Over long periods of operation the performance of the plasma actuators can change due to deterioration of the Kapton tape, in some cases eventually leading to breakdown and failure of the actuator. Since the actuators are handmade, they differ slightly from one another and therefore it is preferable to perform all measurements for one configuration with a single actuator. Any remaining performance variation over one set of measurements can be largely compensated using a closed-loop control circuit as demonstrated by Kriegseis *et al.* [86].

To maintain short measurement times only selected profiles of the streamwise velocity component were measured. At all selected downstream positions one spanwise (wall-parallel) traverse and one wall-normal traverses were performed. The spanwise distribution of the streamwise velocity component was measured at the wall-normal position where the base flow reached 50% of the freestream velocity. This measurement procedure is sketched in Figure 5.4, where the green curve represents the spanwise velocity profile. Using this information the exact positions of the high-speed streak and the low-speed streak could be determined. In a second step the velocity profile normal to the wall was measured for each of the high-speed ($u_{max}(y)$) and low-speed ($u_{min}(y)$) streaks (displayed in Figure 5.4 in blue and red respectively). From these wall-normal profiles the streak amplitude was expressed with respect to the outer, freestream velocity as:

$$A_{st} = \max_{y} \left\{ \frac{u_{max}(y) - u_{min}(y)}{2} \right\} / U_{\infty}. \tag{5.1}$$

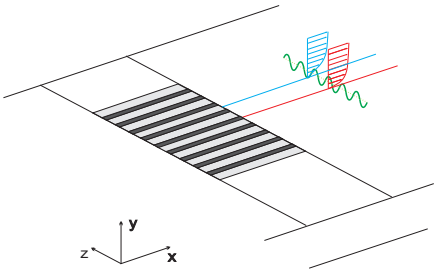

Figure 5.4: Schematic diagram of the measurement procedure. Wall parallel measurements marked in green, boundary-layer profiles in the high-speed (red) and low-speed streak (blue)

The evolution in streamwise direction of the estimated streak amplitude A_{st} according to equation (5.1) is shown in Figure 5.5(a). The normalized, spanwise modulation of the streamwise velocity derived from the wall-parallel measurements is shown in Figure 5.9.

Before presenting the results, the influence of the different parameter is discussed. The relevant parameters can be grouped into geometry, plasma operation and flow conditions. All parameters are to some extent linked, and there is a connection between effects from the geometry parameters and those from the parameters of plasma operation. For generating equally distributed streaks in a laminar boundary layer, it is necessary to adjust all parameters carefully.

5.3 Results: Streak Generation

In the preliminary experiments the parameter combinations shown in Table 5.1, were investigated:

Parameter: Electrode Length and Spanwise Spacing Figure 5.5 shows a comparison of the streamwise development of the streak amplitudes, as

Label	L	λ	d	w	Dielectric	V	DC	Parameter
PA1	100	10	0.33	2	Kapton	4	17	Basis
PA2	75	10	0.33	2	Kapton	4	17	Electrode length
PA3	100	8	0.33	2	Kapton	4	17	Spanwise spacing
PA4	80	8	0.33	2	Kapton	4	17	Electrode length
PA5	100	10	0.33	2	Kapton	4.8	17	Voltage
PA6	100	10	0.33	2	Kapton	4	13	Duty Cycle
PA7	100	10	0.165	2	Kapton	4	17	Dielectric thickness
PA8	100	10	0.165	3	Kapton	4	17	Electrode width
PA9	90	8	0.38	2	AL_2O_3	4	17	Dielectric material

Table 5.1: Overview of the investigated parameter combinations. Geometrical parameters have the dimension [mm] the voltage V is given in [kV]

defined in equation (5.1) and shown in Figure 5.4, for four different cases: Two cases with 10mm spacing (Figure 5.5(a)) and two cases with 8mm spacing (Figure 5.5(b)). Two different electrode lengths were tested for each spacing.

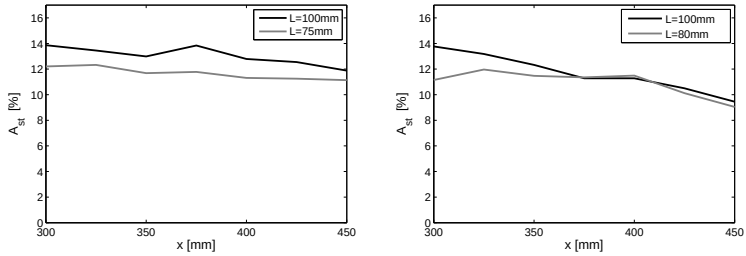

(a) (b)

Figure 5.5: Evolution of the streak amplitude and spanwise velocity modulation with varying electrode length for (5.5(a)) 10mm spanwise spacing (PA1 and PA2) and (5.5(b)) 8mm spanwise spacing (PA3 and PA4).

For the shorter actuator array, another detail requires attention: The 75mm actuator in Figure 5.5(b) consists of two arrays of 37.5mm length separated by 25mm in streamwise direction (Figure 5.6(b)), whereas the

80mm array is a single piece, as sketched in Figure 5.6(d). The end position for the array with the 80mm electrodes is located at $x = 255$mm. A small part of the difference in the amplitudes in Figure 5.5(b) results from the different end position of the arrays.

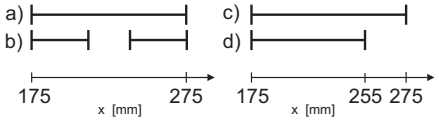

Figure 5.6: Sketch of actuator positions for the configurations a) PA1; b) PA2; c) PA3; d) PA4

The two-piece array demonstrates the possibility to energize vortices with separated and/or cascaded actuator arrays to cover a longer downstream distance.
The preliminary conclusions that can be drawn from this comparison are the following: A smaller spacing leads to stronger decay rates of the streak amplitudes, independent of the streak amplitude at the first measurement position; A reduced actuator length with constant operating voltage leads to lower streak amplitudes, qualitatively according to the reduction in length and therefore to the applied power per electrode or vortex; Actuators may be composed of several segments in streamwise direction and a significant gap between two parts does not seem to cause difficulties. It is easily possible to re-energize an already existing vortex.

Parameter: Operating Voltage Increasing the operating voltage yields a higher streak amplitude at the first measurement position as shown in Figure 5.7. Clearly, the operating voltage is the primary means for adjusting the vorticity and thereby the streak amplitude. It appears that increasing the operating voltage does not affect the decay rate. The mean consumed power was $\frac{\overline{P}}{l_p} = 0.73$W/m and $\frac{\overline{P}}{l_p} = 0.81$W/m for the 4kV (PA1) and 4.8kV (PA5) experiment, which correlates to the increase in streak amplitude.

The range of applicable operating voltages is very limited for this type of plasma actuator. On the one hand a minimum voltage is required for the discharge to occur and a maximum voltage must not be exceeded to avoid triggering transition. Generating low forcing magnitudes was a major issue in this investigation. This is in contrast to many other applications of DBD plasma actuators, where often higher forcing magnitudes are desirable. This challenge of maintaining a discharge a low voltage levels can be

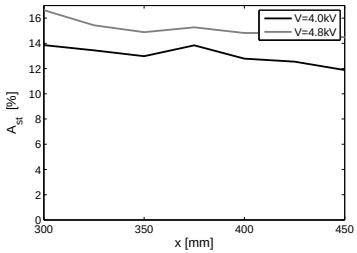

Figure 5.7: Evolution of the streak amplitude and spanwise velocity modulation with varying applied voltages (PA1 and PA5)

met by reducing the thickness of the dielectric layer between the electrodes.

Parameter: Pulsed Operation As already mentioned it can be difficult to operate plasma actuators with very low forcing magnitudes. Simultaneously the size of the discharge volume shrinks with lower operating voltages. This can be detrimental for the generation of vortices of certain dimensions. An operation of the arrays in pulsed mode at a certain modulation frequency and duty cycle offers the possibility to reduce the time averaged force production while keeping the size of the discharge volume constant as demonstrated in Chapter 4. In the case shown in Figure 5.8 a standard actuator configuration was operated in burst mode at a plasma operation frequency of $f_p = 8$kHz modulated at a frequency of $f_{mod} = 300$Hz with two different duty cycles (PA1 $DC = 17\%$ and for PA6 $DC = 13\%$).

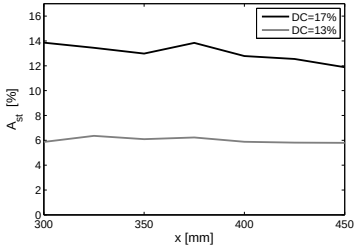

Figure 5.8: Evolution of the streak amplitude and spanwise velocity modulation with varying duty cycles (PA1 and PA6)

Ideally the modulation of the carrier frequency is rectangular, yielding an idealized square-wave shaped body-force time trace. For duty cycles other than 100% the time averaged produced force is reduced. In the experiments shown in Figure 5.8 the mean power per discharge length was reduced from $\frac{\overline{P}}{l_p} = 0.73\frac{\mathrm{W}}{\mathrm{m}}$ at 17% duty cycle to $\frac{\overline{P}}{l_p} = 0.45\frac{\mathrm{W}}{\mathrm{m}}$ at 13% duty cycle. Concerning the resulting drop of the initial streak amplitude for both cases, no good correlation could be found so far.

The reason for this nonlinear behavior can be found in the reduce fluid mechanic effectiveness (η^*_{FM}) for a smaller duty cycle as discussed in Chapter 4.

Figure 5.9 shows the direct comparison of the normalized, spanwise modulation downstream of the streamwise velocity for the standard actuator array (PA1) and the same array operated at a different duty cycle (PA6) is shown.

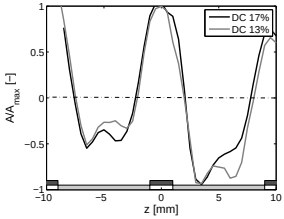

Figure 5.9: Normalized, spanwise modulation of the streamwise velocity for different duty cycle (PA1 with $DC = 17\%$ (solid line) and PA6 with $DC = 13\%$ (dotted line)), measured at $x = 300$mm and $y(u = 4\frac{m}{s})$; electrode positions marked in grey

Due to this normalization the difference in amplitude, as seen in Figure 5.8, is not visible in Figure 5.9. In contrast to the streak amplitude the spanwise distribution of PA1 and PA6 do not reveal large differences. This clearly shows that the streak amplitude can be adjusted without influencing the spanwise distribution of the streaks and confirms the possibility to adjust the desired force magnitude and the size of the body force region independently.

Parameter: Thickness of the Dielectric In Figure 5.10 the evolution of the streak amplitudes for the standard configuration (PA1) and an array with half the thickness of the dielectric (PA7) is shown. The applied

voltage is the same for the two configurations. For the thinner dielectric the breakdown field strength is reached for a lower applied voltage and the consumed power is higher compared to the standard configuration with the same applied voltage. For the configuration with the thinner dielectric less than 50% of the streak amplitude is achieved as compared to the standard array, even though the applied voltage is the same.

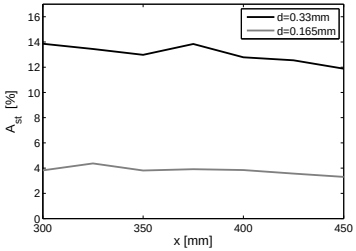

Figure 5.10: Evolution of the streak amplitude and spanwise velocity modulation with varying dielectric thickness (PA1 and PA7)

The effect of the dielectric thickness on the actuator performance is shown in Section 4.1.3. It was demonstrated that the force increases with a thinner dielectric layer at a constant applied voltage, whereas the consumed power increases antiproportional with the dielectric thickness. It could also be seen that the plasma extension is also affected in a small range.

In the present investigation smaller streak amplitudes were achieved with the thinner dielectric. Even though a stronger force can be expected for the thinner dielectric the achieved streak amplitude is smaller than for the thicker dielectric. This can be explained by the fact that not only the force increases but simultaneously the size of the body force volume shrinks also in wall-normal direction. This could be seen in the work of Benard *et al.* [10], where the force-field distribution was evaluated with a significantly lager dielectric thickness. The thinner dielectric leads to smaller and more concentrated vortices which do not interact strong enough to create a single large streaks between the vortices.

Parameter: Width of the Upper Electrode Next, the electrode width was increased from $w = 2$mm (PA7) to $w = 3$mm (PA8) for the configuration with the thin dielectric $d = 0.165$mm. The normalized, spanwise

modulation $\frac{A}{max(|A|)}$ is presented in Figure 5.11 for the two different electrode widths.

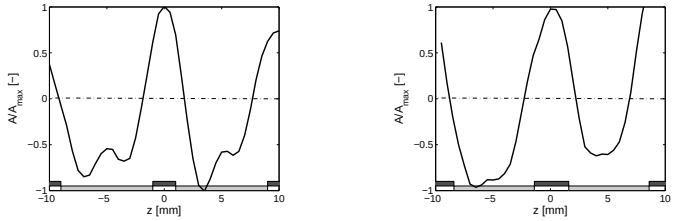

(a) (b)

Figure 5.11: Normalized, spanwise modulation of the streamwise velocity for different electrode widths (a) $w = 2$mm PA7 and b) $w = 3$mm PA8), measured at $x = 300$mm and $y(u = 4\frac{m}{s})$; electrode positions marked in grey

The relative widths of the high-speed and low-speed streak for the wider electrodes ($w = 3$mm) in Figure 5.11(b) are more equalized than with narrower electrodes ($w = 2$mm) in Figure 5.11(a). A double minimum is visible in the low-speed streak with narrower electrode ($w = 2$mm) in Figure 5.11(a), presumably caused by the larger separation of the small vortices. On the one hand it is desired that the interaction of single vortices quickly produces a single low speed streak; on the other hand equal widths of the high speed and the low speed streaks are required. Both features can be influenced by the width of the upper electrode as Figure 11 shows.

Regarding the evolution of the streak amplitudes and spanwise modulation in the streamwise direction for these thin dielectric configurations (PA7 in Figure 5.10 and PA8 in Figure 5.12), they seem not to be appropriate to create sufficiently strong amplitudes. The streak amplitudes A_{st} derived from the boundary-layer profiles and the amplitudes of the wall-normal measurements for $A_{50\%}$ range from 6% to 3% in Figure 5.12. The evolutions for the streak amplitude A_{st} and the spanwise modulation $A_{50\%}$ for both configurations do not show a good correlation. This reveals that measuring such weak streaks is a very difficult task with the current setup.

Parameter: Dielectric Material As mentioned before, the durability of the plasma actuators is limited due to the aging and wear of the chosen

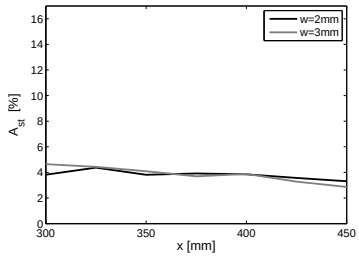

Figure 5.12: Evolution of the streak amplitude and spanwise velocity modulation with varying electrode width (PA7 and PA8)

dielectric material. It is necessary to use higher quality material for such actuators. Thus, ceramic plates were tested as dielectric material (PA9) to compare their performance concerning durability and operation.

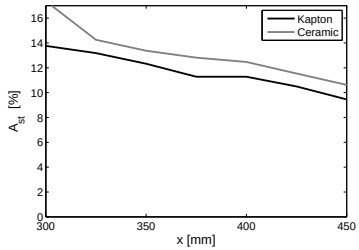

Figure 5.13: Evolution of the streak amplitude and spanwise velocity modulation with different dielectric material (Kapton PA3 and Ceramic PA9)

Alumina plates (Al_2O_3) of 0.38mm thickness were used with $w = 2$mm wide electrodes and a spanwise spacing of $\lambda = 8$mm and a length of $l = 90$mm. The applied voltage was set to $V = 4$kV, although the consumed power per meter was nearly two times larger than with the corresponding Kapton configuration. Since the power consumption scales linearly with the dielectric constant and the force is slightly increased with increasing dielectric constant, the effectiveness is reduced. Figure 5.13 shows the streak amplitudes for the ceramic material and the configuration with Kapton material. The amplitudes are different due to the different induced forces,

but the general features are the same.

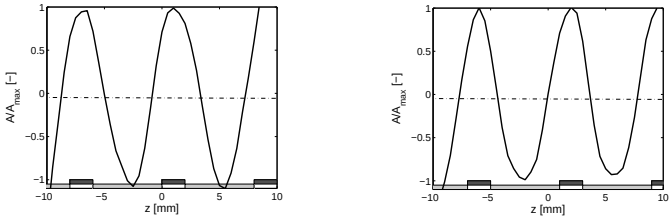

Figure 5.14: Normalized, spanwise modulation of the streamwise velocity for different dielectric materials (a) Kapton dielectric (PA3) and b) Alumina dielectric (PA9)), measured at $x = 300$mm and $y(u = 4\frac{m}{s})$; electrode positions marked in grey

Figure 5.14 shows the normalized distribution of the low-speed and high-speed streaks for the Kapton and for the ceramic actuators at a streamwise position of $x = 300$mm. Note that the configuration PA3 and PA9 with a spanwise spacing of $\lambda = 8$mm and an electrode width of $w = 2$mm are compared here. The distribution, amplitudes and the shape of the streaks are more uniform compared to the distribution in Figure 5.11. If the actuator is operated close to the lower voltage limit, the discharge is very sensitive to imperfections of the dielectric, to the alignment of the electrodes and to the level of wear of the actuator, which causes additional difficulties due to the non-uniformity of the discharge. The non-uniformity of the discharge as can be seen in the streak distribution in Figure 5.11 could be reduced considerably considering the level of wear of the actuators.

5.3.1 Summary

This qualitative investigation of plasma actuators for active vortex generation shows the complex interaction of numerous parameters. For evaluating the performance of the actuators, hot-wire measurements were conducted to capture the high-speed and low-speed streaks in the boundary layer generated by the vortices. The investigations clearly show that the geometry of the plasma actuator array, such as electrode spacing and electrode width, have an influence on the spatial distribution of the streaks, similar to the corresponding parameters of passive vortex generators. Furthermore, extending the electrode length in streamwise direction at constant operating

voltage yields higher streak amplitudes, which implies that the applied power per electrode or vortex is the governing parameter for the resulting vorticity. This conclusion is further supported by the increasing streak amplitudes with increasing operating voltages. However, modifying the operating voltage is only possible in a narrow range: with a minimum voltage required for the discharge to occur and a maximum voltage at which transition is directly triggered. With the pulsed operation of the vortex generator array a new possibility for the independent adjustment of force magnitude and force region has been introduced, representing an important parameter for the scalability of plasma actuator vortex generators.

5.4 Vortex Identification with PAVGs

To gain more insight into the vortex formation with an array of plasma actuator vortex generators, optical PIV measurements with a stereo camera configuration were carried out.

Jukes and Choi [70] investigated the vortex formation with a single plasma actuator vortex generator at a free-stream velocity of $U_\infty = 2.04$m/s and a strong actuation with a velocity ratio of the induced velocity of the plasma actuator with the free-stream velocity of $0.1 < U_p/U_\infty < 1.2$. Different angles of the upper electrode towards the flow direction and different streamwise extensions of the upper electrode were investigated. They demonstrated that the vortex circulation increases with the ratio of the induced velocity and the free-stream velocity and with actuator length. The vortex circulation was maximized when the electrode was orientated parallel to the flow. A comparison of the circulation conducted with a single PAVG and arrays of co-rotating and counter-rotating PAVGs with different ratios of $0.1 < U_p/U_\infty$. In [71] Jukes and Choi extends the parametric study of Jukes and Choi [70] to provide a more in-depth understanding of the mechanisms of streamwise vortex generation by PAVGs. As mentioned earlier they investigated the formation process of a single longitudinal vortex created by means of a single spanwise forcing plasma actuator in comparison with a passive vane-type vortex generator. The formation was identified as twisting and folding of the spanwise vorticity in the boundary layer of the oncoming flow. The comparison of the vortex trajectories of the plasma actuator vortex generator with the one of passive vane-type vortex generator reveal, that the vortices created by means of the plasma actuator experience a larger spanwise shift.

The focus in the following investigation is the vortex formation in an array of PAVGs with a small spanwise distance operated at small power consumption to create stable streaks in a laminar boundary layer.

5.4.1 Experimental Setup

The experiments were conducted on a flat plate in the low-speed wind tunnel facility (NWK2) of the TU Darmstadt. The NWK2 is small open return wind tunnel with a cross section of 450×450mm and a length of 2m, it is designed in the traditional Eiffel configuration. The contraction has an area ratio of 24:1, allowing for a maximum flow speed in the test section of 68 m/s.

The same flat plate as used in the previous section was originally designed to span the test section of the NWK2 without the end plates as used before.

The plasma actuator array was mounted onto the exchangeable insert of the flat plate as shown in Figure 5.2(a). The actuator was made of 0.3mm thick Cirlex and 17μm thick copper electrodes fabricated using PCB manufacturing techniques. For the masking material a photo resist was used which has been patterned by photolithography. The plasma actuator array was composed of 10 lower electrodes and 9 upper electrodes, resulting in 18 discharges: two on each side of the 9 upper electrodes. The width of the upper electrodes was $w = 2$mm each, with a streamwise length of $L = 45$mm and a $\lambda = 7$mm spanwise spacing. The streamwise position of the plasma actuator arrays is between $x = 235$mm and $x = 280$mm.

The laser sheet illuminated the y,z-plane from the side of the test section. The laser light was aligned parallel to the surface of the flat plate to reduce reflection from the electrodes. The cameras were positioned upstream and downstream of the laser sheet capturing the backward scattered light of the DEHS seeding particles. Six measurement positions in streamwise direction were distributed along plasma actuator array starting at the leading edge of the electrodes. Five measurement positions were distributed with the comparable streamwise distance in the wake of the actuator array as shown in Figure 5.15. The distances between the measurement positions are 10 mm, whereas the distance between measurement positions 5,6 and 7 is reduced to 5mm and the last measurement position is slightly further downstream with a distance of 15mm.

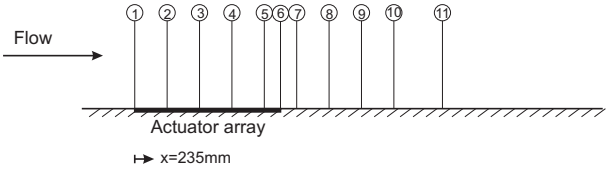

Figure 5.15: Schematic sketch of the measurement positions.

The velocity was acquired using a commercial PIV system, comprising a 15 Hz dual cavity flash-pumped Nd:YAG laser and two CCD cameras (*FlowSense 2M*) with a resolution of 1600×1220px with *Nikon* f=100mm lenses. The PIV system was operated in the double frame mode with a repetition rate of 10Hz with a total number of images of $N = 700$. Laser-sheet thickness was set to 3mm thus the time between the laser pulses was adjusted to $\Delta t = 50\mu s$. PIV processing was performed using Dantec

DynamicStudio v3.4. Velocity vectors were computed on a 16×16 pixel grid with 50% overlap using an averaging cross-correlation technique.

With a reduced image size of 1600×610px the obtained FOV spans a region of 50mm×10mm in spanwise and wall-normal direction.

5.4.2 Base Flow

The free-stream velocity was again chosen to $U_\infty = 8\frac{\mathrm{m}}{\mathrm{s}}$ for the experiments. The normalized boundary-layer profiles u/U_∞ at the wall-normal position η, where y is normalized with the Blasius length scale $\delta(x) = \sqrt{(\nu x)/U_\infty}$, in comparison to the theoretical Blasius solution in Figure 5.16 are shown. Considering the streamwise evolution of the shape factor H_{12} in Figure 5.16, an almost unaccelerated flow can be assumed.

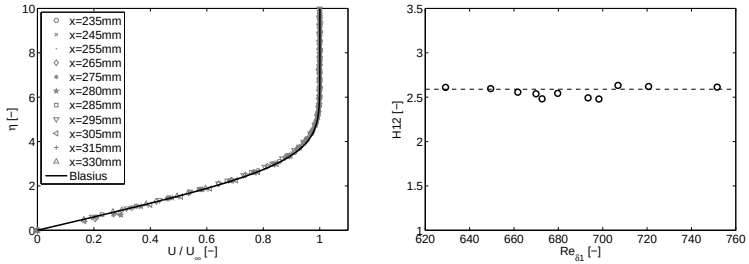

(a) Normalized boundary-layer profiles between $x = 115$ and 500mm

(b) Shape factor H_{12} in streamwise direction

Figure 5.16: Base flow characteristics

5.4.3 Plasma Actuator Vortex Generation

The plasma actuator array was operated at two different voltages of $V =$ 5kV and $V = 5.5$kV at a plasma operating frequency of $f = 10$kHz. To reduce the time averaged force production the plasma actuator was modulated at $f_{mod} = 500$Hz with a duty cycle of DC= 30% with a corresponding power consumption of $P = 0.425$W and $P = 0.53$W per vortex pair, respectively.

The modulation of the streamwise velocity component is shown in Figure 5.17 for position of $x = 280$mm and the higher power level ($V = 5.5$kV). The wall-normal direction is normalized with the boundary-layer thickness.

In spanwise direction two wave lengths of the modulation are shown. As demonstrated before in the previous section an evenly distributed modulation of the streamwise velocity could be achieved with the smaller spacing of 8mm) between the upper electrodes instead of 10mm. This can also be seen in Figure 5.17 with a further reduction of 1mm in the spanwise spacing.

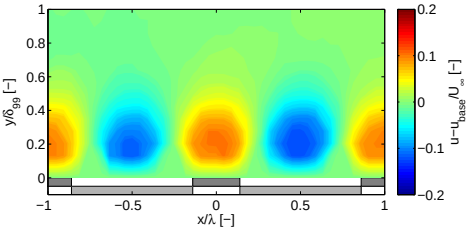

Figure 5.17: The modulation of the streamwise velocity component at $x = 280$mm, $V = 5.5$kV an $\lambda = 7$mm

The streak amplitude of the spanwise modulation of the streamwise velocity component was estimated using Equation (5.1).

The streamwise evolution of the streak amplitude is plotted in Figure 5.18 for both investigated power levels. The streamwise direction is normalized with the length of the actuator array L. As can be seen the streak amplitude increases gradually along the electrodes. With the higher power level the amplification of the streaks is increased and larger maximum amplitude is achieved.

As stated in the previous section the streak amplitude scales with the power consumption. In Figure 5.19 the streak amplitude as defined in using Equation (5.1) is related the consumed power per vortex pair. The slopes of the power related streak amplitudes for both cases show a very good agreement. For both cases the same maximum amplitude is achieved. This confirms the previous assumption that the streak amplitude scales with the power consumption.

Besides the spanwise and wall-normal distribution of the modulation for the streamwise velocity component, the longitudinal vortices causing the modulation can be identified.

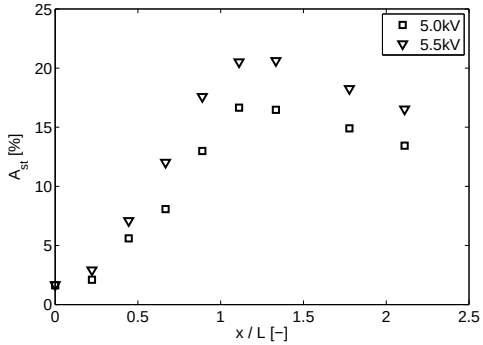

Figure 5.18: Streamwise evolution of the streak amplitude A_st for the voltage $V = 5$kV and $V = 5.5$kV at DC=30%

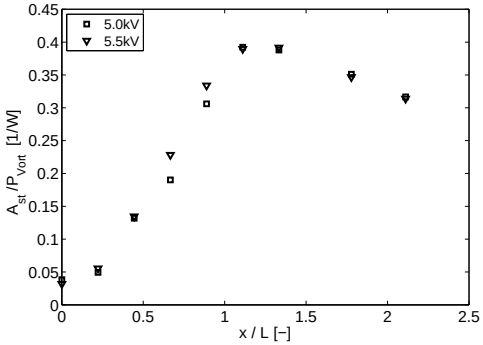

Figure 5.19: Streamwise evolution of the power related streak amplitude A_{st}/P for the voltage $V = 5$kV and $V = 5.5$kV at DC=30%

Vortex Identification The vortex identification functions introduced by Graftieaux *et al.* [50] are applied. The vortex identification functions $\Gamma 1$ and $\Gamma 2$ identify the locations of the center and boundary of the vortex on the basis of the velocity field.

The vortex center identification algorithm Γ_1 returns a dimensionless scalar.

$$\Gamma_1(P) = \frac{1}{N} \sum_S \frac{(PM \wedge U_M) \cdot e_\perp}{\parallel PM \parallel \cdot \parallel U_M \parallel} = \frac{1}{N} \sum_S sin(\Theta_M) \tag{5.2}$$

The variables in Equation (5.2) are discussed in the following. P is an arbitrary point in the measurement plane. The plane is divided into spaces S of the same size which contain a certain number N of measuring points M. P is the central point of S. PM represents the radius or the distance between P and measuring points M and $e_\perp$ is the surface normal unit vector. Θ_M represents the angle between the radius vector PM and the velocity vector U_M at the measurement point M. In the vortex centers Γ_1 reaches the value 1. In practice, values are used around 0.9 for the identification of a vortex center. The smaller this limit is set, the more turbulent, small vortices are identified.

The vortex cores are identified with the $\Gamma 2$ method (Equation (5.3)). This method is similar to the $\Gamma 1$ method. In addition, with this method the S averaged velocity over the surface is subtracted from the velocity at the measuring point U_M. Thus, the effect of convective speeds is eliminated.

$$\Gamma_2(P) = \frac{1}{N} \sum_S \frac{[PM \wedge (U_M - \bar{U}_P)] \cdot e_\perp}{\parallel PM \parallel \cdot \parallel U_M - \bar{U}_P \parallel} \tag{5.3}$$

Based on the vortex center identification algorithm Γ_1 the wall-normal and spanwise position of the vortices are analyzed for the two applied voltages $V = 5$kV and $V = 5.5$kV.

In Figure 5.20 the wall-normal positions are shown in their streamwise development. The wall-normal distance is increased until the end of the upper electrode at the normalized streamwise distance $x/L = 1$. Farther downstream the increase of the wall-normal distance is slightly reduced.

In Figure 5.21 the spanwise positions of a pair of vortices created by the discharge along one upper electrode are shown in normalized streamwise direction for the two applied voltages $V = 5$kV and $V = 5.5$kV. The normalized spanwise extension of the upper electrode is indicated with a gray shaded zone on the left side of the diagram. Additionally the plasma extensions for the two applied voltages $V = 5$kV and $V = 5.5$kV are indicated on both sides of the upper electrode with a light and dark purple shaded zone, respectively.

The spanwise positions remain more or less constant in streamwise direction for the two different cases. Whereas the position for the larger power level is slightly shifted outwards. This correlates well with larger plasma

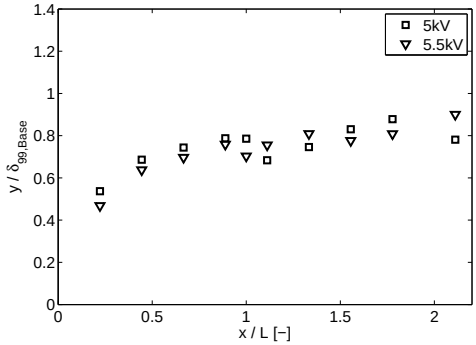

Figure 5.20: Streamwise development of the wall-normal positions of the vortex center.

extension in this case. This confirms the findings in the previous section. With a very small force the vortices are formed above the discharge region. Generated in an array of PAVGs the vortices do not experience a significant spanwise motion.

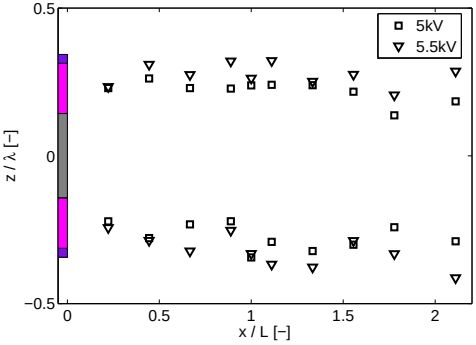

Figure 5.21: Streamwise development of the spanwise positions of the vortex center.

This clearly indicates that the spanwise distribution of the vortices is correlated on the one hand with the width of the upper electrode. Secondly the plasma extension has to be considered for the spanwise distribution.

Vorticity The circulation around the streamwise vortex, Γ normalized with the free-stream velocity and the boundary-layer thickness, was measured by integrating the streamwise vorticity over the vortex cross section, determined by vortex core identification algorithm Γ_2, according to Equation 5.4, where y_V and z_V are the coordinates inside the vortex core determined with the identification algorithm Γ_2.

$$\Gamma_{Vort} = \sum \omega_x(y_V, z_V) \cdot \Delta y \Delta z \tag{5.4}$$

The vorticity in streamwise direction, normalized with the electrode length L, is shown in Figure 5.22. The vorticity reveal a linear increase along the electrode as also identified by Jukes and Choi [70]. This also agrees well with the increase of the streak amplitude A_{st}. The difference between the investigated cases for the different power levels, are less pronounced as compared to the evolution of the streak amplitude. The maximum vorticity is reached slightly downstream of the actuator array, before the vorticity starts to decay rapidly in the further course.

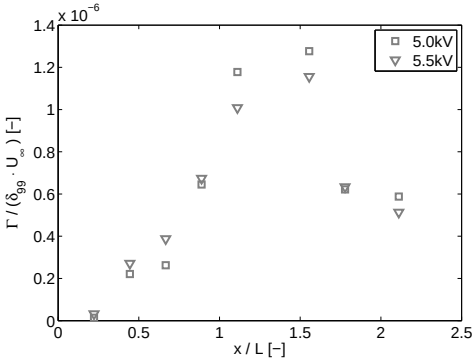

Figure 5.22: Streamwise development of the non-dimensional vortex circulation for the voltage $V = 5$kV and $V = 5.5$kV at DC=30%.

These investigations with the 3C PIV measurements provide some complementally findings to the qualitative parameter investigation in the first part of this chapter. The scaling of the streak amplitude with the consumed power per vortex pair was demonstrated. Based on the vortex identification functions it was shown that with a very small forcing the vortices are created above the discharge region and are intensified at this spanwise location, without a significant spanwise shift.

5.5 Summary of Parameter Influence on PAVG

Based on the qualitative investigation and the 3C PIV measurement the parameter influences can be summarized as follows:

Geometry: The geometry of the plasma actuator array (electrode spacing and electrode width) influence the spatial spanwise distribution of the streaks.

Power per electrode: With increasing electrode length, the generated vortices and thus the created streaks are intensified. The same could be achieved with a higher applied voltage or adjusting the duty cycle

Plasma extent: The spatial distribution of the vortices/streaks are determined by the combination of the plasma extent and the electrode width

Pulsed operation: The independent adjustment of force magnitude and spatial extent of the force with the pulsed operation offers the possibility to adjust the streak amplitude without influencing the spatial distribution.

Based on the identification of the parameter influences a plasma actuator vortex generator could be designed with an equal streak distribution as required for the boundary-layer control, as presented in the next chapter.

6 Boundary-Layer Control with Plasma Actuator Vortex Generators

In this chapter the qualification of plasma actuator vortex generators for boundary-layer control is demonstrated. The term boundary-layer control is here understood as the control of transition from laminar to turbulent flow.

The transition from laminar to turbulent is known as a stability problem. It is based on the idea that the laminar flow always experience small disturbances. For small Reynolds numbers the damping effect of viscosity ν is high enough to damp the small fluctuations. At a sufficiently large Reynolds number the damping effect of viscosity is relatively less, such that the disturbances are amplified and initiate transition to a turbulent flow state.

Dependent on the disturbance level of the oncoming flow and the character of the developing boundary layer, several transition scenarios are possible ([125]). Here the flow over a flat plate with the linear growth of two-dimensional disturbances, also known as Tollmien-Schlichting (TS) waves, is of interest. The transition process of an unaccelerated boundary-layer is schematically sketched in Figure 6.1. At the beginning of the flat plate the boundary layer is laminar and stable against disturbances, originating from roughness of the surface or small fluctuation in the oncoming flow. At a certain downstream distance (Re_{crit}) the boundary layer becomes unstable and two-dimensional disturbances are linearly amplified (primary instability) and grow in amplitude. These disturbances are also referred to as Tollmien-Schlichting waves. Above a certain amplitude the disturbances become three-dimensional and the linear growth is no longer valid (secondary instability). This is accompanied by an increase in spanwise vorticiy (cp. Figure 6.1). With a further increase of the disturbance amplitude the vortices break down and turbulent spots arise, developing into a fully turbulent boundary layer.

When the two-dimensional disturbances do not exceed a certain amplitude and have not entered the 3D state, they are damped further down-

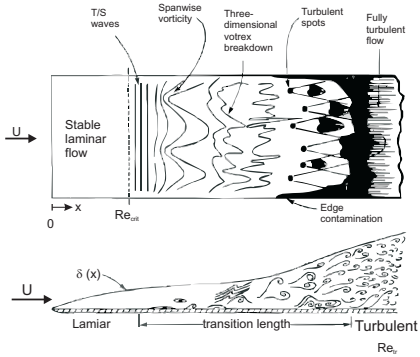

Figure 6.1: Schematic sketch of the transition process of a flat plate flow, according to White [161]

stream. The beginning of the amplification of the TS and the end of this region constitute the unstable region.

Thus the purpose of the boundary-layer control, focusing on the 2D disturbances, is to reduce the amplitude of the TS waves. Different approaches exist to reduce the amplitude of the TS waves: the stabilization of the boundary-layer profile, the active wave cancelation, or imposing of a spanwise modulation of the streamwise velocity component inside the boundary layer.

The latter control mechanism was numerically and experimentally investigated by Bakchinov *et al.* [6], Cossu and Brandt [22, 23], White *et al.* [160], Fransson *et al.* [43] and Liu *et al.* [98, 99]. With counter-rotating vortices the boundary layer is deformed, resulting in streamwise streaks of higher and lower velocity, these streaks affect the growth of the TS waves.

The transition delay in a 2D boundary-layer by the attenuation of Tollmien-Schlichtig (TS) waves was demonstrated by Fransson *et al.* [41] and Gürün and White [55].

The interaction of TS waves with the streaks was investigated experimentally and numerically. Cossu and Brandt [23] numerically demonstrated that the TS waves are modified by the presence of the streaks. They showed that the waves evolve from two-dimensional TS waves into three-dimensional varicose fundamental modes, revealing identical phase speed but lower growth rates than the TS waves. They show characteristics with a M-shaped structure in their streamwise velocity fluctuation. A physical explanation for the observed stabilization is provided by consider-

ing the kinetic energy production. The stabilizing mechanism is related to the additional turbulence production term, which turns out to be a negative contribution (Cossu and Brandt [22]) to the kinetic energy production for the most unstable waves.

Fransson *et al.* [43] demonstrated experimentally that an increase in streak amplitude was directly correlated with less growth of the TS waves.

A secondary instability analysis given by Liu *et al.* [99] of boundary layers distorted by streaks and TS waves. Two opposing effects were identified: a stabilizing effect due to a reduction in the growth rate of the primary two-dimensional TS waves, and a destabilizing effect on secondary instabilities. Liu *et al.* demonstrated, that depending on the spacing of the streaks, transition can be promoted with low streak amplitudes and delayed with higher amplitudes.

The active vortex generation by means of plasma actuator vortex generators in a laminar boundary layer is a new approach for the attenuation of TS waves, which has alreadybeen successfully demonstrated using passive elements.

6.1 TS Wave Attenuation I

Different configurations of arrays for the streak generation with PAVG are the focus of this section. In the previous chapter the possibility to energize vortices with separated and/or cascaded actuator arrays to cover a longer downstream distance was demonstrated. The first approach to generate streaks is to use four cascaded arrays. Thus the streaks are repeatedly reenergized and intensified. This approach is investigated with respect to an intensification of the attenuation and the sustained generation of the streaks. This approach is compared to the vortex generation with a single array. The interaction of artificially exited TS waves with the streak is investigated and compared for the different approaches.

The experiments were conducted in the low-speed wind tunnel facility (NWK2) of the TU Darmstadt using the flat plate as described in the previous section.

The acrylic glass plate segment, containing the exchangeable insert, was replaced with single plate to reduced roughness on the surface of the plate. The new segment had a cavity milled on the surface to flush mount the plasma actuator arrays onto the surface.

6.1.1 Experimental Setup

Four actuator arrays were cascaded in the streamwise direction between $x = 150$ and $x = 400$mm with a streamwise distance of 50mm between each array, as shown in Figure 6.2.

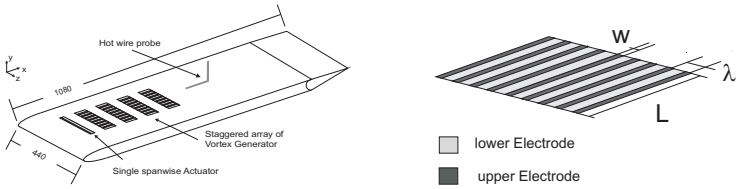

(a) flat plate (b) Actuator array

Figure 6.2: Setup of the flat plate with cascaded plasma vortex generator arrays

A single actuator-array configuration is defined as an array of plasma actuators with a large single lower electrode and nine upper electrodes with a width of $w = 2$mm each, a streamwise length of $L = 25$mm and a $\lambda = 8$mm spanwise spacing. The spacing corresponds to the local spanwise wave number of optimal disturbances $\beta = 0.45$ according to Tumin and Reshotko [150] related to the streamwise position of the upstream edge of the first array. The plasma actuator arrays were made of Cirlex and self-adhesive copper tape. The copper tape and the dielectric layer have thicknesses of 35μm and 300μm respectively. Upstream of the array a single spanwise actuator was placed at $x = 100$mm, serving as a disturbance source for exciting TS waves of 100Hz frequency.

The velocity data were acquired using Laser Doppler Velocimetry (LDV) (*Dantec FlowExplorer*). The measurement positions were downstream and in-between the plasma actuator arrays. In the case of phase-averaged measurements $60k$ samples were acquired per measurement position and sorted into 60 bins per cycle. For non-phase locked measurements 20k samples were acquired per measurement position.

6.1.2 Base Flow

The free-stream velocity was chosen to $U_\infty = 8\frac{\mathrm{m}}{\mathrm{s}}$ for all experiments. The normalized boundary-layer profilesu/U_∞ at the wall-normal position $\eta = y/\delta(x)$ normalized with the Blasius length scale $\delta(x) = \sqrt{(\nu x)/U}$ are shown

for different streamwise positions in comparison to the theoretical Blasius solution in Figure 6.3(a).

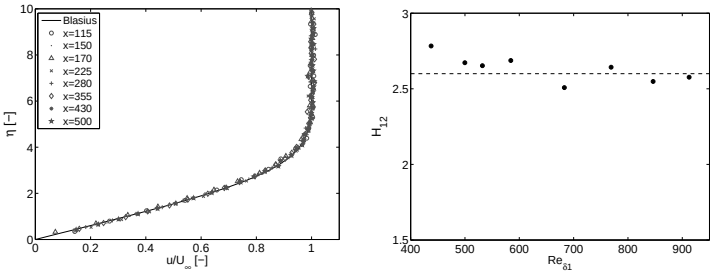

(a) Normalized boundary-layer profiles between $x = 115$ and 500mm

(b) Shape factor H_{12} in streamwise direction

Figure 6.3: Base flow characteristics

The corresponding streamwise evolution of the shape factor H_{12} is shown in Figure 6.3(b). The theoretical shape factor of $H_{12} = 2.58$ is depicted as a dotted line. The measured data revealing a good agreement with the theoretical solution. Considering the normalized boundary-layer profiles and the streamwise evolution of the shape factor, an almost unaccelerated flow can be assumed.

6.1.3 Steak Generation

When operating only the first actuator array, the downstream evolution of the streaks behaves comparable to conventionally created streaks (White[159], Fransson *et al.* [42]) with passive vane type vortex generators. After the initiation of the vortices within the electrode length of $L = 25$mm, the streak amplitude still grows a bit downstream of the actuator before it starts to decay due to diffusion.

In contrast to this, the streamwise development of the streak amplitude with all four arrays operated differs significantly. The comparison of the streamwise development of the normalized streak amplitude for both cases, one array and all four arrays, is shown in Figure 6.4, where the positions of the single actuator arrays are shaded in gray. For the latter case the evolution of the streak amplitude shows an almost linear increase in streamwise direction.

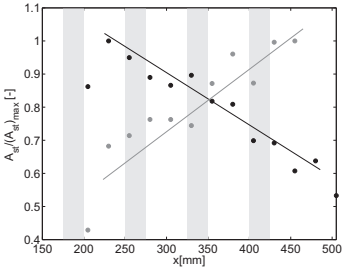

Figure 6.4: Streamwise development of $A_{st}/(A_{st})_{max}$; Black - one actuator array, grey - four actuators arrays: shaded zones indicate downstream position of actuators

When the four cascaded arrays are operated with different parameters, such as increasing the power consumption by increasing the applied voltages or the duty cycle, the maximum streak amplitude A_{st} increases, as shown in Figure 6.5. The different operating conditions reveal an almost linear increase of the streak amplitude across the cascaded arrays in the streamwise direction. Thus, the single and the cascaded arrays behave

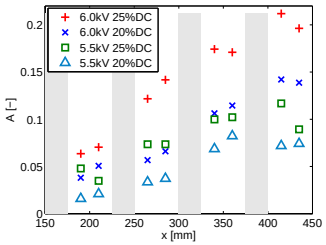

Figure 6.5: Streamwise development of A_{st} with four actuators arrays and different operating conditions: shaded zones indicate downstream position of actuators

similar. The maximum induced streak amplitude increases with increasing power consumption.

6.1.4 Disturbance Source

The single spanwise actuator, subsequently referred to as the disturbance source, was operated at very low voltages and in pulsed mode at a modulation frequency of $f_{mod} = 100$Hz and a duty cycle of 50% to excite TS waves.

The measured phase-angle dependent velocity fluctuation $\widehat{u}_\phi(\eta) = \overline{U_\phi} - \overline{U}$ of the TS waves, shown in Figure 6.7(a), was calculated by subtracting the phase-averaged velocity $\overline{U_\phi}$ from the time averaged velocity $\overline{U}$.

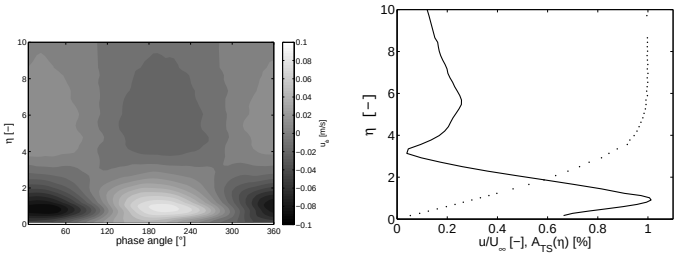

(a) Phase position of $\widehat{u}_\phi$

(b) TS wave amplitude distribution ($A_{TS}(\eta)$) and boundary-layer profile

Figure 6.6: TS waves at $x = 500$mm or $Re_{\delta_1} = 920$

The normalized TS wave amplitude distribution $A_{TS}(\eta) = \mid max(\widehat{u}_\phi) - min(\widehat{u}_\phi) \mid_\eta / (2 \cdot U_\infty)$ is shown for the base line case in Figure 6.7(b). The operating power of the disturbance source was adjusted to achieve a TS wave amplitude A_{TS} of approximately 1% free-stream velocity at $x = 500$mm.

The streamwise development of the TS wave amplitude A_{TS} is shown in Figure 6.7. The amplitude decreases after the excitation until $x = 150$mm ($Re_{\delta_1} = 530$) before it is amplified. Comparing this to the stability features of a Blasius profile (e.g. Schlichting [137]), shows that this location is close to Branch I of the stability curve for the TS wave frequency of $f_{mod} = 100$Hz, corresponding to a disturbance frequency of $\beta_r \cdot \delta_1 / U_\infty = 0.073$ or a reduced frequency of $F = 2\pi f \nu / U_\infty^2 = 136 \cdot 10^6$.

6.1.5 Interaction of TS Waves and Streaks

The artificially excited TS waves interact with the streaks generated by the plasma actuator arrays. At the position of the first plasma actuator array

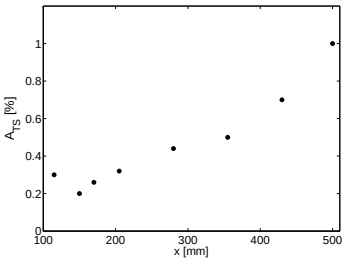

Figure 6.7: Development of TS wave amplitude in the streamwise direction

the TS waves have an amplitude A_{TS} of approximately 0.25%.

To evaluate the interaction of the TS waves with the streaks, their amplitude was calculated according to Equation (6.1) as suggested in Fransson *et al.* [41].

$$A_{TS}^{y} = \int_{\eta=0}^{\eta=8} A_{TS} d\eta \tag{6.1}$$

In order to provide a single value for the TS wave amplitude in the streaky boundary layer, A_{TS}^{yz} is calculated by averaging the amplitudes measured in the spanwise centers of the high-speed streak and low-speed streak.

Four Arrays For the four arrays Figure 6.8 shows the phase averaged velocity fluctuation amplitude A_{TS} measured in the low-speed streak (blue line) and high-speed streak (red line) at $x = 500$mm compared to the base configuration (black line). The corresponding normalized boundary-layer profiles are included.

Figure 6.8(a) and 6.8(b) show the interaction of the TS waves with the streaks of different amplitudes A_{ST}. In Figure 6.8(a) all four PAVG were operated at $V = 4.9$kV and $DC = 20\%$ with a corresponding power consumption of $P = 0.58$W per vortex pair. A streak amplitude of $A_{ST} = 6\%$ at $x = 500$mm was the result. A streak amplitude of $A_{ST} = 13.5\%$ results from slightly modified operation parameters: $V = 5.1$kV at $DC = 20\%$ with a corresponding power consumption of $P = 0.64$W per vortex pair (Figure 6.8(b)). In both cases (4.9 and 5.1kV) an amplification of the TS wave inside the low speed streak could be observed. Whereas an attenuation of A_{TS} in the high speed streak can be identified. For the higher streak amplitude the wave attenuation inside the high speed streak and the

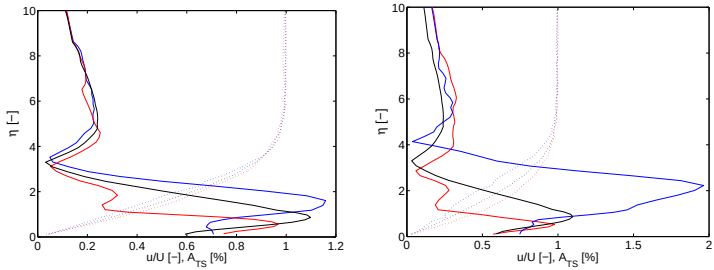

(a) 4.9kV, 20% DC, $P = 0.58$W per vortex (b) 5.1kV, 20% DC, $P = 0.64$W per vortex

Figure 6.8: Boundary-layer profiles (dotted lines) and TS waves (solid lines) in low-speed streak (blue) and high-speed streak (red) compared to the case without actuation (black)

amplification in the low speed streak are stronger. With stronger forcing than with a voltage of 5.1kV the transition location moves upstream of the last measurement position.

Instead of the desired amplitude reduction, the TS wave amplitude A_{TS}^{yz} experiences an amplification of 8% and 36% for the $V = 4.9$ and the 5.1kV cases respectively.

One Array The results on the interaction between streaks and TS waves, with only the first array operated, are presented in Figure 6.9. In Figure 6.9(a) a TS wave attenuation in both, the high and low speed streak can be observed for the operation conditions $V = 4.9$kV and $DC = 40\%$ with a power consumption of $P = 0.81$W per vortex pair and a resulting streak amplitude at $x = 500$mm of $A_{st} = 4\%$. In this case the amplitude A_{TS}^{yz} is damped by 27%. For the case shown in Figure 6.9(a) and 6.9(b), the attenuation in high and low speed streak is even more pronounced in Figure 6.9(b). In this case a higher operating voltage ($V = 5.1$kV, $P = 0.95$W per vortex pair) was applied, resulting in a higher streak amplitude. The damping rate in this case ($V = 5.1$kV) is around 53% for a streak amplitude at $x = 500$mm of $A_{st} = 5\%$.

Again the effect becomes stronger with increasing streak amplitude.

An explanation for the amplification of the TS wave with the four array configuration can be derived from the secondary instability analysis given by Liu *et al.* [99] of boundary layers distorted by streaks and TS waves. Liu

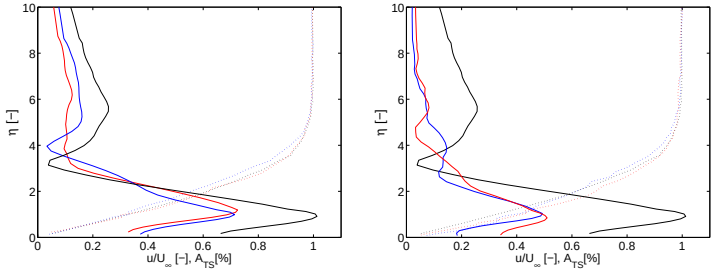

(a) 4.9kV, 40% DC, $P = 0.81$W per vortex

(b) 5.1kV, 40% DC, $P = 0.95$W per vortex

Figure 6.9: Boundary-layer profiles (dotted lines) and TS waves (solid lines) in low-speed streak (blue) and high-speed streak (red) compared to the case without actuation (black)

et al. demonstrated transition can be promoted with low streak amplitudes and delayed with higher amplitudes.

6.1.6 Summary

The active and sustained vortex generation in a laminar boundary layer using spanwise acting plasma actuators was presented. Using four cascaded arrays, streaks were repeatedly reenergized and intensified. This approach is compared to the vortex generation with a single array. The streamwise development of the streak amplitude of the case with four arrays demonstrates the possibility of actively creating and reenergizing streamwise streaks in a laminar boundary layer. Tollmien-Schlichting waves of 1% amplitude were excited artificially with a single streamwise forcing plasma actuator. The interaction of the TS waves with the generated streaks reveals that an amplification and/or damping of the TS waves, depending on the approach for the streak generation and their streamwise development, is possible. It is shown that all effects scale with the forcing magnitude of the plasma actuator. With a single array a damping rate of up to 53% could be achieved.

6.2 TS Wave Attenuation II

Additional measurements investigating the attenuation of TS waves by means of PAVGs were performed.

6.2.1 Experimental Setup

The experiments were conducted at the BL tunnel (BLT) at the Royal Institute of Technology (KTH) in Stockholm. The BLT is a closed-loop, closed-test-section, low-speed and temperature controlled wind tunnel, which includes a 4.2m long test section with a cross-sectional area of $0.5 \times 0.75\text{m}^2$ at its upstream end. The maximum speed with empty test section is 48m/s, and the contraction has an area ratio of CR=9. The turbulence intensity in the test section was evaluated to be less than $< 0.04\%$. Further details on the flow quality can be found in Lindgren and Johansson [93].

The vertically arranged flat plate, made out of $20mm$ thick acrylic-glass, spanned the height of the test section with 750mm. The tip of the leading edge was located 85mm downstream from the outlet of the contraction section. The total length of the plate was 3915mm, including the trailing edge flap with a length of 580mm in streamwise direction. The flap was inclined with an angle of 6.9° to adjust the position of the stagnation point at the leading edge. The leading edge with a super-elliptic profile had a semi-major axis of 200mm.

The disturbance slot was positioned 135mm downstream of the leading-edge. With an extension of 270mm in the z-direction the disturbance slot spanned more than one third in width of the flat plate. The 0.6mm wide disturbance slot was connected via 36 tubes (1.2m in length) to a loud-speaker.

The flat plate consisted of exchangeable segments between the positions $x = 225$mm and $x = 950$mm. They carry the inserts with the plasma actuator arrays, as depicted in Figure 6.10. The exchangeable segments with the plasma actuator arrays could be replaced with segments made of acrylic-glass of different sizes. Thus the position of the plasma actuator arrays could be chosen arbitrarily.

The exchangeable segments with the plasma actuator arrays, were made of aluminum. Resin inserts with pockets were used to flush mount the plasma actuators to the segments and to ensure electrical insulation to the aluminum part as shown in Figure 6.11. Wires for the high voltage and the grounding were connected from the bottom side to ensure a smooth surface on the upper side of the experimental setup.

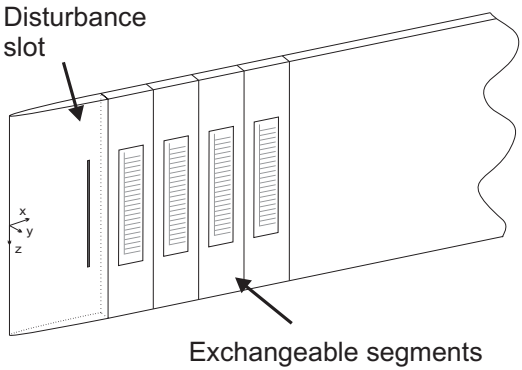

Figure 6.10: Schematic sketch of the experimental setup at KTH

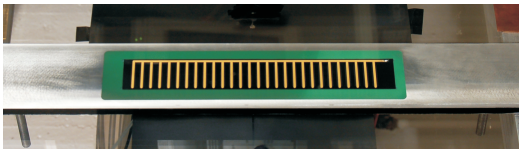

Figure 6.11: Photograph of an exchangeable segment with the resin inserts and mounted plasma actuator array.

A single actuator-array configuration with one spanwise array of plasma actuators with a large single lower electrode and 28 upper electrodes of $w = 2$mm width each, a streamwise length of $L = 25$mm and with a $\lambda = 8$mm spanwise spacing.

The plasma actuator arrays were made of Cirlex with a thickness of $d = 0.3$mm and $17\mu m$ thick copper electrodes fabricated by etching. For the masking material a photo resist was used which has been patterned by photolithography. After the etching process the electrodes were coated with a $6\mu m$ thick layer of tin and gold, to prevent the electrodes from corroding. Two different actuator configurations were investigated. The first configuration was a single actuator array placed at $x = 350$mm related to the electrode's trailing edge. The spacing corresponds to the local spanwise wave number of $\beta = 0.6$ according to Tumin and Reshotko [150] related to the streamwise position of the upstream edge of the first array. This represents narrower streaks at this location, which are beneficial for the attenuation of TS waves according to the findings of liu *et al.* [99].

The second configuration consists of four cascaded arrays with a streamwise distance of $\Delta x = 50$mm, with the first array located at the same position as compared to the single array configuration. All measurements were conducted at a free-stream velocity of $U_\infty = 8$m/s and a controlled temperature of $T = 18°$C.

The velocity was acquired using a commercial high-speed PIV system comprising a *New Wave Pegasus-PIV* diode-pumped Nd:YLF laser system, which offers 10mJ of $\lambda = 527$nm light at 1000Hz, and a *FASTCAM SA5* high-resolution camera (12 bit, maximum resolution 1024×1024 pixels) with a *Nikon 200mm f/4 Macro* lens. The flow was seeded with Di-Ethyl-Hexyl-Sebacat (DEHS) aerosol.

Two different PIV camera configurations were used during these measurements. The first configuration comprises one camera positioned underneath the test section and the laser sheet orientated in the wall-normal x,y-direction as shown in Figure 6.17. These 2D measurements yield the velocity information of the two in-plane velocity components (2C). With a reduced images size of 1024×512 pixels a field of view of 30×15mm in streamwise and wall-normal direction were captured. The second configuration comprises two cameras facing the wall-normal y,z-plane, illuminated with the laser located underneath the test section. To assure the largest possible traversing distance in streamwise direction, the cameras were tolted around two axes towards the measurement plane. A double Scheimpflug configuration was used to adjust the focal plane. With a distance of 800mm between the cameras and the measurement plane and the resulting overlap of the images, a field of view of 35×30mm in spanwise and wall-normal direction was achieved. Theses measurements yield the velocity information of all three velocity components (3C) in the 2D measurement plane. With both camera configurations the laser was operated in the double frame mode with a repetition rate of 840Hz and a time between the laser pulses of $\Delta t = 40\mu s$ and $\Delta t = 50\mu s$ with a total number of images of $N = 5040$ and $N = 10080$ for the 2C and 3C measurements, respectively. The velocity distributions were calculated from the raw data using commercial software (LaVision). To reduce the signal-to-noise ratio (SNR) in the images, the image mean was subtracted from the raw images. The PIV processing with the 2C measurements an adaptive correlation was applied with 3 refinement steps and interrogation areas (IAs) with a final/initial size of $8 \times 8/64 \times 64$ and pixels. The overlap for the IAs was set to 50% for all three refinement steps. Outliers were detected with an RMS based filter

6.2.2 Base Flow

The streamwise development of the undisturbed base flow is analyzed with the 2C measurements at 11 positions between $x = 200$ and 1150mm. The normalized boundary-layer profiles u/U_∞ at the wall-normal position $\eta = y/\delta(w)$, which were normalized with the Blasius length scale $\delta(x) = \sqrt{(\nu x)/U}$ in comparison to the theoretical Blasius solution, are shown in Figure 6.12. The streamwise evolution of the shape factor H_{12} is shown in Figure 6.13.

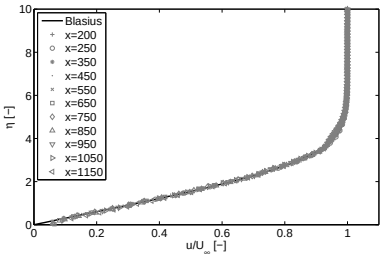

Figure 6.12: Normalized boundary-layer profiles between $x = 200$ and 1150mm.

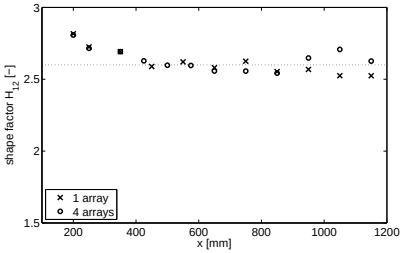

Figure 6.13: Shape factor H_{12} in streamwise direction.

The shape factor (H_{12}) is presented for the two different actuator configurations, since the setup slightly changed due to the different number of exchangeable segments. The junctions between the segments were adjusted to be in the order of less than 0.1mm in roughness. As can be seen in Figure 6.13 the shape factor H_{12} shows good agreement for both configurations

with each other and with the theoretical solution for a unacceleated boundary layer. Only further downstream ($x > 950$mm) do the curves diverge slightly.

6.2.3 Disturbance Source

The TS waves were excited at a frequency of 70Hz. The amplitude was adjusted such that the boundary layer does not reach a turbulent state, at the position of a stationary CTA probe inside the boundary layer at $x = 1250$mm. With a repetition rate of the laser pulses 12 times higher than the disturbance frequency, a phase-averaged analysis of the disturbance, dividing the period into 12 bins, is possible.

The velocity fluctuation $u_\phi(x) = \overline{U_\phi(x)} - \overline{U(x)}$ at the measurement position $x_p = 950$mm is shown in Figure 6.14 for one phase position. The streamwise position $x' = x - x_p$ is related to the measurement position x_p.

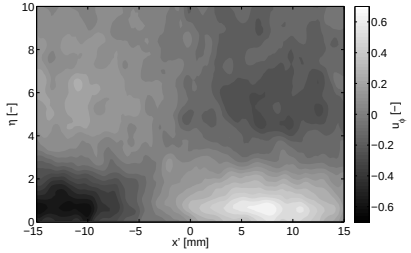

Figure 6.14: Velocity fluctuation $u_\phi(x)$ at the measurement position $x_p = 950$mm.

It can be seen in Figure 6.14, that the FOV of the PIV measurement captures less than one wavelength of the excited TS wave.

The amplitude $A_{TS}(\eta)$ of the disturbance was determined according to the definition in Section 6.1.4 and is shown in Figure 6.15 (solid line). The corresponding boundary-layer profile is plotted with a dotted line.

The maximum of the TS waves ($A_{TS}(\eta)$) at several streamwise measurement positions yielding the evolution and the growth of the disturbances as shown in Figure 6.16.

The amplitude saturates after the excitation until $x = 350$mm, before it is amplified until $x = 1050$mm. Further downstream it starts to decrease. Comparing this to the stability features of a Blasius profile (e.g. Schlichting

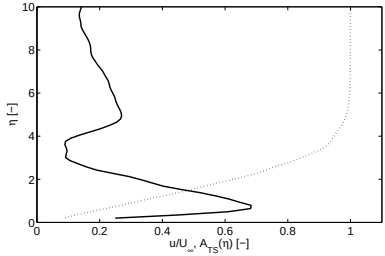

Figure 6.15: TS wave $A_{TS}(\eta)$ at the measurement position $x_p = 950$mm.

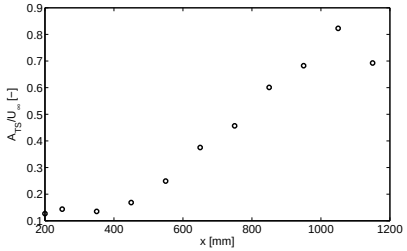

Figure 6.16: Streamwise evolution of the exited TS waves.

[137]), with a reduced frequency of $F = 2\pi f\nu/U_\infty^2 = 94 \cdot 10^6$, shows that $x = 350$mm is close to Branch I of the stability curve for the TS wave frequency of $f_{TS} = 70$Hz and $x = 1050$mm is close to Branch II.

6.2.4 Results 2C Measurements

To evaluate the influence of streaks on the TS waves the 2C measurements were performed at two spanwise positions: $z = 0$mm and $z = 4$mm. The first spanwise position started between two upper electrodes at the location of a low-speed streak ($z = 0$mm) and traversed downstream between $x = 350$ and $x = 1150$mm. The second spanwise position ($z = 4$mm) started downstream of an upper electrode at the spanwise location of a high-speed streak.

One Array The initial streak amplitude at x=350mm downstream of the actuator array was determined to be 16.5% of the free-stream velocity.

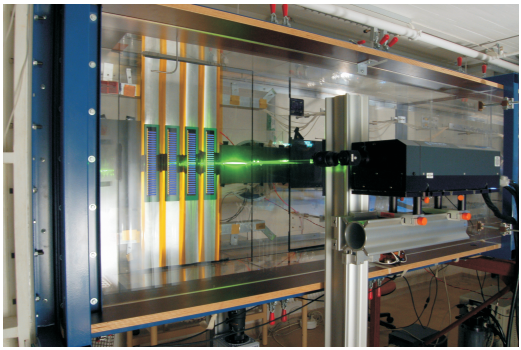

Figure 6.17: Photograph of the experimental setup with the 2C PIV camera configuration and the four cascaded arrays.

The actuator was operated at an applied voltage of $V = 4.6$kV and at an operating frequency of $f = 10$kHz, modulated with $f_{mod} = 500$Hz and a duty cycle of DC= 30%. The average power consumption of the actuator was in total $P_A = 4.9$W with a corresponding power consumption of $P = 0.175$W per vortex pair.

In Figure 6.18 the TS waves at two downstream measurement positions ($x_p = 750$ and $x_p = 1150$mm) are shown for the base flow (black lines) and at the two spanwise positions. The measurements at the spanwise position of the high-speed streak are shown with red curves, whereas the measurement of the spanwise position of the low-speed streak is represented in blue.

At the measurement position $x_p = 750$mm only a small influence on the TS wave can be seen in Figure 6.18(a). The effect is more visible within the high-speed streak. Further downstream at $x_p = 1150$mm (cp. Figure 6.18(b)) the influence of the streaks on the TS waves is more pronounced. Here the TS waves yield the typical M-shaped character of the velocity fluctuations of the streaky TS waves([23]).

To evaluate the interaction of the TS waves with the streaks, their amplitude was calculated according to Equation (6.1). In order to provide a single value for the TS wave amplitude in the streaky boundary layer, A_{TS}^{yz} is calculated by averaging the amplitudes measured in the centers of the high-speed streak and low-speed streak.

For a better comparison of the interaction, the ratio of the undisturbed TS waves and the TS waves of the streaks at several streamwise positions

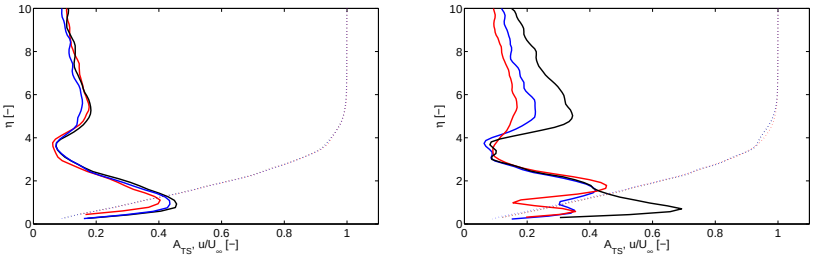

(a) $x_p = 750$mm (b) $x_p = 1150$mm

Figure 6.18: Boundary-layer profiles (dotted lines) and TS waves (solid lines) in low-speed streak (blue) and high-speed streak (red) compared to the case without actuation (black) at the measurement positions $x_p = 750$mm and $x_p = 1150$mm

are shown in Figure 6.19 with the damping factor. With the definition of the damping factor $DF = (A^{yz}_{TS,PAVG}/A^{y}_{TS,base}) - 1$, values of $DF > 0$ give an amplification of the TS waves, whereas values of $DF < 0$ indicate an attenuation.

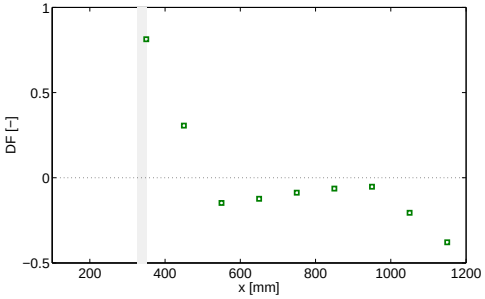

Figure 6.19: Downstream evolution of the damping factor $DF = (A^{yz}_{TS,PAVG}/A^{y}_{TS,base}) - 1$ for the one array configuration

The steamwise position of the single actuator array is indicated with a shaded gray zone in Figure 6.19. At the first two measurement positions downstream of the actuator array, an amplification of the mean TS wave

amplitude A_{TS}^{yz} can be seen. This is related to an amplification within the low-speed streak, whereas the damping in the high-speed streak is less pronounced. Further downstream ($x_p > 550$mm) the TS waves are reduced in amplitude in both the high and low-speed streaks resulting in a negative damping factor. This initial growth was also observed by Shahinfar *et al.* [140]. They assume a correlation between the maximum TS wave amplitude with the streamwise location of the maximum streak amplitude.

Four Arrays For the configuration with the cascaded arrays, the actuator arrays were operated at lower power levels than in the previous case. The actuator was operated at a voltage of $V = 4.2$kV and an operating frequency of $f = 10$kHz, modulated with $f_{mod} = 500$Hz and a duty cycle of DC= 20%. The average power consumption of the actuator was in total $P_A = 14.5$W with a corresponding power consumption of $P = 0.52$W per vortex pair.

In Figure 6.20 the TS waves at two downstream measurement positions ($x_p = 575$ and $x_p = 650$mm) are shown, comparing the base flow configuration (black line) with the TS waves measured inside the high-speed and low speed streak (red and blue lines, respectively). At the first measurement position $x_p = 575$mm right downstream of the last actuator array a strong amplification of the TS wave in the low-speed streak can be seen in Figure 6.20(a), in comparison to this the TS wave inside the high-speed streak is reduced in its magnitude. Further downstream at $x_p = 650$mm, shown in Figure 6.20(b), the TS wave in the low-speed streak is reduced in its magnitude again whereas the TS wave in the high-speed streak is amplified.

In Figure 6.21 the comparison of the streamwise evolution of the TS waves for the base flow with the TS waves in the high-speed and low-speed streak is shown. After the first array the TS wave amplitude A_{TS} is slightly amplified within the low-speed streak. With every additional array the TS wave in the low-speed streak grows in amplitude. Downstream of the last array at $x_p = 575$mm the amplification within the low-speed streak is strongly increased and the TS wave reaches an amplitude of 1.45% of the free-stream velocity. The initial growth of the TS wave as observed with the single array configuration. With the cascaded arrays this initial growth is repeated with every additional array. This growth of the TS wave is accompanied by an almost linear increase of the streak amplitude across the cascaded arrays. This agrees well with the assumption that the maximum TS wave amplitude is correlated with the streamwise location of the streak amplitude

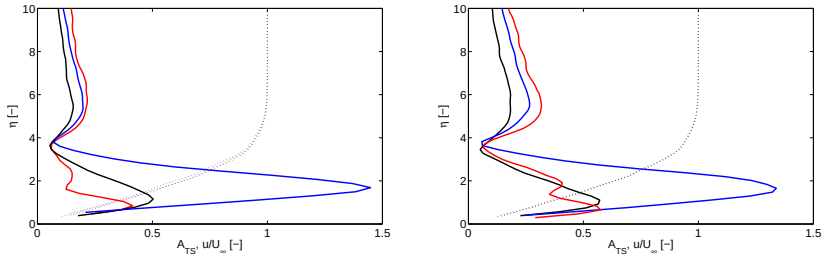

(a) $x_p = 575$mm (b) $x_p = 650$mm

Figure 6.20: Boundary-layer profiles (dotted lines) and TS waves (solid lines) in low-speed streak (blue) and high-speed streak (red) compared to the case without actuation (black) at the measurement positions $x_p = 575$mm and $x_p = 650$mm

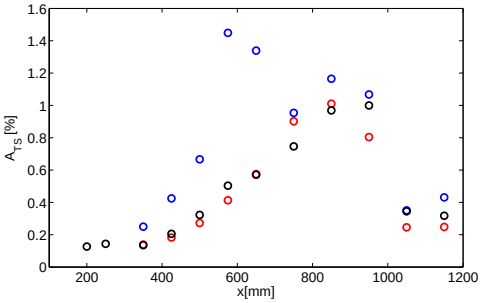

Figure 6.21: Comparison of the streamwise evolution of the TS waves for the base flow (○) with the TS waves of the high-speed (○) and low-speed streak(○).

In contrast to this, the TS waves in the high-speed streak seem less affected in its amplitude, but as seen in Figure 6.20(a) the TS waves are strongly influenced in its shape. This results in a reduction of the amplitude $A^y_{TS,PAVG}$.

This can also be seen in the downstream evolution of the damping factor shown in Figure 6.22. The damping factor after the first actuator arrays reveal a small positive value, smaller as compared to the amplification as

can be seen with the single array configuration, associated with the lower streak amplitude after the first array. With the second and third additional actuator array the damping factor is reduced, due to the averaged influence of increased reduction of the TS wave amplitude in the high-speed streak and the amplification within the low-speed streak. Downstream of the last array at $x_p = 575$mm the damping factor is strongly increases due to the strong increase of the TS wave in the low-speed streak. No further compensation by an attenuation of the TS wave amplitude in the high-speed streak can be seen.

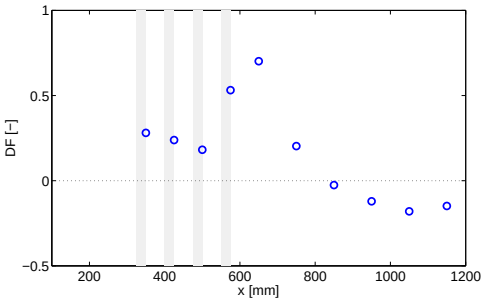

Figure 6.22: Downstream evolution of the damping factor ($DF = (A^{yz}_{TS,PAVG}/A^{y}_{TS,base}) - 1$) for the four array configuration

The damping factor reaches a maximum at $x_p = 650$mm and further downstream the damping factor decreases. As mentioned before, the TS wave reaches an amplitude of 1.45% of the free-stream velocity at $x_p = 575$mm. Amplitudes larger than 1% of the free-stream velocity are usually referred to disturbances that exceed the linear stability regime. The streamwise velocity fluctuation does not reveal the typical eigenform of the TS wave as can be seen in Figure 6.23. The velocity fluctuation $u_\phi(x)$ is shown for one phase position at $x_p = 1150$mm for the unmodulated base flow (Figure 6.23(a)) and the measurement in the low-speed streak at this streamwise position (Figure 6.23(b)). The velocity fluctuation $u_\phi(x)$ in Figure 6.23(a) shows the typical features of TS waves including a phase shift close to the boundary-layer edge ($\eta = 3$). In contrast to this, the velocity fluctuation $u_\phi(x)$ in Figure 6.23(b) dose not reveal these features. The wall-normal extension of the fluctuation is reduced and a second maximum with a phase shift is not visible. Regions with positive and negative

component of the fluctuation are not arranged next to each other, they are surprisingly small and imbricating each other.

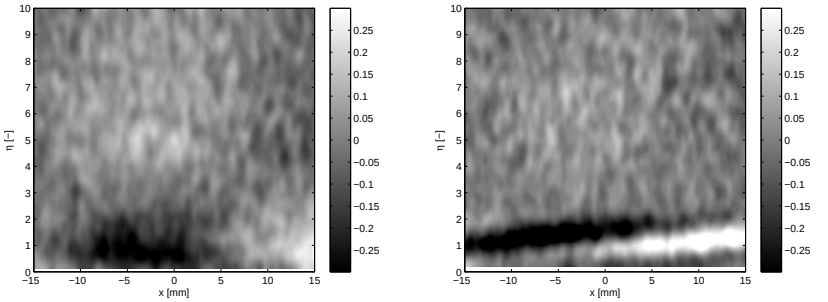

(a) Base flow (b) Low-speed streak

Figure 6.23: Comparison of the velocity fluctuation $u_\phi(x)$ at the measurement position $x_p = 1150$mm for the base flow (a) and the measurement within the low-speed streak at $x_p = 1150$mm (b).

The results obtained by the measurements at KTH are in good agreement with the preliminary investigations performed in the low-speed wind tunnel facility (NWK2) at the TU Darmstadt.

With the measurement of the streamwise evolution more detailed insights of the interaction of the TS waves and the streaks, created with single and cascaded plasma actuator vortex generators, could be obtained.

With the single array configuration an initial growth of the TS waves is observed in the low-speed streak. This agrees well with the findings of the TS wave attenuation by passive VGs ([140]). Farther downstream TS waves are reduced in amplitude in both the high-speed and low-speed streaks resulting in a negative damping factor. This initial growth occurs repeatedly with the four cascaded arrays. This amplification seems to be related to the growth of the streak amplitude. With this configuration the TS wave amplitude exceed an amplitude where the linear growth of the TS waves is not valid anymore. Father downstream at the last measurement position, the streamwise velocity fluctuation does not reveal the typical eigenform of the TS wave.

6.2.5 Results 3C Measurements

The 3C PIV measurements reveal the benefit of simultaneous measurements of spanwise modulation and velocity fluctuation.

Using the 3C measurements configuration the interaction of the exited TS waves and the streaks created with one actuator array was investigated. A photograph of the experimental setup is shown in Figure 6.24.

The actuator array was operated at a slightly lower power consumption, as compared to the 2C measurements configuration. The actuator was operated at a voltage of $V = 4.2$kV and at an operating frequency of $f = 10$kHz, modulated with $f_{mod} = 500$Hz and a duty cycle of DC= 30%. The average power consumption of the actuator was in total $P_A = 2.96$W with a corresponding power consumption of $P = 0.11$W per vortex pair.

The 3C measurements were performed first in the chronological order, thus the lower power consumption with the 3C measurements originate from the careful treatment of the equipment during the first measurements.

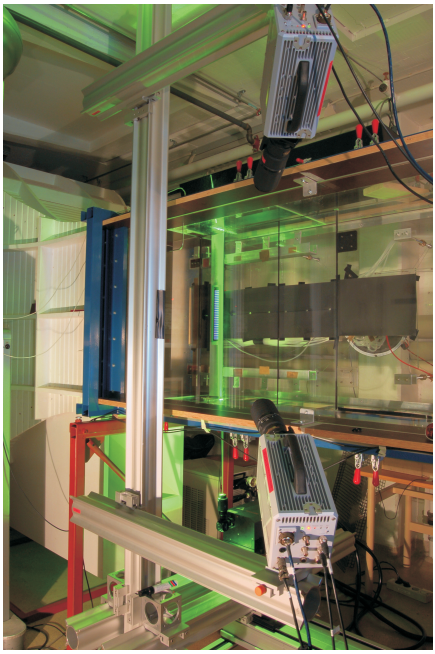

Figure 6.24: Photograph of the experimental setup with the 3C PIV camera configuration and one plasma actuator arrays.

Another benefit of the 3C measurements in the y,z-plane is the more exact evaluation of the streak amplitude in comparison with the 2C measurements in the x,y-plane. Since the 2C measurements compares single experiments, obtained at the spanwise position of the high-speed and low-speed streak small variations in the determination of the wall normal distance lead to a falsely determined velocity difference. Thus smaller streak amplitudes further downstream are resolvable with the 3C measurements. The maximum streak amplitude is 4.23% of the free-stream velocity with the present operating condition. This is significantly smaller than with the larger applied voltage as presented for the single array configuration in Section 6.2.4. The streamwise evolution of the streak amplitude downstream of the actuator array is shown in Figure 6.25.

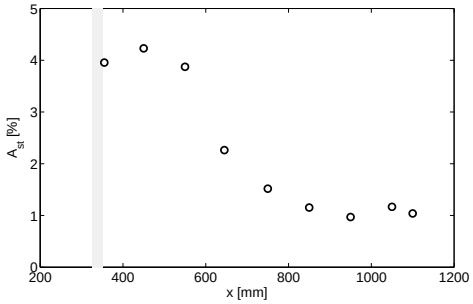

Figure 6.25: Downstream development of the streak amplitude A_{st} .

It can be seen, that downstream of the actuator array the streak amplitude is still increasing, before it starts to decay. This is in good agreement with the measurements obtained at the low-speed wind tunnel facility (NWK2) at the TU Darmstadt with one actuator array.

In addition to the spanwise modulation of the boundary layer, the phase-averaged velocity fluctuation $\widehat{u_\phi}$ and $\widehat{v_\phi}$ (in streamwise and wall normal direction respectivly) can be calculated from these measurements. To reduce the noise, the phase-averaged velocity fluctuation is spanwise averaged in spanwise direction along the whole FOV with the number (B_z) of calculated velocity profiles for the PIV data processing:

$$u_\phi^z(\eta) = \frac{1}{B_z}\sum_{z=1}^{B_z}\widehat{u_\phi}(\eta, z), v_\phi^z(\eta) = \frac{1}{B_z}\sum_{z=1}^{B_z}\widehat{v_\phi}(\eta, z). \tag{6.2}$$

The phase-averaged velocity fluctuations in streamwise (u_ϕ^z) and wall-normal (v_ϕ^z) direction at a streamwise position of $x = 850$mm are shown in Figure 6.26.

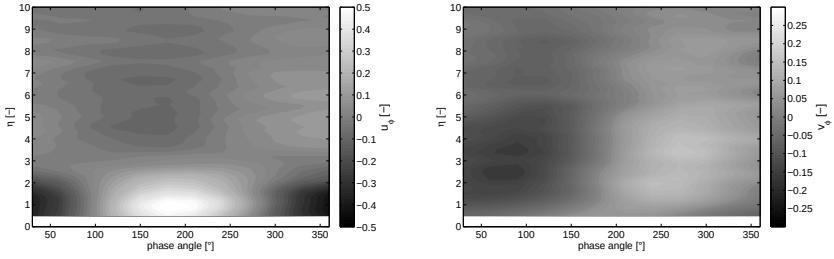

(a) u_ϕ^z (b) v_ϕ^z

Figure 6.26: Velocity fluctuation u_ϕ and u_ϕ at the measurement position $x = 850$mm.

The normalized TS wave amplitude distribution $A_{TS}^z(\eta) = \mid max(\widehat{u^z}_\phi) - min(\widehat{u^z}_\phi) \mid_\eta / (2 \cdot U_\infty)$ is evaluated at several streamwise measurement positions. In Figure 6.27 the TS wave amplitude distribution ($A_{TS}^z(\eta)$) is shown for the streamwise position $x = 850$mm. It can be seen that the distribution is more noisy compared to the 2C measurements.

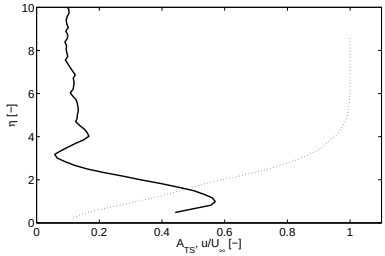

Figure 6.27: TS wave amplitude distribution ($A_{TS}^z(\eta)$) and boundary-layer profile.

The streamwise development of the maximum TS wave amplitude is shown in Figure 6.28 revealing a stronger uncertainty in the determined maximum TS wave amplitude as compared to the data obtained with the

2C measurements.

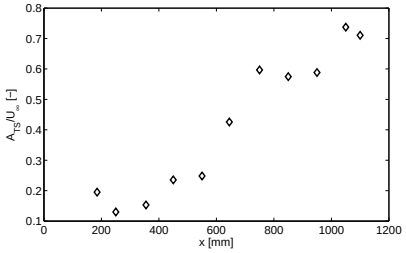

Figure 6.28: Development of maximum TS wave amplitude in the streamwise direction.

However, the growth of the TS waves is in general good agreement with the 2C measurements. Since the data is noisy (cp. Figure 6.27) the damping factor $DF_{3C} = (max(A^z_{TS,PAVG})/max(A^z_{TS,base})) - 1$ is evaluated with the maximum value of the spanwise averaged TS wave amplitude $A^z_{TS}(\eta)$. The development of the damping factor DF_{3C} is shown in Figure 6.29.

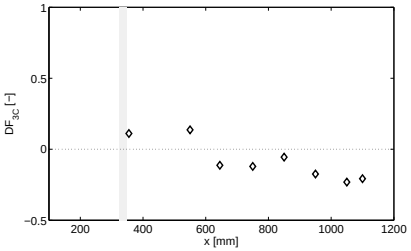

Figure 6.29: Downstream evolution of the damping factor (DF_{3C}) for the one array configuration with the 3C measurements.

Even though the damping factor DF_{3C} obtained with the 3C measurements is not directly quantitatively comparable with the damping factor DF of the 2C measurements from the previous section, it reveals the same tendencies. The TS waves are amplified just downstream of the actuator array. Further downstream they develop with a reduced growth.

6.2.6 Summary

In this section 2C PIV measurements in the x,y-plane and 3C PIV measurements in the y,z-plane were performed.

Investigations of the one array and four array configurations with the 2C PIV measurements yield comparable results obtained with the measurements at the TU Darmstadt. More detailed information of the downstream development on the interaction of the TS waves and the streaks were obtained depending on the approach for the streak generation. With the streak generation with one single array the TS waves exhibited an amplification in the low-speed streak just downstream of the array. Farther downstream the TS waves developed with a reduced growth in the high-speed and low-speed streak. Yielding the characteristic M-shaped form of the velocity fluctuations of the streaky TS waves([23]).

With the streak generation with four arrays the amplification of the TS waves in low-speed streak is increased with every additional array. TS waves within the low-speed streak reaching high amplitudes exceeding the range of the linear growth of the TS wave. At the last measurement position the TS waves don't reveal the typical shape of the velocity fluctuations of the 2D disturbances.

The 3C PIV measurements demonstrate the benefit of simultaneous measurements of spanwise modulation and velocity fluctuation. To provide a higher statistical significance of the velocity information a larger number of images with the PIV measurement is required. Nevertheless, the 3C PIV measurements shown a good agreement with the 2C PIV measurements obtained with the single array configuration.

6.3 Summary TS wave Attenuation

This chapter demonstrated the qualification of PAVG for boundary-layer control. In the first section the streak generation with a single actuator array in comparison with four cascaded arrays was demonstrated. The interaction of TS wave and streaks, depending on the approach of the streak generation, was shown. The different approaches of the streak generation reveal that an amplification and/or damping of the TS waves is possible. It is shown that all effects scale with the forcing magnitude of the plasma actuator.

Complementary measurements were performed at KTH, investigating the interaction of TS wave and streaks with the two different configurations for

the streak generation. Here, the streamwise development of the TS wave and the streaks, generated with the two different configurations, could be investigated. With the single array configuration an initial growth of the TS waves is observed in the low-speed streak. This agrees well with the findings by passive VGs ([140]). Farther downstream TS waves are reduced in amplitude in both the high-speed and low-speed streaks resulting in a negative damping factor. This initial growth occurs repeatedly with the four cascaded arrays, resulting in a strong amplification of the TS wave amplitude downstream of the last actuator array. This amplification seems to be related to the growth of the streak amplitude.

Future work should focus on the effect of the gradually increasing streak amplitude. Another interesting topic is the investigation of cascaded arrays with a larger streamwise distance, to reenergize the streaks when the TS waves are already decaying and a combination of both approaches: abrupt generation of strong enough streaks for attenuating the waves and subsequent repeated reenergization of the otherwise decaying streaks.

7 Conclusion and Outlook

The present study focuses in the first part on the characterization and quantification of dielectric barrier discharge plasma actuators. These insights were used to evaluate the parameter influences for the generation of stable vortices in laminar boundary layers and to qualify the plasma actuator vortex generators for flow control.
For the characterization and quantification of dielectric barrier discharge plasma actuators various existing and established strategies have been utilized and were extended by novel approaches. Both time averaged and time resolved analysis methods were applied. Based on this characterization empirical scaling laws for describing the influences of the operating conditions and the actuator setup were derived. The direct scaling of the induced body force is achieved by influencing the discharge intensity with the operating conditions and actuator setup. Besides this direct scaling an indirect method for decoupling the spatial extent and the magnitude of the force was introduced. This is achieved by non-continuous operation of the plasma actuator, allowing adjustment of the the time-averaged force production. The scaling methods were the prequisite creating stable vortices in a laminar boundary layer.
Based on the quantification and the scaling of the induced body force the parameters for the vortex generation by means of plasma actuator was identified and discussed. Qualitative and quantitative investigations on the vortex generation were performed to evaluate these influences.
In a last step the qualification of plasma actuator vortex generators boundary-layer control was demonstrated. The longitudinal vortices created by the plasma actuator deform a boundary layer and the streamwise velocity component is modulated in streaks of higher and lower velocity. The interaction of Tollmien-Schlichting waves with these streaks was investigated in two different wind tunnels. Two different approaches of creating streaks (abrupt creation and gradually increasing the streak amplitude) were investigated, revealing an attenuation or an amplification of the Tollmien-Schlichting waves. The amplification of the TS waves reveal a relation to the increase of the streak amplitude. In the following sections the main findings and conclusions of the different investigations are briefly summarized.

7.1 Characterization of DBD Plasma Actuators

The lower and upper operation limits were identified using electrical characteristic and optical measurements of the discharge. This provides a range for the operation of the plasma actuator in which a temporally and spatially homogeneous discharge and, thus, a two-dimensional force distribution along the upper electrode exists. The relation of the electrical measures agree well with previous literature, a relation between operating voltage V and consumed actuator power of $P_A \propto V^{7/2}$ as well as the relation of the operating frequency and the consumed power of $P_A \propto f$ was observed. Analysis of the velocity field measurements exhibit good agreement with the assumption that the induced wall-jet in quiescent air is a laminar flow. Additionally, it was demonstrated, that the laminar wall jet is deformed inside the discharge region due to the acceleration close to the wall. An improved self-similarity of the induced wall jet was demonstrated, when the discharge related length (e.g. the plasma extension) is taken into account for the evaluation.

The force production was analyzed in the previously defined operation range and was characterized by different measurement techniques. The relations of the force magnitude and the electrical measures: voltage V and power consumption P_A, reveal a good agreement with the previous literature and the relation of $F \propto V^{7/2}$ and $F \propto P_A$.

Phase-averaged velocity measurements and the time dependent evaluation of the force-field density and magnitude showed a good consistency with data found in literature, although the actuator was operated at a significantly higher frequency. This demonstrates that plasma actuators exhibit similar characteristics over a larger operation range.

7.2 Scaling of the Induced Body Force

The two options of directly influencing the induced body force in its magnitude and distribution: operating conditions and geometry, were investigated with three independent and simultaneously applied analysis methods.

The scaling law for the electrical characteristics could be summarized to one general relation between the consumed power, applied voltage, operating frequency and the influence of the thickness and material constant of the dielectric layer.

$$\frac{P_A/L}{fV^{7/2}} \cdot \frac{\epsilon}{d} = const$$

Analogue to this, the interrelation of the produced thrust with the electrical characteristics, dependent on the actuator setup and the operating conditions, could be expressed with the following equations:

$$\begin{aligned} V^{7/2} &\propto F_t \frac{1}{f^{1/4}} \frac{d^{1/2}}{\epsilon^{3/10}} \\ P_A &\propto F_t \cdot f^{3/4} \cdot \frac{\epsilon^{7/10}}{d^{1/2}} \end{aligned}$$

These scaling relations allow determination of changes in the performance of an actuator, based on one known configuration.

The indirect scaling of the induced body force is achieved with a discontinuous operation of the actuator. An analysis of the force field was used to describe the influence of the discontinuous force production on the force magnitude and the extension of the force field. It was demonstrated, that the time averaged force magnitude can be adjusted in a wide range without changing the time averaged size of the force field.

7.3 Governing Parameters of on Plasma Actuator Vortex Generators

For generating stable vortices in a laminar boundary layer the forcing magnitude of the plasma actuator has to be carefully adjusted. The qualitative investigation of plasma actuators for active vortex generation shows the complex interaction of numerous parameters. Based on 3C PIV measurements vortex identification methods were applied to analyze the vortex formation in an array of plasma actuator vortex generators at very low forcing.

The geometry of the plasma actuator array (electrode spacing and electrode width) influences primarily the spatial spanwise distribution of the streaks; however the spatial distribution of the vortices/streaks was also determined by the combination of the plasma extension and the electrode width. With increasing electrode length, the generated vortices and thus the created streaks were intensified. The same can be achieved with a higher applied voltage or by adjusting the duty cycle. The independent adjustment of force magnitude and spatial extent of the force by pulsed

operation offers the possibility to adjust the amplitude without influencing the spatial distribution.

Based on this knowledge a plasma actuator vortex generator was designed with an equal streak distribution, as required for the boundary-layer control.

7.4 Boundary-Layer Control with PAVG

For the qualification of the plasma actuator vortex generator for transition control, the interaction of Tollmien-Schlichting waves with these streaks was investigated in two different wind tunnels. Two different approaches of creating streaks (abrupt creation and gradually increasing the streak amplitude) were investigated, revealing an attenuation or an amplification of the Tollmien-Schlichting waves.

With the first approach (abrupt creation) an initial amplification was observed, before the Tollmien-Schlichting waves developed with a reduced growth farther downstream. With the gradually increasing streak amplitude this initial amplification was repeated. Thus the amplification of the TS waves reveal a relation to the increase of the streak amplitude.

7.5 Outlook

Based on the characterization of the plasma actuator, that shows a good agreement with the previous literature, empirical scaling laws were derived allowing to predetermine changes in the produced thrust and consumed power. The layout and the design of the actuator for an experimental setup can be based on an initial configuration. Premised on robust and generally valid scaling laws, a more universal development of empirical actuator models for numerical simulations is now possible. This allows a better comparability of experiment and simulation.

Even though these new scaling relations appear promising to describe and classify the consumed electrical power and produced thrust of DBD plasma actuators with varying operating conditions and changes in the dielectric, these correlations do not yet include any information about changes of the electrode arrangement. For a better comparability of experiments of different research groups, it is necessary to quantify the influence of these additional geometrical parameters.

For the active vortex generation of stable vortices in laminar boundary

layers with plasma actuators complementary investigations are necessary to allow a quantification of the parameter influences. An extension of the investigations to higher free-stream velocities would allow to investigate the qualification of plasma actuator vortex generation for different boundary-layer control scenarios.

Future work on the attenuation of Tollmien-Schlichting waves with plasma actuator vortex generators should focus on the effect of the gradually increasing streak amplitude. In this context an increase of the streamwise distance of cascaded arrays, to reenergize the streaks (when the TS waves are already decaying) could improve the attenuation or a combination of both approaches: abrupt generation of strong enough streaks for attenuating the waves and subsequent repeated reenergization of the otherwise decaying streaks.

Bibliography

[1] T. Abe, Y. Takizawa, and S. Sato. A parametric experimental study for momentum transfer by plasma actuator. In *AIAA 2007-185; 45th AIAA Aerospace Sciences Meeting and Exhibit, Reno, Nevada, USA*, 2007.

[2] T. Abe, Y. Takizawa, and S. Sato. Experimental study for momentum transfer in a dielectric barrier discharge plasma actuator. *AIAA Journal*, 46(9):2248–2256, 2008.

[3] T. Albrecht, T. Weier, G. Gerbeth, H. Metzkes, and J. Stiller. A method to estimate the planar, instantaneous body force distribution from velocity field measurements. *Physics of Fluids*, 23(2):021702, 2011.

[4] K. Allégraud, O. Guaïtella, and A. Rousseau. Spatio-temporal breakdown in surface DBDs: evidence of collective effect. *Journal of Physics D: Applied Physics*, 40(24):7698, 2007.

[5] P. Andersson, L. Brandt, A. Bottaro, and D. S. Henningson. On the breakdown of boundary layer streaks. *J. Fluid Mech.*, 428:29–60, 2001.

[6] A. A. Bakchinov, G. R. Grek, . G. B. Klingmann, and V. V. Kozlov. Transition experiments in a boundary layer with embedded streamwise vortices. *Physics of Fluids*, 7:820–832, 1995.

[7] K. Barckmann, J. Kriegseis, S. Grundmann, and C. Tropea. Dielectric-barrier discharge plasmas for flow control at higher Mach numbers. In *AIAA 2010-4258; 5th Flow Control Conference, Chicago, Illinois, USA*, 2010.

[8] J. W. Baughn, C. O. Porter, B. L. Peterson, T. E. McLaughlin, C. L. Enloe, G. I. Font, and C. Baird. Momentum transfer for an aerodynamic plasma actuator with an imposed boundary layer. In *AIAA 2006-166; 44th AIAA Aerospace Sciences Meeting and Exhibit, Reno, Nevada, USA*, 2006.

[9] N. Bénard, P. Braud, G. Touchard, and E. Moreau. Detachment and attachment of an axisymmetric non-reactive jet with turbulent shear layer: Control by plasma actuator. *Experimental Thermal and Fluid Science*, 32(6):1193 – 1203, 2008.

[10] N. Benard, A. Debien, and E. Moreau. Time-dependent volume force produced by a non-thermal plasma actuator from experimental velocity field. *Journal of Physics D: Applied Physics*, 46:245201, 2013.

[11] N. Bénard and E. Moreau. Capabilities of the Dielectric Barrier Discharge Plasma Actuator for Multi-Frequency Excitations. *Journal of Physics D: Applied Physics*, 43(14):145201, 2010.

[12] N. Bénard, E. Moreau, J. Griffin, and L. Cattafesta. Slope seeking for autonomous lift improvement by plasma surface discharge. *Experiments in Fluids*, DOI 10.1007/s00348-009-0767-6, 2009.

[13] J. P. Boeuf, Y. Lagmich, and L. C. Pitchford. Contribution of positive and negative ions to the electrohydrodynamic force in a dielectric barrier discharge plasma actuator operating in air. *Journal of Applied Physics*, 106(2):023115, 2009.

[14] J. P. Boeuf, Y. Lagmich, T. Unfer, T. Callegari, and L. C. Pitchford. Electrohydrodynamic force in dielectric barrier discharge plasma actuators. *Journal of Physics D: Applied Physics*, 40:652–662, Feb. 2007.

[15] V. Boucinha, R. Joussot, P. Magnier, R. Weber, and A. Leroy-Chesneau. Characterization of the ionic wind produced by a DBD actuator designed to control the laminar-to-turbulent transition. In *14th Int Symp on Applications of Laser Techniques to Fluid Mechanics*, 2008.

[16] N. S. J. Braithwaite. Introduction to gas discharges. *Plasma Sources Science and Technology*, 9(4):517–527, 2000.

[17] S. Bürkle. On the nature and behavior of filaments in the dielectric barrier discharge of plasma actuators. Master's thesis, TU Darmstadt, 2013.

[18] D. Caruana, A. Mignosi, M. Corrège, A. L. Pourhiet, and A. M. Rodde. Buffet and buffeting control in transonic flow. *Aerospace, Science and Technology*, 9:605–616, 2005.

[19] D. Caruana, A. Mignosi, C. Robitaillié, and M. Corrège. Separated flow and buffeting control. *Flow, Turbulence and Combustion*, 71:221–245, 2004.

[20] T. C. Corke and C. He. Plasma flapts and slats: An application of weakly-ionized plasma actuators. In *AIAA 2004-2127, 2nd AIAA Flow Control Conference, Portland, OR*, 2004.

[21] T. C. Corke, M. L. Post, and D. M. Orlov. Single dielectric barrier discharge plasma enhanced aerodynamics: Physics, modeling and applications. *Experiments in Fluids*, 46:1–26, 2009.

[22] C. Cossu and L. Brandt. Stabilization of tollmien-schlichting waves by finite amplitude optimal streaks in the blasius boundary layer. *Phys. Fluids*, 14:L57–60, 2002.

[23] C. Cossu and L. Brandt. On tollmien-schlichting-like waves in streaky boundary layers. *European Journal of Mechanics B/Fluids*, 23:815–833, 2004.

[24] J. Dandois, V. Brunet, P. Molton, J.-C. Abart, and A. Lepage. Buffet control by means of mechanical and fluidic vortex generators. In *5th Flow Control Conference, AIAA 2010-4975*, 2010.

[25] A. Debien, N. Benard, and E. Moreau. Streamer inhibition for improving force and electric wind produced by dbd actuators. *Journal of Physics D: Applied Physics*, 45:215201, 2012.

[26] B. Dong, J. M. Bauchire, J. M. Pouvesle, P. Magnier, and D. Hong. Experimental study of a DBD surface discharge for the active control of subsonic airflow. *Journal of Physics D: Applied Physics*, 41(15):155201 (9pp), 2008.

[27] R. Durscher and S. Roy. Force measurement techniques and preliminary results using aerogels and ferroelectrics for dielectric barrier discharge actuators. In *AIAA 2011-3735; 42nd AIAA Plasmadynamics and Lasers Conference, Honolulu, Hawaii, USA*, 2011.

[28] R. Durscher and S. Roy. Evaluation of thrust measurement techniques for dielectric barrier discharge actuators. *Experiments in Fluids*, 53(4):1165–1176, 2012.

[29] C. Enloe, J. Baughn, G. Font, and T. McLaughlin. Parameterization of temporal structure in the single-dielectric-barrier aerodynamic plasma actuator. *AIAA Journal*, 44:1127–1136, 2006.

[30] C. L. Enloe, M. G. McHarg, G. I. Font, and T. E. McLaughlin. Plasma-induced force and self-induced drag in the dielectric barrier discharge aerodynamic plasma actuator. In *AIAA-2009-1622; 47th AIAA Aerospace Sciences Meeting, Orlando, Florida, USA*, 2009.

[31] C. L. Enloe, M. G. McHarg, and T. E. McLaughlin. Time-correlated force production measurements of the dielectric barrier discharge plasma aerodynamic actuator. *Journal of Applied Physics*, 103(7):073302–+, 2008.

[32] C. L. Enloe, T. E. McLaughlin, R. D. VanDyken, and J. C. Fischer. Plasma structure in the aerodynamic plasma actuator. In *AIAA-2004-0844; 42nd AIAA Aerospace Sciences Meeting and Exhibit, Reno, Nevada, USA*, 2004.

[33] C. L. Enloe, T. E. McLaughlin, R. D. VanDyken, K. D. Kachner, E. J. Jumper, and T. C. Corke. Mechanisms and responses of a single dielectric barrier plasma. In *AIAA 2003-1021; 41st Aerospace Sciences Meeting and Exhibit, Reno, Nevada, USA*, 2003.

[34] C. L. Enloe, T. E. McLaughlin, R. D. VanDyken, K. D. Kachner, E. J. Jumper, T. C. Corke, M. Post, and O. Haddad. Mechanisms and Responses of a Single Dielectric Barrier Plasma Actuator: Geometric Effects. *AIAA Journal*, 42(3):595–604, 2004.

[35] J. W. Ferry and L. Rovey. Thrust measurement of dielectric barrier discharge plasma actuators and power requirements for aerodynamic control. In *AIAA 2010-4982; 5th Flow Control Conference, Chicago, Illinois, USA*, 2010.

[36] S. Flügge, editor. *Encyclopedia of Physics*, volume Volume 22: Gas Discharges 2. Springer, 1956.

[37] G. I. Font, C. L. Enloe, and T. E. McLaughlin. Plasma Volumetric Effects on the Force Production of a Plasma Actuator. *AIAA Journal*, 48:1869–1874, 2010.

[38] G. I. Font and W. L. Morgan. Plasma discharges in atmospheric pressure oxygen for boundary layer separation control. In *AIAA 2005-4632; 35th AIAA Fluid Dynamics Conference and Exhibit, Toronto, Ontario, Canada*, 2005.

[39] M. Forte, J. Jolibois, E. Moreau, G. Touchard, and M. Cazalens. Control of the shear-layer in thewake of an axisymmetrical airfoil using a dbd plasma actuator. In *IUTAM Symposium on Flow Control and MEMS, 209-215.*, 2008.

[40] M. Forte, J. Jolibois, J. Pons, E. Moreau, G. Touchard, and M. Cazalens. Optimization of a dielectric barrier discharge actuator by stationary and non-stationary measurements of the induced flow velocity: Application to airflow control. *Experiments in Fluids*, 43:917–928, 2007.

[41] J. Fransson, A. Talamelli, L. Brandt, and C. Cossu. Delaying transition to turbulence by a passive mechanism. *Phys. Rev. Lett.*, 96:064501– 1–4, 2006.

[42] J. H. M. Fransson, L. Brandt, A. Talamelli, and C. Cossu. Experimental and theoretical investigation of the nonmodal growth of steady streaks in a flat plate boundary layer. *Physics of Fluids*, 16:10, 2004.

[43] J. H. M. Fransson, L. Brandt, A. Talamelli, and C. Cossu. Experimental study of the stabilization of Tollmien-Schlichting waves by finite amplitude streaks. *Physics of Fluids*, 17:054110, 2005.

[44] R. Gadri and J. Roth. Glow discharge-like characteristics of a oaugdp revealed by computer modeling. In *Plasma Science, 1998. 25th Anniversary. IEEE Conference Record - Abstracts. 1998 IEEE International on Plasma Science*, page 288, jun 1998.

[45] V. I. Gibalov and G. J. Pietsch. The development of dielectric barrier discharges in gas gaps and on surfaces. *Journal of Physics D: Applied Physics*, 33(20):2618, 2000.

[46] M. B. Glauert. The wall jet. *Journal of Fluid Mechanics*, 1(06):625–643, 1956.

[47] G. Godard, J. Foucaut, and M. Stanislas. Control of a decelerating boundary layer. part 2: Optimization of slotted jets vortex generators. *Aerospace Science and Technology*, 10:394–400, 2006.

[48] G. Godard and M. Stanislas. Control of a decelerating boundary layer. part 1: Optimization of passive vortex generators. *Aerospace Science and Technology*, 10:181–191, 2006.

[49] G. Godard and M. Stanislas. Control of a decelerating boundary layer. part 3: Optimization of round jets vortex generators. *Aerospace Science and Technology*, 10:455–464, 2006.

[50] L. Graftieaux, M. Michard, and N. Grosjean. Combining piv, pod and vortex identification algorithms for the study of unsteady turbulent swirling flows. *Meas. Sci. Technol.*, 12:1422–1429, 2001.

[51] J. W. Gregory, C. L. Enloe, G. I. Font, and T. E. McLaughlin. Force production mechanisms of a dielectric-barrier discharge plasma actuator. In *AIAA 2007-185; 45th AIAA Aerospace Sciences Meeting and Exhibit, Reno, Nevada, USA*, 2007.

[52] S. Grundmann, E. L. Sayles, and J. K. Eaton. Sensitivity of an asymmetric 3d diffuser to plasma-actuator induced inlet condition perturbations. *Experiments in Fluids*, 50:217–231, 2011.

[53] S. Grundmann and C. Tropea. Experimental transition delay using glow-discharge plasma actuators. *Experiments in Fluids*, 42(4):653–657, 2007.

[54] S. Grundmann and C. Tropea. Delay of boundary-layer transition using plasma actuators. In *AIAA-2008-1369; 46th AIAA Aerospace Science Meeting and Exhibit; Reno, Nevada, USA*, 2008.

[55] A. M. Gürün and E. B. White. Tollmien-schlichting wave suppression and transition delay using stationary transient disturbances. In *4th AIAA Theoretical Fluid Mechanics Meeting, AIAA 2005-5313*, 2005.

[56] R. E. Hanson, J. Kimelman, N. M. Houser, and P. Lavoie. Effect of dielectric degradation on dielectric barrier discharge plasma actuator performance. In *51st AIAA ASM, Grapevine*. AIAA, AIAA 2013-0397.

[57] R. E. Hanson, P. Lavoie, K. M. Bade, and A. M. Naguib. Steady-state closed-loop control of bypass boundary layer transition using plasma actuators. In *50th AIAA Aerospace Sciences Meeting including the New Horizons Forum and Aerospace Exposition 09 - 12 January 2012, Nashville, Tennessee*. AIAA, AIAA 2012-1140.

[58] C. He, T. C. Corke, and M. P. Patel. Numerical and experimental analysis of plasma flow control over a hump model. In *45th AIAA ASM 2007, Reno, AIAA 2007-935*. AIAA, 2007.

[59] E. Hering, J. Gutekunst, and R. Martin. *Elektrotechink für Maschinenbauer*. Springer, 1998.

[60] A. Hoskinson and N. Hershkowitz. Differences between dielectric barrier discharge plasma actuators with cylindrical and rectangular exposed electrodes. *Journal of Physics D: Applied Physics*, 43:065205, 2010.

[61] A. Hoskinson, N. Hershkowitz, and D. Ashpis. Comparisons of force measurement methods for DBD plasma actuators in quiescent air. In *AIAA 2009-485; 47th AIAA Aerospace Sciences Meeting, Orlando, Florida, USA*, 2009.

[62] A. R. Hoskinson, N. Hershkowitz, and D. E. Ashpis. Force measurements of single and double barrier DBD plasma actuators in quiescent air. *Journal of Physics D: Applied Physics*, 41(24):245209 (9pp), 2008.

[63] A. R. Hoskinson, L. Oksuz, and N. Hershkowitz. Microdischarge propagation and expansion in a surface dielectric barrier discharge. *Applied Physics Letters*, 93(22):221501–+, Dec. 2008.

[64] X. Huang and X. Zhang. Streamwise and spanwise plasma actuators for flow-induced cavity noise control. *Physics of Fluids*, 20(3):037101, 2008.

[65] S. Im, H. Do, and M. A. Cappelli. Dielectric barrier discharge control of a turbulent boundary layer in a supersonic flow. *Applied Physics Letters*, 97(4):041503, 2010.

[66] J. Jolibois, M. Forte, and r. Moreau. Application of an AC barrier discharge actuator to control airflow separation above a NACA 0015 airfoil: Optimization of the actuation location along the chord. *Journal of Electrostatics*, 66(9-10):496–503, 2008.

[67] T. Jukes, K. Choi, G. Johnson, and S. Scott. Characterization of surface plasma-induced wall flows through velocity and temperature measurements. *AIAA Journal*, 44:764–771, Apr. 2006.

[68] T. N. Jukes and K.-S. Choi. Control of unsteady flow separation over a circular cylinder using dielectric-barrier-discharge surface plasma. *Physics of Fluids*, 21(9):094106, 2009.

[69] T. N. Jukes and K.-S. Choi. Flow control around a circular cylinder using pulsed dielectric barrier discharge surface plasma. *Physics of Fluids*, 21(8):084103, 2009.

[70] T. N. Jukes and K.-S. Choi. Dielectric-barrier-discharge vortex generators: characterisation and optimisation for flow separation control. *Experiments in Fluids*, 52:329–345, 2012.

[71] T. N. Jukes and K.-S. Choi. On the formation of streamwise vortices by plasma vortex generators. *J. Fluid Mech.*, 733:370–393, 2013.

[72] T. N. Jukes, T. Segawa, and H. Furutani. Active flow separation control on a naca 4418 using dbd vortex generators and fbg sensors. In *50th AIAA Aerospace Sciences Meeting including the New Horizons Forum and Aerospace Exposition 09 - 12 January 2012, Nashville, Tennessee AIAA 2012-1139*, 2012.

[73] T. N. Jukes, T. Segawa, and H. Furutani. Flow control on a naca 4418 using dielectric-barrier-discharge vortex generators. *AIAA Journal*, 51:452–464, 2013.

[74] C. J. Kähler, S. Scharnowski, and C. Cierpka. On the uncertainty of digital piv and ptv near walls. *Experiments in Fluids*, 52:641–1656, 2012.

[75] C. S. Kalra, S. Zaidi, and R. B. Miles. Shockwave induced turbulent boundary layer separation control with plasma actuators. In *AIAA 2008-1092, 46th AIAA Aerospace Sciences Meeting and Exhibit, Reno, Nevada*, 2008.

[76] S. Kanazawa, M. Kogoma, T. Moriwaki, and S. Okazaki. Stable glow plasma at atmospheric pressure. *J. Phys. D: Appl. Phys.*, 21:836–840., 1988.

[77] W. Kim, H. Do, M. G. Mungal, and M. A. Capelli. On the role of oxygen in dielectric barrier discharge actuation of aerodynamic flows. *Applied Physics Letters*, 91:181501, 2007.

[78] U. Kogelschatz. Dielectric-barrier discharges: Their history, discharge physics, and industrial applications. *Plasma Chemistry and Plasma Processing*, 23:1–46, 2003.

[79] M. Kotsonis, S. Ghaemi, R. Giepman, and L. Veldhuis. Experimental study on the body force field of dielectric barrier discharge actuators. In *AIAA 2010-4630; 41st Plasmadynamics and Lasers Conference, Chicago, Illinois, USA*, 2010.

[80] A. V. Kozlov and F. O. Thomas. Bluff-body flow control via two types of dielectric barrier discharge plasma actuation. *AIAA Journal*, 49:1919–1931, 2011.

[81] A. V. Kozlov and F. O. Thomas. Plasma flow control of cylinders in a tandem configuration. *AIAA Journal*, 49:2183–2193, 2011.

[82] J. Kriegseis. *Performance characterization and quantification of dielectric barrier discharge plasma actuators.* PhD thesis, TU Darmstadt, Dezember 2011.

[83] J. Kriegseis, S. Grundmann, and C. Tropea. Power consumption, discharge capacitance and light emission as measures for thrust production of dielectric barrier discharge plasma actuators. *Journal of Applied Physics*, 110(1):013305, 2011.

[84] J. Kriegseis, B. Möller, S. Grundmann, and C. Tropea. Capacitance and power consumption quantification of dielectric barrier discharge (DBD) plasma actuators. *Journal of Electrostatics*, 69(4):302 – 312, 2011.

[85] J. Kriegseis, B. Möller, S. Grundmann, and C. Tropea. On performance and efficiency of dielectric barrier discharge plasma actuators for flow control applications. *International Journal of Flow Control*, 4:3+4, 2012.

[86] J. Kriegseis, D. Schröter, S. Grundmann, and C. Tropea. Online-characterization of dielectric barrier discharge plasma actuators for optimized efficiency of aerodynamical flow control applications. *Journal of Physics: Conference Series*, 301(1):012020, 2011.

[87] J. Kriegseis, C. Schwarz, C. Tropea, and S. Grundmann. Velocity-information-based force-term estimation of dielectric-barrier discharge plasma actuators. *Journal of Physics D: Applied Physics*, 46:055202, 2013.

[88] A. M. Kuethe. Effect of streamwise vortices on wake properties associated with sound generation. *Journal of Aircraft*, 9:715–719, 1972.

[89] A. Kurz, A. Duchmann, A. Widmann, S. Grundmann, and C. Tropea. Characterization of the active Tollmien-Schlichting wave damping process using phase-locked piv. In *accepted at 64th Annual Meeting of the APS Division of Fluid Dynamics, November 20-22, 2011, Baltimore, Maryland*, 2011.

[90] Y.-h. Li, Y. Wu, M. Zhou, C.-b. Su, X.-w. Zhang, and J.-q. Zhu. Control of the corner separation in a compressor cascade by steady and unsteady plasma aerodynamic actuation. *Experiments in Fluids*, 48:1015–1023, 2010.

[91] A. V. Likhanskii, M. N. Shneider, S. O. Macheret, and R. B. Miles. Modeling of dielectric barrier discharge plasma actuator in air. *Journal of Applied Physics*, 103(5):053305, 2008.

[92] J. C. Lin. Review of research on low-profile vortexgenerators to control boundary-layer separation. *Progress in Aerospace Sciences*, 38:389–420, 2002.

[93] B. Lindgren and A. Johansson. Evaluation of a new wind tunnel with expanding corners. *Experiments in Fluids*, 36:197–203, 2004.

[94] J. Little, M. Nishihara, Adamovich, and M. Samimy. Separation control from the flap of a high - lift airfoil using dbd plasma actuation. In *AIAA 2008-4200, 4th Flow Control Conference , Seattle, Washington*, 2008.

[95] J. Little, M. Nishihara, I. Adamovich, and M. Samimy. High-lift airfoil trailing edge separation control using a single dielectric barrier discharge plasma actuator. *Experiments in Fluids*, 2009.

[96] J. Little, M. Nishihara, I. Adamovich, and M. Samimy. Separation control from the flap of a high-lift airfol using dbd plasma actuators. In *AIAA 2009-145, AIAA Aerospace Sciences Meeting Including The New Horizons Forum and Aerospace Exposition, Orlando, Florida*, 2009.

[97] J. Little, K. Takashima, M. Nishihara, I. Adamovich, and M. Samimy. High lift airfoil leading edge separation control with nanosecond pulse driven dbd plasma actuators. In *5th Flow Control Conference 28 June - 1 July 2010, Chicago, Illinois AIAA 2010-4256*, 2010.

[98] Y. Liu, T. A. Zaki, and P. A. Durbin. Boundary-layer transition by interaction of discrete and continuous modes. *J. Fluid Mech.*, 604:199–233, 2008.

[99] Y. Liu, T. A. Zaki, and P. A. Durbin. Floquet analysis of secondary instability of boundary layers distorted by klebanoff streaks and tollmien-schlichting waves. *Phys. Fluids*, 20:124102, 2008.

[100] O. Lögdberg, K. Angele, and P. H. Alfredsson. On the robustness of separation control by streamwise vortices. *European Journal of Mechanics B/Fluids*, 29:9–17, 2010.

[101] T. C. Manley. The electric characteristics of the ozonator discharge. *Journal of The Electrochemical Society*, 84(1):83–96, 1943.

[102] F. Massines, A. Rabehi, P. Decomps, R. B. Gadri, P. Ségur, and C. Mayoux. Experimental and theoretical study of a glow discharge at atmospheric pressure controlled by dielectric barrier. *Journal of Applied Physics*, 83:2950–2957, Mar. 1998.

[103] T. E. McLaughlin, M. D. Munska, J. P. Vaeth, T. E. Dauwalter, J. R. Goode, and S. G. Siegel. Plasma - based actuators for cylinder wake vortex control. In *AIAA 2004-2129, UB/TIB Hannover, Tagung RN 160*, 2004.

[104] L. P. Melton, C.-S. Yao, and A. Seifert. Active control of separation from the flap of a supercritical airfoil. *AIAA Journal*, 44:34–41, 2006.

[105] E. Moreau. Airflow control by Non-thermal plasma actuators. *Journal of Physics D: Applied Physics*, 40:605–636, 2007.

[106] E. Moreau, R. Sosa, and G. Artana. Electric wind produced by surface plasma actuators: a new dielectric barrier discharge based on a three-electrode geometry. *Journal of Physics D: Applied Physics*, 41, 2008.

[107] J. P. Murphy and P. Lavoie. Characterization of dbd plasma actuators via piv measurements. In *51st AIAA Aerospace Sciences Meeting, Grapevine, Texas*. AIAA, AIAA 2013-0346.

[108] G. Nersisyan and W. G. Graham. Characterization of a dielectric barrier discharge operating in an open reactor with flowing helium. *Plasma Sources Science Technology*, 13:582–587, Nov. 2004.

[109] D. Orlov, T. Apker, C. He, H. Othman, and T. Corke. Modeling and experiment of leading edge separation control using SDBD plasma actuators. In *AIAA 2007-0877; 45th Aerospace Sciences Meeting, 8-11 January 2007, Reno, Nevada, USA*, 2007.

[110] D. Orlov, T. Corke, and M. Patel. Electric circuit model for aerodynamic plasma actuator. In *AIAA 2006-1206; 44th AIAA Aerospace Science Meeting and Exhibit; Reno, Nevada, USA*, 2006.

[111] D. Orlov and T. C. Corke. Numerical simulation of aerodynamic plasma actuator effects. In *AIAA 2005-1083; AIAA 43rd Aerospace Sciences Meeting, Reno, Nevada, USA*, 2005.

[112] J. Park, I. Henins, H. W. Herrmann, and G. S. Selwyn. Gas breakdown in an atmospheric pressure radio-frequency capacitive plasma source. *J. Appl. Phys.*, 89:15–19, 2001.

[113] F. Paschen. Ueber die zum Funkenübergang in Luft, Wasserstoff und Kohlensäure bei verschiedenen Drucken erforderliche Potentialdifferenz. *Annalen der Physik*, 273(5):69–96, 1889.

[114] M. P. Patel, T. T. Ng, S. Vasudevan, T. Corke, M. Post, T. McLaughlin, and C. F. Suchomel. Scaling effects of an Aerodynamic Plasma Actuator. *Journal of Aircraft*, 45:223–236, 2008.

[115] J. Poggie, C. P. Tilmann, P. M. Flick, J. S. Silkey, B. A. Osborne, G. Ervin, D. Maric, S. Mangalam, and A. Mangalam. Closed-loop stall control on a morphing airfoil using hot-film sensors and dbd actuators. In *AIAA 2010-547; 48th AIAA Aerospace Sciences Meeting, Orlando, Florida, USA*, 2010.

[116] J. Pons, E. Moreau, and G. Touchard. Asymmetric surface dielectric barrier discharge in air at atmospheric pressure: Electrical properties and induced airflow characteristics. *Journal of Physics D: Applied Physics*, 38(19):3635, 2005.

[117] J. Pons, E. Moreau, and G. Touchard. Electrohydrodynamic properties of surface dielectric barrier discharges in ambient air for aerodynamic airflow control. In *28. ICPIG, July 15-20, 2007, Prague, Czech Republic*, 2007.

[118] D. Poon, T. Simon, U. Kortshagen, and D. Ernie. Experimental studies of plasma actuator performance for separation control. In *48th*

AIAA Aerospace Sciences Meeting Including the New Horizons Forum and Aerospace Exposition 4 - 7 January 2010, Orlando, Florida AIAA 2010-1219. AIAA, 2010.

[119] C. O. Porter, J. W. Baughn, T. E. McLaughlin, C. L. Enloe, and G. I. Font. Plasma actuator force measurements. *AIAA Journal*, 45:1562–1570, July 2007.

[120] C. O. Porter, T. E. McLaughlin, C. L. Enloe, G. I. Font, J. Roney, and J. W. Baughn. Boundary layer control using a dbd plasma actuator. In *AIAA 2007-786; 45th AIAA Aerospace Sciences Meeting and Exhibit, Reno, Nevada, USA*, 2007.

[121] C. O. Porter, B. J. W, T. E. McLaughlin, C. L. Enloe, and G. I. Font. Temporal force measurements on an aerodynamic plasma actuator. In *AIAA 2006-1206; 44th AIAA Aerospace Science Meeting and Exhibit; Reno, Nevada, USA*, 2006.

[122] M. L. Post and T. C. Corke. Separation control on high angle of attack airfoil using plasma actuators. *AIAA Journal*, 42:2177 – 2184, 2004.

[123] I. Radu, R. Bartnikas, and M. R. Wertheimer. Frequency and voltage dependence of glow and pseudoglow discharges in helium under atmospheric pressure. *IEEE Transaction on Plasma Science*, 31:1363–1378, 2003.

[124] Y. P. Raizer, M. N. Shneider, and N. A. Yatsenko. *Radio-Frequency Capacitive Discharges*. CRC Press, 1995.

[125] E. Reshotko. Boundary-layer stability and transition. *Annual Review of Fluid Mechanics*, 8(1):311–349, 1976.

[126] J. Roth. Aerodynamic flow acceleration using paraelectric and peristaltic electrohydrodynamic effects of a One Atmosphere Uniform Glow Discharge Plasma. *Physics of Plasmas*, 10:2117, 2003.

[127] J. R. Roth. *Industrial Plasma Engineering Volume 1: Principles*. IOP, 1995.

[128] J. R. Roth. *Industrial Plasma Engineering Volume 2: Applications to Nonthermal Plasma Processing*. IOP, 2001.

[129] J. R. Roth, D. Sherman, and S. P. Wilkinson. Boundary layer fow control with a one atmosphere uniform glow discharge surface plasma. In *AIAA 1998-0328; 36th AIAA Aerospace Science Meeting and Exhibit; Reno, Nevada, USA*, 1998.

[130] R. J. Roth and X. Dai. Optimization of the aerodynamic plasma actuator as an electrohydrodynamic (ehd) electrical device. In *AIAA 2006-1203, 44th AIAA Aerospace Sciences Meeting and Exhibit, Reno, Nevada, USA*, 2006.

[131] R. J. Roth, R. C. M. Madhan, M. Yadav, J. Rahel, and S. P. Wilkinson. Flow field measurements of paraelectric, peristaltic, and combined plasma actuators based on the one atmosphere uniform glow discharge plasma. In *AIAA 2004-845, 42nd AIAA Aerospace Sciences Meeting and Exhibit, Reno, Nevada*, 2004.

[132] R. J. Roth, J. Rahel, X. Dai, and D. M. Sherman. The physics and phenomenology of one atmosphere uniform glow discharge plasma reactors for surface treatment applications. *Journal of Physics D: Applied Physics*, 38:555–567, 2005.

[133] R. J. Roth, D. M. Sherman, and S. P. Wilkinson. Electrohydrodynamic flow control with a glow-discharge surface plasma. *AIAA Journal*, 38:1166–1172, 2000.

[134] D. V. Roupassov, A. A. Nikipelov, M. M. Nudnova, and A. Y. Starikovskii. Flow separation control by plasma actuator with nanosecond pulsed-periodic discharge. *AIAA Journal*, 47(1):168–185, 2009.

[135] D. M. Schatzman and F. O. Thomas. Turbulent boundary-layer separation control with single dielectric barrier discharge plasma actuators. In *4th Flow Control Conference 23 - 26 June 2008, Seattle, Washington AIAA 2008-4199*, 2008.

[136] D. M. Schatzman and F. O. Thomas. Turbulent boundary-layer separation control with single dielectric barrier discharge plasma actuators. *AIAA Journal*, Vol. 48, No. 8:1620–1634, August 2010.

[137] H. Schlichting and K. Gersten. *Grenzschicht-Theorie*. Springer, 2005.

[138] W. Schoppa and F. Hussain. A large-scale control strategy for drag reduction in turbulent boundary layers. *Phys. Fluids*, 10:1049, 1998.

[139] A. Schütze, J. Y. Jeong, S. E. Babayan, J. Park, G. S. Selwyn, and R. F. Hicks. The atmospheric-pressure plasma jet: A review and comparison to other plasma sources. *IEEE TRANSACTIONS ON PLASMA SCIENCE*, 26(6):1685–1694, 1998.

[140] S. Shahinfar, S. S. Sattarzadeh, J. H. M. Fransson, , and A. Talamelli. Revival of classical vortex generators now for transition delay. *Phys. Rev. Lett.*, 109:074501, 2012.

[141] J. J. Shi, X. T. Deng, R. Hall, J. D. Punnett, and M. G. Kong. Three modes in a readio frequency atmospheric pressure glow discharge. *J. Appl. Phys.*, 94(10):6303–6310, 2003.

[142] J. J. Shi and M. G. Kong. Expansion of the plasma stability range in radio-frequency atmosphericpressure glow discharges. *Applied Physics Letters*, 87:201501–1–4, 2005.

[143] J. J. Shi, D. W. Liu, and M. G. Kong. Plasma stability control using dielectric barriers in radio-frequency atmospheric pressure glow discharges. *Applied Physics Letters*, 89:081502–1–4, 2006.

[144] A. A. Sidorenko, B. Y. Zanin, B. V. Postnikov, A. D. Budovsky, A. Y. Starikovskii, D. V. Roupassov, I. N. Zavialov, N. D. Malmuth, P. Smereczniak, and J. S. Silkey. Pulsed discharge actuators for rectangular wing separation control. In *AIAA 2007-941, 45th AIAA Aerospace Sciences Meeting and Exhibit, Reno, Nevada*, 2007.

[145] B. L. Snyder, K. Lewis, Joshua A.and Cohen, C. A. Seaver, and T. McLaughlin. Closed-loop plasma active control technology (clopact). In *AIAA 2007-108, 45th AIAA Aerospace Sciences Meeting and Exhibit, Reno, Nevada*, 2007.

[146] S. A. Stanfield. *A Spectroscopic Investigation of a Surface-Discharge-Mode, Dielectric Barrier Discharge.* PhD thesis, Wright State University, 2009.

[147] F. O. Thomas, T. C. Corke, M. Iqbal, A. Kozlov, and D. Schatzman. Optimization of dielectric barrier discharge plasma actuators for active aerodynamic flow controlv. *AIAA Journal*, 47:2169–2178, 2009.

[148] F. O. Thomas, A. Kozlov, and T. C. Corke. Plasma actuators for cylinder flow control and noise reduction. *AIAA Journal*, 47(8):1921–1931, 2008.

[149] J. S. Thorp, M. Akhtaruzzaman, and D. Evans. The dielectric properties of alumina substrates for microelectronic packaging. *Journal of Material Science*, 25:4143–4149, 1990.

[150] A. Tumin and E. Reshotko. Spatial theory of optimal disturbances in boundary layers. *Physics of Fluids*, 13:7, 2001.

[151] J. A. Valerioti. Pressure dependence of plasma actuated flow control. Master's thesis, Graduate School of the University of Notre Dame, 2010.

[152] R. Van Dyken, T. E. McLaughlin, and C. L. Enloe. Parametric investigations of a single dielectric barrier plasma actuator. In *AIAA 2004-0846*, 2004.

[153] P. Versailles, V. Gingras-Gosselin, and H. Vo. Impact of pressure and temperature on the performance of plasma actuators. *AIAA Journal*, 48:859–863, 2010.

[154] A. von Engel. Ionization in gases by electrons in electric fields. In S. Flügge, editor, *Encyclopedia of Physics*, volume Volume 21: Electron-Emission Gas Discharges 1, pages 504–573. Springer, 1956.

[155] H. E. Wagner, R. Brandenburg, K. V. Kozlov, A. Sonnenfeld, P. Michel, and J. F. Behnke. The barrier discharge: Basic properties and applications to surface treatment. *Vacuum*, 71(3):417 – 436, 2003.

[156] R. Wallis. A preliminary note on a modified type of air jet for boundary layer control. Technical report, Aeronautical Research Council, 1956.

[157] P. Wassermann and M. Kloker. Mechanisms and passive control of crossflow-vortex-induced transition in a three-dimensional boundary layer. *J. Fluid Mech.*, 456:49–84, 2002.

[158] R. D. Whalley and K.-S. Choi. Turbulent boundary-layer control with spanwise travelling waves. In *13th European Turbulence Conference*, volume 318 of *(ETC13)*, page 022039, 2011.

[159] E. B. White. Transient growth of stationary disturbances in a flat plate boundary layer. *Physics of Fluids*, 14:12, 2002.

[160] E. B. White, M. A. Shelley, and A. M. Gürün. Interactions of Tollmien-Schlichting waves an stationary transient disturbances. In *34th AIAA Fluid Dynamics Conference and Exhibit, AIAA 2004-2540*, 2004.

[161] F. M. White. *Viscous Fluid Flow.* McGraw-Hill Education, 1974.

[162] M. Wicks, F. O. Thomas, D. Schatzman, P. Bowles, T. C. Corke, M. Patel, and A. B. Cain. A parametric investigation of plasma streamwise vortex generator performance. In *AIAA 2012-0824 50th, AIAA Aerospace Science Meeting and Exhibit, Nashville, Tennessee*, 2012.

[163] B. Wilke. *Aerodynamische Strömungssteuerung mittels dielektrischen Barriereentladungs-Plasmaaktuatoren.* PhD thesis, Technische Universität Darmstadt, DLR Göttingen, 2009.

[164] S. William S, J. Ruben B. Canillo, and M. S. Reibert. Leading-edge roughness as a transition control mechanism. In *36th ASM. AIAA 98-0781*, 1998.

Nomenclature

Latin letters

upper case

symbol	SI unit	description
A_{st}	–	streak amplitude
A_{TS}	–	Tollmien-Schlichting wave amplitude
C, $C(t)$	F	capacitance
C_d	F	dielectric capacitance
C_eff	F	effective capacitance
C_g	F	gas capacitance
C_p	F	charge-probe capacitance
C_0	F	pure passive-component capacitance / cold capacitance
E_k	W s	consumed energy per discharge cycle k
F	$\mathrm{N} = \mathrm{kg\,m/s^2}$	steady force
F, F_i, $F_i(t)$	N	plasma force
F_t	N	thrust
F_b	N	body force
F_f	N	friction force
$G(x,t)$	–	gray value as a function of chord and time
$G(x)$	–	spanwise averaged light intensity
GV	–	integrated graz value
H_1, H_2	m	lengths of rocker
H_{12}	–	shape factor
I, $I(t)$	A	electric current
I_i	$\mathrm{Ns} = \mathrm{kg\,m/s}$	momentum
KTH	–	Kungliga Tekniska högskolan

		(Royal Institute of Technology)
L	m	actuator length
M	–	Mach number
N	–	number of images
N_z	–	spanwise number of gray-value informations
P_A	W	power consumption / actuator power
$P_{\mathrm{A},k}$	W	consumed power per discharge cycle k
P_L	W	power loss
P_S	W	power saving
Q, $Q(t)$	C	electric charge
R	Ω	electric resistance
Re	–	Reynolds number
T	s	period of periodic function
T	K	temperature
U_i	m/s	flow fields snapshot
u_max	m/s	maximum wall-jet velocity
U_∞	m/s	free-stream velocity
V, $V(t)$	V	operating voltage (peak-to-peak)
V_b	V	breakdown voltage (ignition potential)
V_p, $V_\mathrm{p}(t)$	V	charge-probe voltage (peak-to-peak)
$W(t)$	kg	weight balance signal
$\overline{W}_n$	kg	average of balance signals

lower case

symbol	SI unit	description
d	m	thickness of dielectric
f	$\mathrm{Hz} = 1/\mathrm{s}$	operating frequency
f_{mod}	$\mathrm{Hz} = 1/\mathrm{s}$	modulation frequency
f_i	$\mathrm{kg/m^2 s^2}$	volume-force density
f_res	Hz	natural resonant frequency
f_x	$\mathrm{kg/m^2 s^2}$	chordwise force density

f_y	$\mathrm{kg/m^2s^2}$	wall normal force density
g	$\mathrm{m/s^2}$	acceleration of gravity
$g_j(x,z)$	–	j^{th} spatial gray-value distribution
$\overline{g}(x,z)$	–	average spatial gray-value distribution
i	–	spanwise location ($i \in N_z$)
i, j, k	–	control variables of the coordinates
j	–	raw-image number ($j \in J$)
m	kg	mass
		charge number density
p	$\mathrm{bar} = \mathrm{kg/m\,s^2}$	gas/static pressure
p_0	bar	ambient pressure
t	s	time
u	m/s	velocity component in x-direction
u_i	m/s	velocity (free index i)
u_max	m/s	maximum velocity
u^*	–	normalized velocity
$\widehat{u_\phi}$	m/s	phase-averaged velocity fluctuation
v	m/s	velocity component in y-direction
w_1	m	dimension upper electrode
w_2	m	dimension lower electrode
x	m	chordwise coordinate
x_max	m	maximum x-coordinate
x_min	m	minimum x-coordinate
y	m	wall normal coordinate
y_max	m	maximum y-coordinate
y_min	m	minimum y-coordinate
y^*	–	normalized wall normal distance
z	m	spanwise coordinate

Greek letters

upper case

symbol	SI unit	description
Δt	s	exposure time
Δt	s	computation sequence of control circuit
Δx	m	chordwise plasma length (light-emission based)
Δx_{F}	m	chordwise penetration length (force-determination based)

lower case

symbol	SI unit	description
δ	m	wall-jet thickness
δ	m	Blasius length scale
$\delta_{1/2}$	m	wall-normal distance of 50% wall-jet velocity
η	$\mathrm{Pa\,s{=}Ns/m^2}$	dynamical viscosity
η	–	normalized wall-normal distance
η^*_{FM}	N/W	fluid-mechanical effectiveness
τ_{w}	$\mathrm{Pa{=}N/m^2}$	wall-shear stress
ρ, $\rho(\vec{x},t)$	$\mathrm{kg/m^3}$	density
$\phi(t)$	–	phase angle
$\omega\,, \omega_k\,, \omega_z$	1/s	vorticity

Abbreviations

symbol	description
AC	Alternating current
CAM	camera
CCD	Charged Coupled Device
CMOS	Complementary Metal Oxide Semiconductor
CTA	Constant Temperature Anemometry
CV	control volume
DBD	Dielectric Barrier Discharge
DC	Direct current
DC	Duty cycle
DEHS	Di-Ethyl-Hexyl-Sebacat
EHD	electro hydro dynamic
FG	function generator
FOV	fields of view
fps	frames per second
HV	high voltage
IA	interrogation area
LDA	Laser Doppler Anemometry
max	maximum
min	minimum
NSE	Navier-Stokes equations
PAVG	Plasma Actuator Vortex Generator
PIV	Particle Image Velocimetry
RF	Radio frequency
SD	Surface discharges
TU	Technische Universität
VD	Volume discharges
VG	Vortex Generator
WB	weight balance
2D	two-dimensional
3D	three-dimensional

2C	two component
3C	three component

List of Figures

List of Tables

Katrin Barckmann

Center of
Smart Interfaces
Technische Universität Darmstadt
Flughafenstr. 19
D-64347 Griesheim
Germany

phone: +49 6151 16-75349
fax: +49 6151 16-6246
email:
Barckmann@csi.tu-darmstadt.de

Personal

Born on July 18, 1982, in Büdingen, Germany
(German citizenship)

Education

08/2008 - 10/2013	Doctoral research in Mechanical Engineering Technische Universität Darmstadt, Darmstadt, Germany
10/2001 - 03/2008	Studies in Mechanical Engineering (Dipl.-Ing.), Technische Universität Darmstadt, Darmstadt, Germany
1992-2001	Gesamtschule Konradsdorf, Ortenberg, Germany

Employment

since 08/2008	Research assistant at Center of Smart Interfaces, Technische Universität Darmstadt, Darmstadt, Germany
09/2006 - 03/2007	Internship, Dr.Ing.h.c. F.Porsche AG, Computation aerodynamic und thermomanagement, Stuttgart, Germany
07/2006 - 08/2006	Internship, INWAT Zakład Badawczo-Projektowy, Łódź, Poland